Studies of Earth's Mantle using Seismic Traveltimes and Amplitudes

by

Yang Zhang

A dissertation submitted in partial fulfillment
of the requirements for the degree of
Doctor of Philosophy
(Geology)
in The University of Michigan
2011

Doctoral Committee:

Associate Professor Jeroen Ritsema, Chair
Professor August Evrard
Professor Larry John Ruff
Professor Peter E van Keken
Professor Craig R Bina, Northwestern University

For my husband and my parents

ACKNOWLEDGEMENTS

It is an amazing opportunity for me to join the PhD program in the University of Michigan in the first place. I am deeply grateful for my advisor, Prof. Jeroen Ritsema, for providing this wonderful opportunity for me and advise me with support, encouragement, and inspiration throughout my graduate study. He is always patient leading me though unfamiliar areas, and helping me with my knowledge and skill developments. His open and amiable personality also make our discussion relaxing and fruitful. His precious guidance will benefit me through my career path and personal development.

I also want to express my thanks to Prof. Peter van Keken and Prof. Larry Ruff, for their guidance throughout the 5 years of my study here. There are always inspiring discussions of my research results among us. The suggestions they provide to my thesis work are very profound and practical. I also learned from them a broader areas of knowledge from geophysics and geology. Prof. August Evrard and Prof. Craig Bina, as members of my thesis committee, care about my progresses and devoted their valuable time to provide great suggestions.

I want to thank Prof. Mike Thorne from University of Utah, and postdoc scholar Ling Bai for close cooperations on the research projects of my PhD thesis. Thanks go to Profs. Rob Van der Voo, Eric Hetland, Jackie Li, Lars Stixrude for their help and instructions as great experts from geophysics area. My former academic advisors, Carolina R. Lithgow-Bertelloni and Rebecca Lange, provide great assistances and advices during my PhD study.

I am very thankful for former and current members of the geophysics lab. I got many help from former members Nico de Koker, Wenbo Xu, Ni Sun, J.P. Brandenburg, John Naliboff, Stephen Stackhouse, Amy Bengtson for their selfless help, my peer students Yong Keun Hwang and Xin Wan for their enlightening research discussions. The geophysics seminar every Friday is an unforgettable memory, for learning a great deal in geophysics and enjoying inspiring discussions.

I thank Anne Hudon, our graduate program coordinator, Janine and Mike, our IT support for their great favors. I thank my fellow graduate students and great friends within this department, Jing Zhou, Qiaona Hu, Yang Chen, Lixin Jin, Lin Ma, Wenjun Yong, Yuehan Lu, Takehito Ikejiri, Xuan Guo for all the great supports provided. I want to thank fellows in CIDER program, SEG student chapters, and Ann Arbor Toastmasters and Friends Club.

Heartfelt thanks to Xin Feng, my husband for great and love and support. My parents provide endless love and encouragement during these years. I would not able to complete the thesis without them.

TABLE OF CONTENTS

LIST OF FIGURES

Figure

LIST OF TABLES

Table

CHAPTER I

Introduction

1.1 Seismology and the Earth

Seismology is the primary tool to image the Earth's interior. Seismic waves are generated by natural (e.g., earthquakes) or artificial (e.g., man-made explosions) sources. They propagate throughout the Earth and are recorded by seismometers. Seismic waves provide the highest-resolution images of the Earth's structure. A variety of seismic phases recorded have unique paths and their properties (i.e., speed and amplitude) reveal the internal structure of the Earth, such as the elastic and density variations and the presence of internal boundaries. Near the surface, reflection and refraction seismology provides detailed crustal structure that are useful for exploring economic resources such as oil and minerals. In the deeper earth, earthquake seismology is the primary tool for understanding Earth's global scale structure and it is widely used by geodynamicists to constrain Earth's dynamic processes such as convection.

1.1.1 Seismic Traveltimes and Amplitudes

Seismic traveltimes and amplitudes are important characteristics of seismic waves. If the origin time of wave generation from (earthquake) sources is known, wave arrival times, or wave traveltimes, indicate wave speed in the Earth. Seismic waves

can reflect, refract and diffract at boundaries between layers with different physical properties. The contrast of material properties, especially the wave speed and density change across boundaries determine the amplitudes of the reflected and transmitted seismic waves. In a seismogram, traveltimes are measured by onset of seismic phases, and amplitudes are defined by peak ground motions.

Mathematically, P and S velocities derived by traveltimes provide integral constraints along their propagation paths. Based on ray theory, it can be represented by

$$T = \int_{raypath} \frac{ds}{v}. \tag{1.1}$$

The wave amplitude is represented by the integral of velocity gradient.

$$A \propto \int_{raypath} \nabla \cdot \vec{V} ds. \tag{1.2}$$

It is primarily determined by earthquake magnitude, wave attenuation and geometric spreading. (*Aki and Richards*, 1980; *Stein and Wysession*, 2003).

Geometrical spreading, reflection and transmission coefficient, focusing and scattering are pure elastic effects. Geometric spreading explains the decay of wave amplitudes with distance. Reflection and transmission coefficients are determined by the internal layering within the Earth. Seismic waves can be focused and defocused due to lateral variations in wave speed. In addition, amplitude can be modified by wave scattering off small-scale heterogeneities. Earth's anelastic structure cause amplitude decay due to intrinsic attenuation.

The seismic wave traveltimes and amplitudes provide complementary constraints on Earth's structure.

1.1.2 1D Earth Model

The Earth is to first order a layered medium comprised of crust (6–60 km thick), mantle (∼3000 km thick), outer core (∼3000 km thick) and inner core (∼1500 km thick). Seismologically, Earth's crust, mantle and core have distinct variations in seismic velocity and density with depth. A large number of radially symmetric earth models have been derived from seismic observations. The PREM (Preliminary Reference Earth Model) developed by *Dziewonski and Anderson* (1981) has been the standard reference model for the past 30 years. Within it, a radial shear velocity profile, a compressional velocity profile and a density profile are defined. The PREM is derived from global data sets of traveltime, wave dispersions, and free oscillation frequencies.

To demonstrate that the PREM model is an accurate model of Earth's seismic structure, we compare a computed (i.e., synthetic) seismogram based on PREM with an observed seismogram in Figure 1.1. The excellent waveform match and the arrival time and amplitude of large number of phases (such as P, PP, PKKP), indicating that PREM is a good approximation of the Earth's seismic structure.

1.1.3 3D Earth Model

However, there are lateral variations of seismic velocity in the Earth. They exceed 20% in the crust and upper mantle. In the deep mantle, seismic velocity varies laterally by 3–5%. This 3D heterogeneity modifies both traveltimes and amplitudes (shown in Figure 1.1).

The lateral seismic velocity variations provide insight into tectonic processes and deep mantle convection. Since seismic velocity depends on compositional and temperature variation in the Earth, a major goal of seismology is to map the three-dimensional velocity structure.

Seismic tomography is the primary technique used to map 3D heterogenous Earth.

A 3D model of seismic velocity is composed of a standard 1D reference model (usually PREM) and the 3D velocity perturbations based on the 1D velocity, shown as following:

$$V_s(\vec{r}) = V_s^0(r)\left\{1 + \delta V_s(\vec{r})\right\}. \tag{1.3}$$

Tomographic images show velocity anomalies δV_s as percent anomalies of the reference velocity (i.e. $V_s^0(r)$). Figure 1.2(a) shows a cross-section view of the tomography model S40RTS (*Ritsema et al.*, 2010) beneath the Pacific and North America. The shear velocity perturbations relative to the standard PREM model are plotted with scales between -1.5 to 1.5%. It is typical to use blue colors to depict high velocity perturbations and red colors to depict low velocity perturbations. Thus Figure 1.2(a)predicts that seismic waves propagate faster in the deep mantle beneath circum-Pacific region and slower in the mantle beneath the central Pacific region.

3D models of seismic velocity have improved with time due to improved data sets and observational and analytical techniques. Present research focuses on the simulation of 3D models to evaluate the accuracy of the models. One set of 3D waveforms generated for S40RTS is shown in Figure 1.2(b). They are compared to synthetic seismograms for PREM. The waveform simulations such as in Figure 1.2(b) are impoartant to test new seismic models and to recognize which types of data are yet to be explained by 3D seismic models.

1.2 The Deep Earth

The Earth is a chemically layered planet. The boundaries between the crust and the mantle (the Moho) and between the mantle and the core (the core-mantle boundary or CMB) of Earth's principle layers have strong seismic contrasts. The crust has been extensively explored using a variety of high-resolution geophysical techniques. The mantle, on the other hand, is primarily constrained by seismic waves,

whose velocities and amplitudes reveal the incompressibility, rigidity and density, and the contrasts of internal phase boundaries.

This thesis describes several studies of the mantle that combine observational and computational approaches. We review past seismic studies of the upper mantle, the lower mantle, and mantle discontinuities in the following three sections. This is followed by a section describing some of the problems and uncertainties related to seismic studies of the Earth's deep interior, and sections describing research objectives and the outline of the thesis.

1.2.1 The Upper Mantle

Strong seismic velocity variations exist in the upper mantle due to plate tectonic processes and depth variations associated with a myriad of high-pressure phase transformations in mantle minerals. Global seismic-velocity discontinuities are present at depths near 410, 520, 660 km and define the transition zone. Whereas compositional changes underlie the Moho and CMB, the 410-, 520- and 660-km discontinuities represent pressure and temperature induced mineralogical phase transformations to denser lattice structures.

The 410- and 660-km discontinuities are global boundaries that vary in depth due to temperature variations in the mantle. Depth estimates are made using a variety of body waves, such as P'P'(PKPPKP) precursors (e.g. *Adams*, 1968; *Xu et al.*, 2003), P-to-SV conversions (e.g. *Li et al.*, 1998; *Dueker and Sheehan*, 1998), SS precursors (e.g. *Shearer et al.*, 1999; *Lawrence and Shearer*, 2006a), near-source S-to-P conversions and depth phases (e.g. *Flanagan and Shearer*, 1998; *Ritsema et al.*, 1995). The signals are analyzed after stacking to bring the relatively low amplitude reflections above noise level (*Shearer*, 1991; *Shearer and Masters*, 1992). The depth of the 410-km and 660-km varies globally by 20 to 30 km. The thickness of the transition zone, as defined by the 410- and 660-km, is largest in subduction zones. The thickness

variation is primarily due to thermal heterogeneity. Temperature variations cause a phase boundary to vary in depth. The results from seismic reflections can be used to explain the mineral structure of the upper mantle, the presence of melt, and the discontinuity topography on a global and regional scale (*Shearer*, 2000; *Helffrich*, 2000; *Kind and Li*, 2007; *Deuss*, 2009).

1.2.2 The Lower Mantle

Significant internal boundaries are absent between 710 to 2600 km depth throughout most of the Earth's lower mantle. Lateral variations in seismic velocity can be modeled using seismic tomography. Relatively high velocities extend downward beneath the Pacific rim. Two broad low velocity regions are present beneath the central Pacific and Africa. These low velocity regions have been termed large low seismic velocity provinces (LLSVPs) (*Garnero and McNamara*, 2008).

The core-mantle boundary (CMB) marks Earth's largest step increase in density. This boundary exists 2890 km beneath the surface, and is the interface between the solid rock mantle and the liquid iron alloy outer core. The contrast in chemistry, dynamics, and physical states across the CMB is large and comparable to that at the Earth's surface. The lowermost several hundred kilometers above the CMB is much more heterogeneous than the overlying lower mantle. The thermal, chemical and compositional variations are of great interest to geoscientists, since they elucidate Earth's evolution, thermal history, and mantle and core dynamics (e.g. *Hager et al.*, 1985; *Gurnis et al.*, 2000; *McNamara and Zhong*, 2004, 2005). The D" region is characterized by shear-velocity discontinuities with positive and negative gradients (e.g. *Lay and Helmberger*, 1983; *Ritsema et al.*, 1997; *Avants et al.*, 2006; *Lay et al.*, 2006; *van der Hilst et al.*, 2007), anisotropic properties (*Panning and Romanowicz*, 2006; *Rokosky et al.*, 2006), and ultralow velocity zones (ULVZs) (e.g. *Garnero et al.*, 1993; *Rost et al.*, 2006; *McNamara et al.*, 2010).

1.2.2.1 LLSVPs

Both inverse (i.e., tomographic) and forward modeling of high-amplitude phase traveltimes and normal-mode frequencies have led to images of the large-scale (>1000 km) three-dimensional (3-D) structure of the Earth's interior (e.g. *Dziewonski et al.*, 1977; *Ritsema et al.*, 1999; *Kuo et al.*, 2000; *Panning and Romanowicz*, 2006; *Kustowski et al.*, 2008; *Li et al.*, 2008; *He and Wen*, 2009; *Ritsema et al.*, 2009b; *Simmons et al.*, 2009). The images reveal consistent low seismic velocity provinces (LLSVPs) (*Garnero and McNamara*, 2008; *Dziewonski et al.*, 2010) in the lower mantle. The LLSVPs rise from CMB to at least 1000 km above the CMB (e.g., *To et al.*, 2005; *Takeuchi et al.*, 2008; *Sun et al.*, 2010). The LLSVPs are hypothesized as distinct compositions (e.g. *Ni and Helmberger*, 2003a; *Trampert et al.*, 2004; *Bull et al.*, 2009). The low S-wave velocity have attendant moderately low P-wave velocity (*Masters et al.*, 2000), and possible high density (*Ishii and Tromp*, 2001).

Forward modeling has been instrumental in constraining lateral gradients associated with the margins of LLSVPs beneath the Pacific and Africa. 2D waveform synthetics of wide-angle SH signals are used by *Ritsema et al.* (1998) and *Wen* (2001) to model the steeply dipping western margin of the LLSVP beneath Africa. *Wang and Wen* (2004) mapped the L-shaped configuration of the low-velocity provinces. *Ni et al.* (2002) used SKS phases together with tomography models to constrain the sharp velocity reduction of ∼3% within the LLSVP. The southeastern margin of the African LLSVP has been investigated by *Ni and Helmberger* (2003a,b); *Ni et al.* (2005). *He et al.* (2006) utilized S and ScS travel times and waveforms and found a S-wave reduction of -5% in the lowermost 300 km at the northwestern boundary of the Pacific LLSVP . *Takeuchi et al.* (2008) used differential time analysis of ScS-S and sScS-sS to study the western edge and propose a 4% velocity change. *He and Wen* (2009) found evident of two regions of the LLSVP separated by a 740-km gap using SKS, SKKS, and Sdiff arrivals. *To et al.* (2005) and *Ford et al.* (2006) analyzed the

southern and southeastern LLSVP margins and found a strong lateral gradient north of approximately 52^oS. Lateral variations in PKPab travel times and multipathing also indicate strong lateral gradients at the northern end of the Pacific LLSVP(*Luo et al.*, 2001).

1.2.2.2 Deep Mantle Discontinuities

The D" region was originally defined by *Bullen* (1949) as the lowermost 200 km or so of the mantle with a lower gradient in seismic velocities than the overlying lower mantle. The term D" refers to the bottom few hundred kilometers of the mantle, but the exact thickness vary geographically (see review by *Young and Lay* (1987)). Both positive and negative D" velocity gradients have been proposed in past studies, which has significant implications on the temperature profile at the base of the mantle. The discovery in 2004 of a phase change in the primary lower-mantle mineral, magnesium silicate perovskite $[(Mg, Fe)SiO_3]$ (*Iitaka et al.*, 2004; *Murakami et al.*, 2004), provides a plausible explanation for the P- and S-wave velocity discontinuities at the top of the D" layer (e.g. *Tsuchiya et al.*, 2004; *Hernlund et al.*, 2005; *Tsuchiya and Tsuchiya*, 2006).

Seismological investigations of D" have not yet resulted in a complete characterization of the region, although it is clear that D" is a heterogeneous region. Diffracted-wave studies that transverse long distances in the D" region constrain radial velocity gradients (e.g. *Wysession et al.*, 1992; *Ritsema et al.*, 1997), while studies of S, ScS and Scd have detected abrupt velocity discontinuities near the top of D" (e.g. *Lay and Helmberger*, 1983; *Wysession et al.*, 2001; *Sun et al.*, 2007). Velocity discontinuities have also been constrained by P-wave reflected (PdP) arrivals (e.g. *Weber*, 1993; *Thorne et al.*, 2007) (see review by *Lay and Garnero* (2007)). Tomographic inversions resolve large-scale heterogeneities in D" region (e.g. *Obayashi and Fukao*, 1997; *Sun and Helmberger*, 2008).

1.2.2.3 ULVZs

A number of studies mapped Ultra-Low Velocity Zones (ULVZs) near the margins of LLSVPs at the base of mantle (*Garnero et al.*, 1993; *McNamara et al.*, 2010). The ULVZs are typically of 10–40 km thick and have extreme (10–40%) reductions in shear velocity. They have been modeled primarily using SP_dKS traveltimes (e.g., *Garnero and Helmberger*, 1996; *Rondenay and Fischer*, 2003) and PcP and ScP reflections (e.g., *Rost and Revenaugh*, 2001, 2003; *Rost and Garnero*, 2006; *Idehara et al.*, 2007; *Hutko et al.*, 2009). The magnitude of the velocity reductions and relative effects on P- and S-wave velocity have been attributed to the presence of partial melt. It has been suggested (e.g., *Williams and Garnero*, 1996; *Hernlund and Tackley*, 2007) that ULVZs are located in the center and at the edges of the LLSVPs (e.g., *Thorne and Garnero*, 2004). Further complexity indicated by short-period signal scattering (*Garnero and Vidale*, 1999; *Castle and van der Hilst*, 2000; *Reasoner and Revenaugh*, 2000; *Persh et al.*, 2001; *Castle and ver der Hilst*, 2003; *Rost and Revenaugh*, 2003; *Rost et al.*, 2005, 2006; *Xu and Koper*, 2009; *McNamara et al.*, 2010; *Rost et al.*, 2010a,b) may be linked to ULVZs. It is still uncertain whether the anomalous structure is concentrated on the mantle side of the CMB or in a thin zone of finite rigidity or anomalous P-wave velocity on the core side (*Buffett et al.*, 2000; *Garnero and Jeanloz*, 2000; *Rost and Revenaugh*, 2001).

1.2.2.4 Examples of the Pacific Lower Mantle Models

Previous studies of modeling the Pacific lower mantle can be categorized into two groups: Tomography studies which use long-wavelengths data to image the large-scale 3D velocity structure, and regional modeling which use short-wavelengths data, and seismic phases of reflection, diffraction to model the small-scale regional 1D velocity structure. The vertical scales of these models (which will be discussed in Chapter 2 and 3) vary. The Pacific anomaly as imaged tomographically (e.g., S40RTS) extend

vertically to at least about 1000 km above the core-mantle boundary. The regional model M1 (*Ritsema et al.*, 1997) indicate a negative gradient start at the bottom 200 km of the mantle. The ULVZ structure, as discussed by previous studies (e.g. *Garnero et al.*, 1993), has a thickness of 20 – 50 km above the core-mantle boundary.

Example synthetics of the model S40RTS, M1 and ULVZ are shown in Figure 1.3 and compared with PREM synthetics at a distance of 110^o. The phases SKS, SKKS and S(diff) are marked on the synthetics. We observe most time shifts in the synthetics for the model S40RTS but no obvious amplitude change. On the other hand, in the M1 synthetics we observe both amplitude amplification and time shifts for the phase S(diff). The SKS amplitude are severely reduced for model ULVZ and complicated by with another phase generated behind the SKS phase. From these comparisons we observe that different models of seismic structure predict the seismic wave traveltime and amplitude differently. This indicates that traveltimes and amplitudes are highly sensitive to velocity structure, and can be utilized further to explore the detailed Pacific lower mantle.

1.3 Overview of the Thesis

1.3.1 Motivation

Tomographic imaging and regional wave modeling studies provide complementary constraints on the large-scale and small-scale heterogeneity in Earth's mantle. However, many issues in seismic studies of the Earth's deep interior remain unresolved.

The seismic structure of the lowermost mantle is only constrained in detail for localized regions. Tomographic images continue to increase in resolution as data sets accumulate and new seismic networks are deployed. With better resolved 3-D mantle heterogeneity images, more detailed images of CMB topography, D" velocity structure, LLSVPs and ULVZs are forthcoming. Despite progress, various seismic

information, such as amplitudes, have not yet been fully exploited to constrain the wavespeed variations or to verify independently the accuracy of tomographic images.

On the other hand, the data sets used in tomographic inversions have limited coverage and irregular source-receiver geometries. Regularization of tomography render image uncertainties (*Marone et al.*, 2007; *Ritsema et al.*, 2009b), as well as the ray theory approximation (*Li and Romanowicz*, 1995; *Nolet and Dahlen*, 2000; *Dahlen et al.*, 2000). Detailed regional waveform modeling in the Pacific region provide local vertical profiles with different discontinuities, velocity gradients and absolute shear velocities (*Ritsema et al.*, 1997; *Lay et al.*, 2006; *Kawai and Geller*, 2010), but the modeling is compromised by trade-offs, restrictive epicentral distance ranges and used seismic phases, and simplified 1D model parameterizations. The gap between the large-scale and small-scale structures raises the question whether the multi-scale seismic structure can be independently constrained.

Numerous studies suggest that ray-theoretical traveltime calculations may be imprecise. Especially for the broad sensitivity of SS wave (*Chaljub and Tarantolla*, 1997; *Neele et al.*, 1997; *Neele and de Regt*, 1999; *Zhao and Chevrot*, 2003; *Dahlen*, 2005), traveltime contributions due to shear-velocity heterogeneity has so far been estimated by ray-tracing through tomographic velocity models. While ray theory is simple, it is still questionable whether it can be used to approximate seismic wave propagation.

This thesis focuses on evaluations of existing models for the mantle and to determine how well they explain a variety of seismic data types, including seismic traveltimes and amplitudes. We are motivated to bridge the gap between long-wavelength tomographic studies and smaller wavelength detailed regional studies. New seismic data types provide additional detailed information on the nature of deep mantle heterogeneity. Amplitudes, in particular, are often ignored to quantify the deep Earth structure. 3D waveforms are calculated using advanced computing techniques. To make progress towards integrating seismically resolved structures and studies of the

thermal, chemical and dynamic behavior or the deep earth, particularly the lower mantle, documenting detailed behavior of seismic phases sensitive to the region is necessary.

1.3.2 Objective

The objective of this work is to provide detailed measurements and subsequent analysis of seismic data sets sensitive to deep Earth structure. Particular emphasis is on seismic amplitudes that have not been utilized for documenting mantle heterogeneity. It is the goal of this work to determine whether structure in the mantle can cause waveform and amplitude complexity, to provide information on the scale lengths of heterogeneity prevalent in the Pacific lower mantle, to determine how inaccurate ray-theoretical corrections project as artifacts in traveltime maps of synthetic waveform stacks through computing of 3D SEM waveforms, and to demonstrate how the coherent global and distance patterns of SS/S amplitude ratios are determined by the focusing effects. A long-term objective is to evaluate the potential improvement of tomographic studies with the use of seismic wave amplitudes.

1.3.3 Outline

The thesis has four chapters that have been individually published, or submitted for publication. These chapters are thus self contained, with its own abstract, introduction, and conclusion. Chapter 2 was published as "Modeling the ratios of SKKS and SKS amplitude with ultra-low velocity zones at the core-mantle boundary" in *Geophys. Res. Lett.*, 2009. Chapter 3 embodies "Evaluation of 1D and 3D seismic models of the Pacific lower mantle with S, SKS and SKKS traveltimes and amplitudes" submitted to *J. Geophys. Res.*. Chapter 4 contains "An analysis of SS precursors using spectral-element method seismograms" submitted to *Geophys. J. Inter.*. Chapter 5 will eventually be developed into an article entitled "Modeling

spatial distribution of SS/S amplitude ratios". Chapter 6 summarize the findings and propose future work directions.

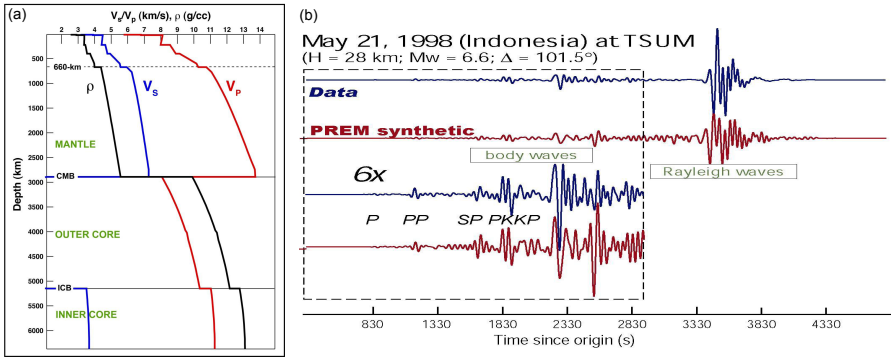

Figure 1.1: PREM (Preliminary Reference Earth Model) (*Dziewonski and Anderson*, 1981) is shown with example seismograms computed from PREM (red line) and observed from a real event (blue line), separately. The observed seismogram is collected at station TSUM from an event happened on May 21st, 1998, with depth at 28 km and magnitude 6.6.

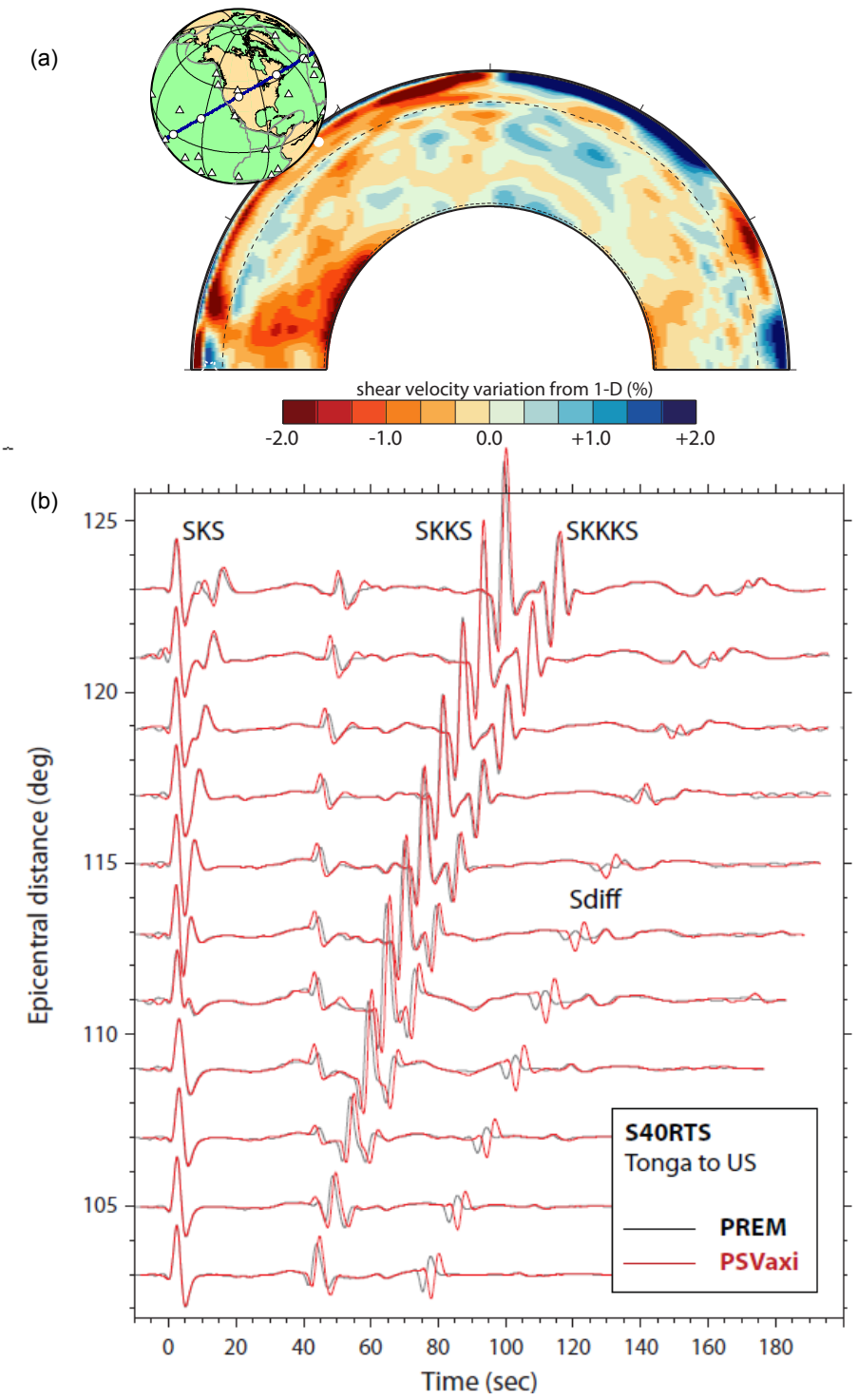

Figure 1.2: A 3D tomography image (from model S40RTS (*Ritsema et al.*, 2010)) is plotted with 3D seismograms generated from this cross section using method PSVaxi (*Jahnke et al.*, 2008). The map with the cross section path is shown in the upper left corner of the tomographic image, the mantle of both the Pacific and North America regions are displayed with their shear velocity perturbations.

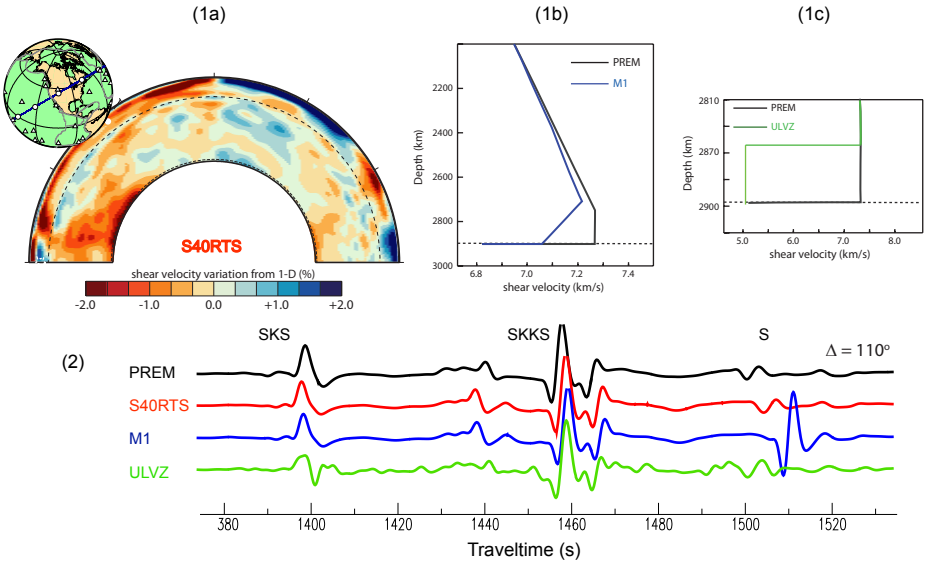

Figure 1.3: Models of the Pacific lower mantle (S40RTS (*Ritsema et al.*, 2010), M1 (*Ritsema et al.*, 1997), ULVZ (e.g. *Zhang et al.*, 2009)) are shown with their synthetic seismograms compared with PREM (in black). The traveltime and amplitudes of the seismic phases SKS, SKKS and S can be clearly observed.

CHAPTER II

Modeling the ratios of SKKS and SKS amplitudes with ultra-low velocity zones at the core-mantle boundary

2.1 Abstract

Between 105–115° degrees, the SKS waveform is complicated by the formation of SP_dKS, a wave that has segments of P diffraction along the core mantle boundary. While previous studies have primarily focused on the move-out of SP_dKS from SKS, we analyze the concomitant reduction of the SKS amplitude. Long-period SKKS/SKS amplitude ratios present a coherent global pattern. SKKS/SKS is relatively large in North and South American recordings of deep Tonga-Fiji earthquakes but PREM-like in European recordings of earthquakes in South America and Indonesia. Modeling of SKKS/SKS indicate that Ultra-Low Velocity Zones (ULVZs) layers at the base of the mantle with a thickness of about 10–20 km and a shear velocity reduction between 20–30%, are required to explain high SKKS/SKS ratios and the early move-out of SP_dKS.

2.2 Introduction

Joint seismological and mineral physics studies have suggested that silicate melts may be present at the base of the mantle (e.g., *Williams and Garnero*, 1996; *Hernlund and Tackley*, 2007). Seismically, these melt structures can be modeled as 10–40 km thick layers with extreme (10–40%) reductions in shear velocity (e.g., *Thorne and Garnero*, 2004). These Ultra-Low Velocity Zones (ULVZs) in general have variable shapes, widths, and distributions across the CMB. The best studied ULVZ is located at the margins of a low seismic velocity anomaly beneath the Pacific (e.g., *Garnero et al.*, 1998; *Simmons and Grand*, 2002; *Ni and Helmberger*, 2003b).

So far, ULVZs have been modeled primarily using SP_dKS traveltimes (e.g., *Garnero and Helmberger*, 1996; *Rondenay and Fischer*, 2003) and PcP and ScP reflections (e.g., *Rost and Revenaugh*, 2001, 2003; *Rost and Garnero*, 2006; *Idehara et al.*, 2007; *Hutko et al.*, 2009). Here, we demonstrate that the frequency-dependent amplitude ratio of the seismic phases SKKS and SKS can provide complementary constraints.

2.3 Method

Since SKS and SKKS waves propagate along similar paths in the upper mantle, anomalous traveltime (e.g., *Souriau and Poupinet*, 1991) and amplitude (e.g., *Silver and Bina*, 1993) differences are excellent indicators of deep mantle heterogeneity (Figure 2.1). SKS bifurcates near a distance of about 104° (depending on source depth) for PREM (*Dziewonski and Anderson*, 1981). At this distance, SP_dKS, a wave that includes segments of P diffraction along the core-mantle boundary (CMB) develops (*Choy*, 1977) and SKS decreases in amplitude. However, SP_dKS forms earlier when ULVZs are present. Consequently, the difference time between SP_dKS and SKS and the amplitude ratios of SKKS and SKS are larger than expected for PREM.

We define the SKKS/SKS amplitude ratio as

$$R = \log_{10}\left(\frac{A_{\mathrm{SKKS}}}{A_{\mathrm{SKS}}}\right) - \log_{10}\left(\frac{A_{\mathrm{SKKS}}}{A_{\mathrm{SKS}}}\right)_{\mathrm{REF}} \tag{2.1}$$

where the second term is determined for the PREM velocity structure and Global CMT event parameters. Figure 2.2 shows two examples of SKS and SKKS recordings and PREM synthetics of the October 16, 2007 (Depth = 512 km, M_w = 6.6) Fiji Islands earthquake at stations CCM and FVM in Missouri. These recordings are representative of the signal quality of SKS and SKKS and they illustrate that variability in R is evident even for nearby stations.

R has a clear geographic pattern. Figure 2.3 shows R as a function of epicentral distance (Δ) for measurements from four subsets of data. These data sets are derived from deep ($>$ 500 km) earthquakes with moment magnitudes larger than 6.5 that exhibit SKS and SKKS signals with (> 5) signal-to-noise-ratios. Groups A and B are southwest Pacific events recorded in North America and South America, respectively. Group C includes South American events recorded in Europe, and group D includes Indonesian events recorded in North America. R reaches an averaged peak value between $\Delta = 100^\circ$ and $\Delta = 110^\circ$ of about 0.5 and 0.3 for recordings from groups A and B, respectively. For groups A and B, the SKS core-entry points are within a broad low shear-velocity anomaly at the CMB beneath the Pacific Ocean (see Figure 2.1). In contrast, SKKS/SKS ratios for groups C and D can be explained by PREM synthetics. Incidentally, shear velocities near the SKS core-entry and core-exit points for the group C and D recordings are similar to those in PREM.

2.4 SKKS/SKS ratios for the Pacific

We analyze in more detail the data are from five recent Tonga-Fiji earthquake recordings from broadband stations in the United States that make up group A. $R(\omega)$

is measured via spectral ratios using 1-D waveform calculations with the reflectivity method (*Fuchs and Muller*, 1971) and 3D waveform calculations for axi-symmetric structures (*Igel and Weber*, 1996; *Jahnke et al.*, 2008). The spectral ratios can be reliably measured between period of 5–20s by applying spectral smoothing and multi-taper techniques. At a period of 20 s, R is measured beyond 98° when SKKS and SKS are well separated. Primarily due to waveform differences in the recordings and synthetics render a measurement uncertainty in R of about 0.05. This is an order of magnitude smaller than the variability of R. We apply upper mantle anisotropy corrections for those stations with available SKS splitting parameters (*Schutt and Humphreys*, 2001).

We first consider three models for the Pacific lower mantle: M1 (*Ritsema et al.*, 1997), SPAC (*Russell et al.*, 2001), and SPAC2 (*Avants et al.*, 2006), which have 2–3% shear-velocity reductions in the lowermost 200–300 km of the mantle. Model SPAC includes a 10-km thick ULVZ with a P and S velocity that is, respectively, 4% and 12% smaller than in PREM.

As demonstrated in Figure 2.4, these models with modest velocity reductions fail to reproduce the high values of R at 0.1 Hz (and other frequencies). Predicted values for the SKKS/SKS ratio by models M1 and SPAC2 are nearly identical to the PREM predicted values. Only SPAC reproduces the increase in R near 100° but underestimates its peak value.

Next we consider ULVZs, embedded in the PREM velocity structure. SKKS/SKS amplitude ratios for ULVZs within more realistic models for the Pacific lower mantle (e.g., M1, SPAC, or SPAC2) produce virtually identical results. Given the considerable variability in R (see Figure 2.2), we model the ULVZ as a single layer and modify its thickness and velocity reductions from PREM. The ULVZ is present only at the core-entry region of SKS but both SKS and SKKS traverse it. At the core-exit side of SKS the seismic structure is identical to PREM.

In Figure 2.5a, R is compared to predicted values for ULVZs that have thicknesses of 5, 10, and 15 km. The reductions in S and P velocity are 18% and 6%, respectively. In Figure 2.5b, the ULVZs are 10 km thick and have S-velocity reductions of 30%, 18%, and 6% and accompanying P-velocity reductions that are 3× smaller. In Figure 2.5c, we consider ULVZs with a thickness of 10 km, a S-velocity reduction of 18%, and P-velocity reductions of 6%, 12%, and 18%. Thus the ratios of S and P velocity reductions are 3:1, 3:2, and 3:3, which are expected when melts are present (3:1) (e.g., *Williams and Garnero*, 1996; *Revenaugh and Meyer*, 1997), or when the ULVZ is compositionally distinct (3:3).

We analyze the match to R at frequencies of f=0.1 Hz and f=0.05 Hz, the upper and lower frequency limits for which R is measured most reliably. R is consistently larger than 0 for distances up to 108°. R is negative between 108° and 115° due to the formation of SP_dKS for PREM. The oscillation in R is strongest at 0.1Hz. Observed R values reach around 0.2 at a distance longer than 120°, which cannot be reproduced accurately by our ULVZ models.

R is highest for the thickest ULVZs or ULVZz with the largest velocity reductions and R's maximum value shifts to the shortest distances. These trends are due to the advanced move-out of SP_dKS from SKS and the reduction of the SKS amplitude. For the ULVZ structures examined in Figure 2.5, the maximum values of R are larger for f = 0.1 Hz and R peaks approximately 5° earlier. The frequency dependence of R can, in principle, help reduce the modeling trade-off between thickness and velocity.

As pointed out previously (e.g., *Garnero and Helmberger*, 1998), there is a trade-off between thickness and shear velocity reduction. For thickness between 5–15 km, when the high-frequency SKS waveforms are matched best (*Stutzmann et al.*, 2000), we resolve a shear-velocity reduction of 18%∼30%. Values that are comparable to those inferred from SP_dKS traveltime studies (e.g., *Thorne and Garnero*, 2004). Especially at f = 0.1 Hz, the high R values for distances smaller than 108° are reproduced

best for a ratio of S and P-velocity reductions of 3:2.

2.5 Discussion and Conclusions

The scatter in R is large and not due to measurement error. Figure 2.2 demonstrates that SKS and SKKS (and Sdiff) amplitudes from nearly co-located (from a teleseismic point of view) stations can differ significantly. Sources for this scatter may include anisotropy at the base of the mantle (*Fouch et al.*, 2001; *Long*, 2009), shear velocity gradients (*To et al.*, 2005), and core mantle boundary topography (*Restivo and Helffrich*, 2006). The scatter indicates the presence of fine-scale structure that cannot be addressed with our simplified models and synthetics.

We emphasize therefore the overall trends in the SKKS/SKS amplitude ratios. First, SKKS/SKS amplitude ratios are anomalous with respect to standard model predictions only when SKS core-entry points are within the low shear-velocity region beneath the Pacific. Second, Tonga-Fiji earthquake recordings from Norh America show a systematic variation with epicentral distance (95°–125°) and signal frequency. This cannot be explained by 1D shear-velocity profiles that include 2–3% shear-velocity reductions in the lowermost several hundreds of kilometers of the mantle. Rather, our long-period data require the presence of thin (∼10-20km) Ultra-Low Velocity Zones (ULVZ) in which the shear velocity is reduced by 20–30%, corroborating previous (short period and broadband) modeling efforts.

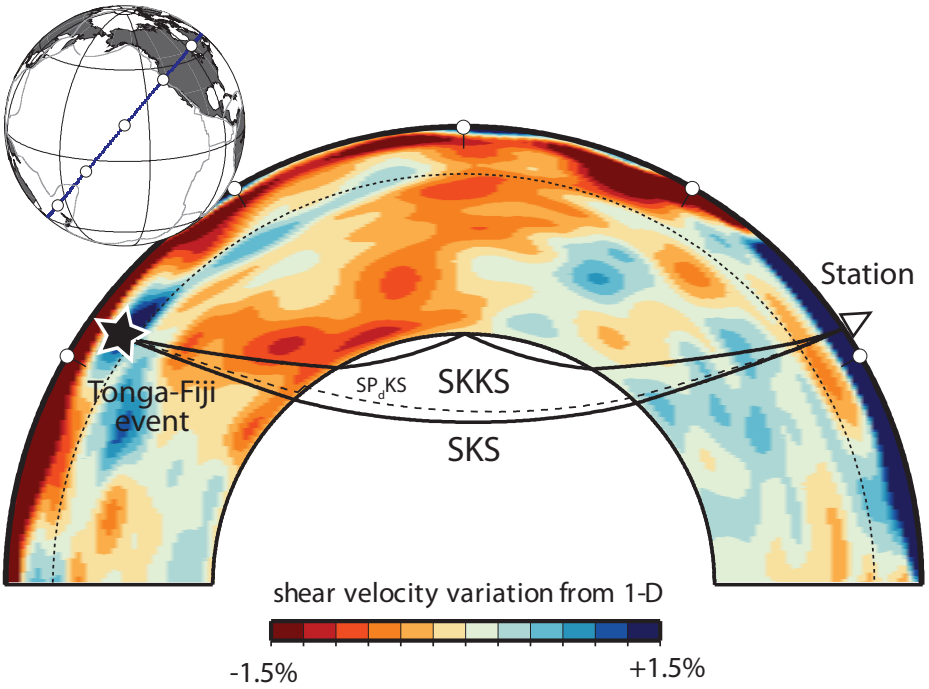

Figure 2.1: Geometrical ray paths of SKS, SKKS (solid lines) and SP_dKS (dashed line) propagating are shown from a deep earthquake in the Tonga-Fiji region (dark circle) to a North American station (light circles) at an epicentral distance of 110^o. The background shows the shear velocity variation in the mantle according to *Ritsema et al.* (1999). The shear velocity in regions shaded dark (light) grey is lower (higher) than in PREM.

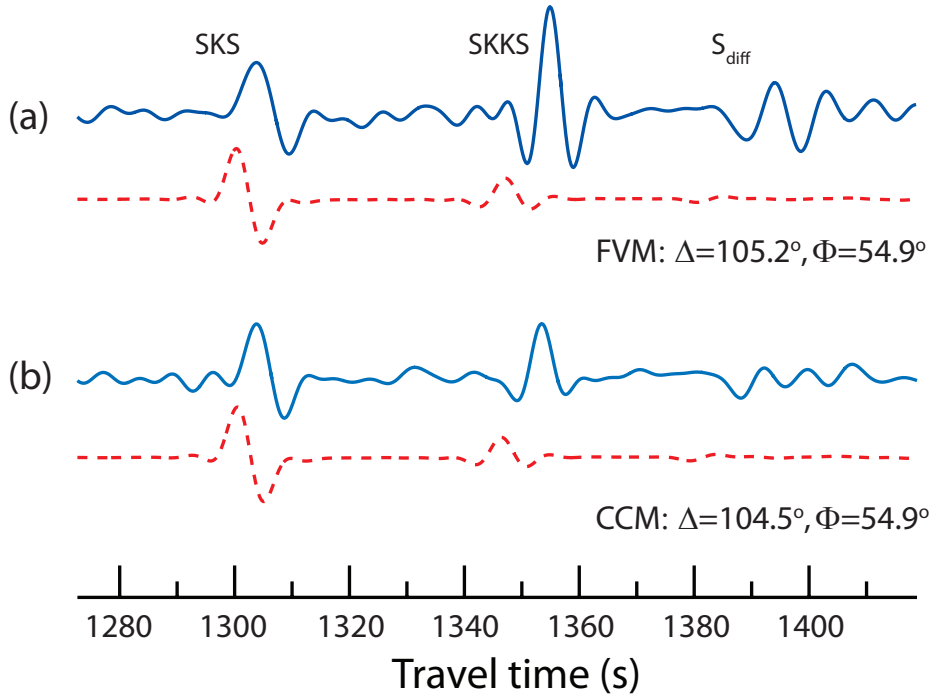

Figure 2.2: Radial component observed(solid) and synthetic(dashed)seismograms at stations FVM (French Village, Missouri) and CCM (Cathedral Cave, Missouri) from Global-CMT event C200710162105A. Both stations are at nearly similar epicentral distance and source azimuth. Note the similar SKS amplitudes and that the amplitudes of SKKS and Sdiff are significantly different.

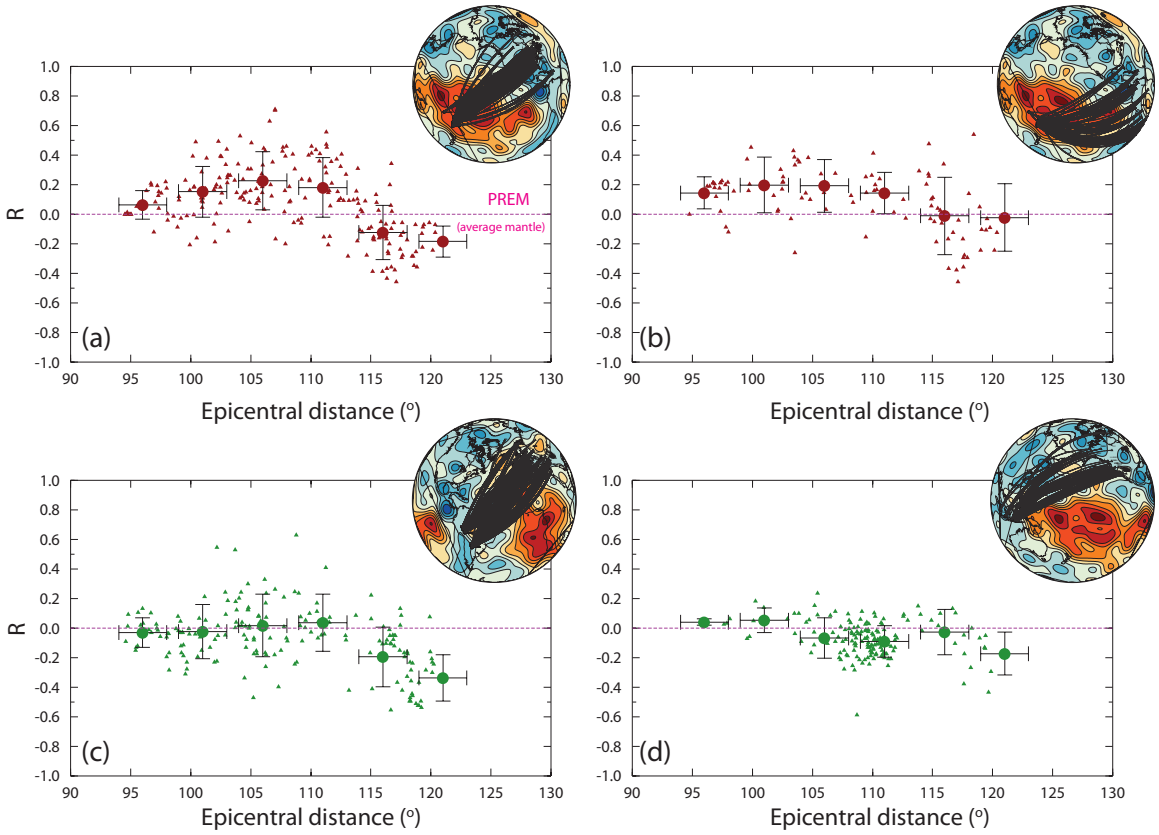

Figure 2.3: Global measurements of R are shown for four mantle corridors: (a) Southwest Pacific to North America, (b) Southwest Pacific to South America, (c) South America to Europe, and (d) Indonesia to North America. Open circles are individual measurements while solid circles and error bars are average values within 5° epicentral distance bins and standard deviations. Globes superposed in the upper right corner indicate the great-circle paths for each group and the shear-velocity variation at the core-mantle boundary (*Ritsema et al.*, 1999).

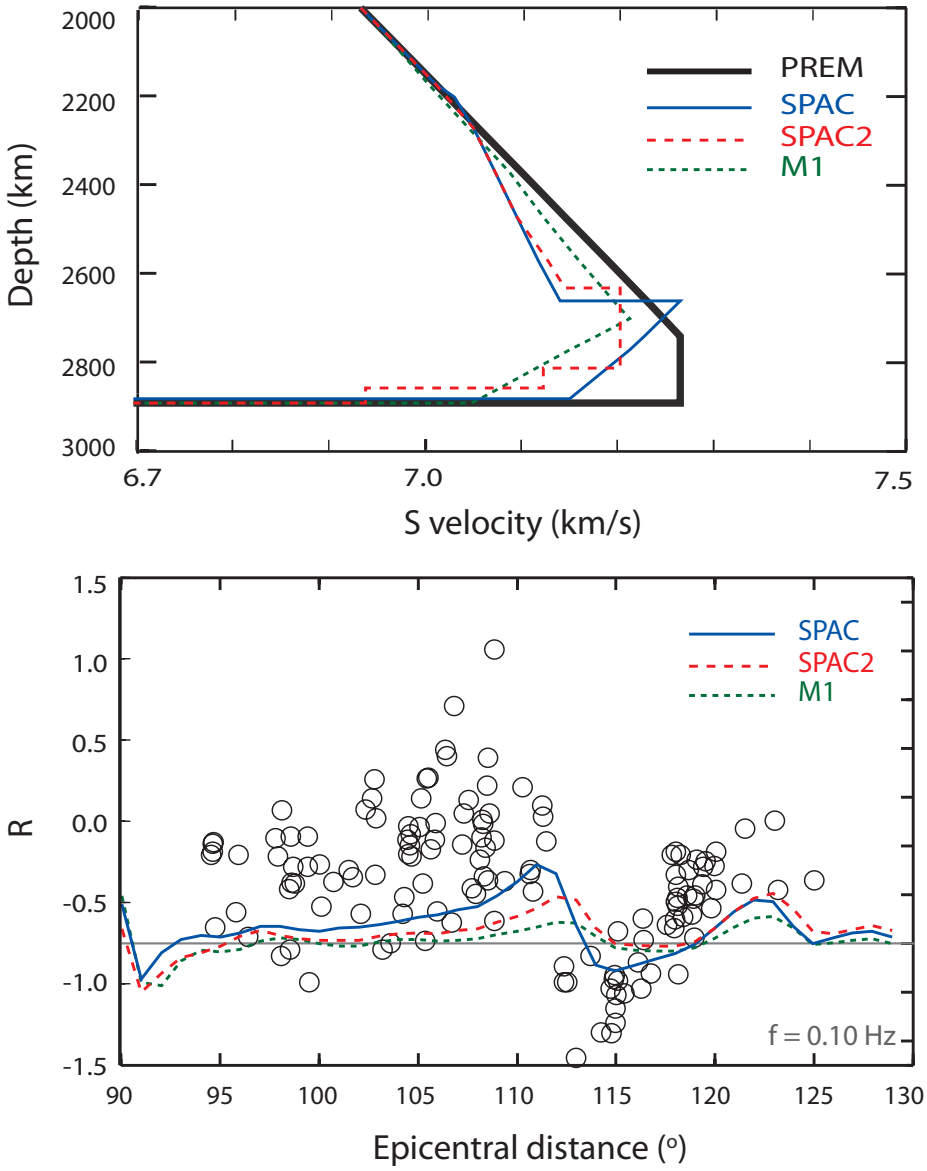

Figure 2.4: Shear velocity profiles (top)and R predications of SPAC, SPAC2 and M1 (bottom) are shown. Measurements of R (circles) and model predictions for model SPAC (blue solid line), SPAC2 (red dashed line) and M1 (green dotted line) at 0.10 Hz.

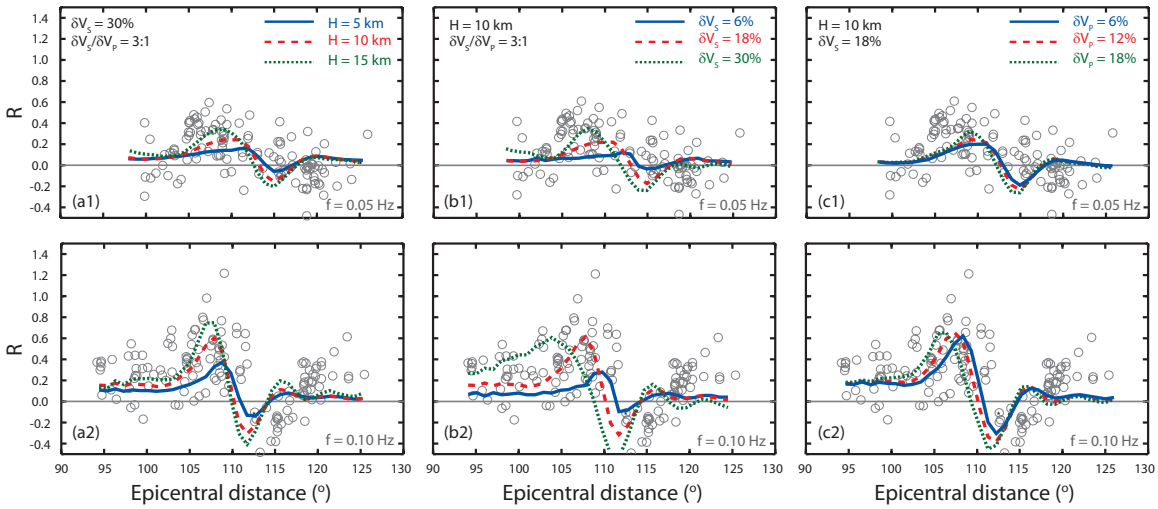

Figure 2.5: Modeling of R is shown using ULVZ structures. Measurements (circles) and model predictions (lines) of R at (top) 0.05 Hz and (bottom) 0.1 Hz for ULVZs at the SKS and SKKS core-entry points. Varied are (left) ULVZ thickness, (middle) V_S reduction, and (right) the ratio of the V_S and V_P reductions.

CHAPTER III

Evaluation of 1D and 3D seismic models of the Pacific lower mantle with S, SKS, and SKKS traveltimes and amplitudes

3.1 Abstract

Tomographic inversion and waveform forward modeling provide us with different angles to examine the nature of the Pacific lower mantle. We use a data set from Fiji earthquakes recorded over a wide teleseismic distances (80–140^o) at North American stations. Measurements are taken on the seismic phases S, SKS and SKKS traveltime residuals and amplitude ratios. Large-scale mantle structure, as seen tomographically, causes traveltime variability over regional distances. The amplitude variability of S/SKS is induced by a localized negative shear velocity gradient of $\sim$2%, while SKKS/SKS amplitude variability is attributed by a source-side ultralow velocity zone (ULVZ)(*Zhang et al.*, 2009). Best estimates can be achieved by a hybrid model composed of the tomographically revealed large-scale low velocity structure, regional gradients and ULVZs.

3.2 Introduction

Two approaches characterize the seismic modeling of the lower mantle. The first approach involves the inverse (i.e., tomographic) and forward modeling of high-amplitude phase traveltimes and normal-mode frequencies to imaging the large-scale ($>$ 1000 km) three-dimensional (3-D) structure of the Earth's interior. While the modeling of regional network waveforms have produced radial profiles of seismic velocity in well-sampled regions. The images reveal two antipodal large, low seismic velocity provinces (LLSVPs) (*Garnero and McNamara*, 2008; *Dziewonski et al.*, 2010) in the lower mantle, hypothesized to be long-lived piles of compositionally distinct material (e.g. *Ni and Helmberger*, 2003a; *Trampert et al.*, 2004; *Bull et al.*, 2009). The LLSVPs are broad at the core-mantle boundary (CMB) (*He and Wen*, 2009) and their relatively sharp margins extend from the CMB at least 1000 km into the mantle (e.g., *To et al.*, 2005; *Takeuchi et al.*, 2008; *Sun et al.*, 2010). The second approach involves detailed waveform modeling and array processing of low-amplitude signals to constrain velocity profiles in well sampled mantle regions. The profiles reveal mantle layering (e.g. *Russell et al.*, 2001) due to the mineral phase changes (e.g., *Hernlund et al.*, 2005; *Lay et al.*, 2006), the presence of melt layers (e.g., *Williams and Garnero*, 1996; *Hernlund and Tackley*, 2007; *Hutko et al.*, 2009), and shear anisotropy (e.g., *Pulliam and Sen*, 1998; *Ford et al.*, 2006). See *Rost and Thomas* (2009) and *Lay and Garnero* (2011) for reviews.

Usually, the tomographic images and the wavespeed profiles are regarded as complementary views in which 'fine-scale' layering of D" ($<$ 500 km) is embedded within the large-scale ($>$ 1000 km) convecting lower mantle. Figure 3.1 provides an example view of the lower mantle beneath the Pacific Ocean. In Figure 3.1(a) the SW–NE oriented cross-section through tomography model S40RTS (*Ritsema et al.*, 2010) shows the Pacific LLSVP extending from the core-mantle boundary (CMB) halfway into the mid-mantle. The LLSVP is asymmetrically positioned between Tonga-Fiji and

North America, Figure 3.1(b)shows the PREM and three shear-velocity profiles for the central Pacific Ocean based on Fiji-Tonga waveform data. The discontinuities, the velocity gradients, and absolute shear velocities in M1 (*Ritsema et al.*, 1997), L2 (*Lay et al.*, 2006) and KG10 (*Kawai and Geller*, 2010) have been attributed to phase transitions in perovskite and anomalous thermal gradients at the base of the Pacific LLSVP (e.g. *Tsuchiya et al.*, 2004; *Hernlund et al.*, 2005; *Tsuchiya and Tsuchiya*, 2006).

However, whether the multi-scale seismic structure can indeed be independently constrained is, in many cases, uncertain. The propagation of seismic waves through the lower mantle is uneven and, almost always, unidirectional. Layering in D" may affect global sets of traveltimes diffracted waves while the LLSVPs may cause large traveltime and waveform perturbations over regional distances even if traveltime differences such as S-ScS and S-SKS are analyzed (e.g., *Ritsema et al.*, 1998; *Wen*, 2001). The (joint) geophysical interpretation of large-scale and fine-scale models of the lower mantle is therefore complicated.

In this paper, we illustrate how shear-wave traveltimes and amplitudes are influenced by both large-scale and fine-scale seismic heterogeneity. We focus on a trans-Pacific cross-section of the lower mantle. The abundant recordings of deep-focus earthquakes in the Fiji-Tonga region at seismic networks across Canada and the United States (Figure 3.2) motivated a large number of studies of the deep mantle beneath the Pacific Ocean. Indeed, much of our understanding of the lower mantle structure and the research cited in the first paragraph of this section originated from the analysis of North American recordings of Tonga-Fiji earthquakes.

We focus on the seismic phases, S, SKS, and SKKS that are recorded over a wide teleseismic distance range across North America. Figure 3.1(a) shows the geometric ray paths of S, SKS, and SKKS and illustrates their complex interactions with the LLSVP and D". S and SKKS propagates through the core of the LLSVP while

SKS skirts its southwestern margin. In addition, S propagates through D" for several thousand kilometers while SKS and SKKS traverse D" orthogonally in different ways, which leads us to hypothesize that the low-velocity zones of Figure 3.1(b) are projections of the LLSVP into 1D velocity profiles.

We hypothesize that the low-velocity anomaly in the tomographic image of Figure 3.1(a) and in the 1D profiles of Figure 3.1(b) have a common origin in the delay of teleseismic shear-wave traveltimes. The contrast in dimensions may be accentuated by the different modeling procedures. The LLSVP in S40RTS may be artificially stretched into a large radial (>500 km) structure due to the predominantly steeply propagating shear waves beneath the Fiji-Tonga region. The anomalies in M1, L2, and KG10 are restricted to the lowermost 200-500 km of the mantle because of the 1D modeling approach.

Using a large set of S, SKS, and SKKS amplitude and traveltimes we evaluate the connection between the LLSVP in S40RTS and the low-velocity structures in M1, L2, and KG10. The sharp discontinuities and gradients in these models cannot be fully constrained by the traveltime and amplitude measurements and are not further discussed. Since our waveform calculations are time-consuming, we limit our analysis to a set of cases focussed on the radial extent of the shear velocity structure and the shear-velocity gradient in D" which is clearly different in the seismic structures of Figure 3.2. We analyze the effects of tomographic damping on traveltimes and amplitudes, evaluate how traveltimes and amplitudes vary with azimuths, evaluate how the different shear velocity gradients in M1, L2, and KG10 affect traveltimes and amplitudes, and determine the influence of thin ultra-low velocity layers.

3.3 Traveltimes and amplitudes

We analyze traveltime differences and amplitude ratios of SKKS and SKS and of S and SKS. The raypaths of S, SKS, and SKKS are shown in Figure 3.1(a) for three

epicentral distances that span the entire distance range of our analysis. Assuming that the outermost core is homogeneous, we expect that the phases SKKS and SKS are affected mainly by southwestern flank of the LLSVP above the core-entry points of SKS and SKKS. S is primarily affected by the LLSVP and D" structure beneath the central Pacific Ocean due to its long diffraction.

Traveltime differences and amplitude ratios of S, SKS, and SKKS minimize the effects earthquake mislocations and velocity heterogeneity in the crust and upper mantle. The time difference of SKKS and SKS has been measured before by *Garnero et al.* (1993); *Sylvander and Souriau* (1996); *Castle and van der Hilst* (2000); *Kuo et al.* (2000) and *Tanaka* (2007). The amplitude of S with respect to SKS has been analyzed previously by *Vinnik et al.* (1989), *Ritsema et al.* (1997) and *Ford et al.* (2006).

Using SKS as a reference phase, we denote the traveltime differences as

$$\delta T_{\mathrm{S}} = T^{\mathrm{obs}}_{\mathrm{S-SKS}} - T^{\mathrm{ref}}_{\mathrm{S-SKS}}, \tag{3.1}$$

and

$$\delta T_{\mathrm{SKKS}} = T^{\mathrm{obs}}_{\mathrm{SKKS-SKS}} - T^{\mathrm{ref}}_{\mathrm{SKKS-SKS}}. \tag{3.2}$$

The amplitude ratios are defined as

$$\delta A_{\mathrm{S}} = \log_{10}\left(\frac{A_{\mathrm{S}}}{A_{\mathrm{SKS}}}\right)^{\mathrm{obs}} - \log_{10}\left(\frac{A_{\mathrm{S}}}{A_{\mathrm{SKS}}}\right)^{\mathrm{ref}}, \tag{3.3}$$

and

$$\delta A_{\mathrm{SKKS}} = \log_{10}\left(\frac{A_{\mathrm{SKKS}}}{A_{\mathrm{SKS}}}\right)^{\mathrm{obs}} - \log_{10}\left(\frac{A_{\mathrm{SKKS}}}{A_{\mathrm{SKS}}}\right)^{\mathrm{ref}}. \tag{3.4}$$

The reference (i.e., 2^{nd}) terms in equations (3.1), (3.2), (3.3), and (3.4) are computed using the Preliminary Reference Earth Model (PREM) (*Dziewonski and Anderson*, 1981) and Global CMT source parameters. Thus, traveltime differences and ampli-

tude ratios are defined as anomalies with respect to PREM. Values of δT and δA equal to 0 imply that the measurements are identical to PREM-predicted values.

Recorded and synthetic waveforms for event 101607I (October 16, 2007, M_W 6.6) at stations CMB at 84.7°, CCM at 104.6°, and HRV at 120.2° illustrate the quality of waveforms for most recordings in our data collection (Figure 3.3). At large distances S, SKS, and SKKS are recorded with a delay with respect to PREM. In addition, the S amplitude is recorded with an anomalously large amplitude on the radial component and it is narrow on the transverse component. These are expected waveform attributes of shear waves propagating through a low-velocity lower mantle.

3.3.1 Fiji-Tonga recordings in North America

We analyze 31 events (1995–2007) with moment magnitudes larger than 6 from the Fiji-Tonga region (Table 3.1). The focal depths are larger than 300 km. The S, SKS and SKKS are impulsive signals that do not interfere with the near-source surface reflections (e.g., sS, sSKS, sSKKS). The event epicenters have latitudes between 13°S and 32°S and longitudes between 170°E and 176°W. We analyze broadband seismograms of these events recorded at the Transportable Array, ANSA Backbone, IRIS/GSN, CNSN, TriNET, BDSN, and PASSCAL networks in North America. The epicentral distances are between 80–130° and source azimuths between 30–60° although most stations in the United States are within the azimuth range of 45–60° (Figure 3.2).

Routine data processing includes lowpass filtering (T > 5 s), instrument deconvolution, and the rotation of the E-W and N-S component recordings into radial (R) and transverse (T) component waveforms. We inspect all traces on the computer to select seismograms with high signal-to-noise ratio, clear S and SKS onsets, and waveforms without obvious source complexity.

3.3.2 SKKS-SKS and SKKS/SKS

The measurements of δT_{SKKS} traveltimes and δA_{SKKS} amplitudes are obtained by waveform cross-correlation using a 30-s long window. The SKKS waveform is Hilbert transformed to account for its $\pi/2$ phase shift with respect to SKS. Errors in the measurement have been evaluated following *Tanaka* (2002). We obtain 477 measurements of δT_{SKKS} and δA_{SKKS} for epicentral distances larger than 90° when SKKS is well developed and separated from SKS. Figure 3.4(a)(b) shows the variation of δT_{SKKS} and δA_{SKKS} as a function of epicentral distance, respectively.

The values of δA_{SKKS} are predominantly positive. δA_{SKKS} increases to a peak value of about 0.5 at an epicentral distance of 105° and decreases at larger distances. *Zhang et al.* (2009) explained the increase in δA_{SKKS} by the early onset of SPdKS diffraction at the critical SKS refraction angle, consistent with the difference time between SPdKS and SKS (*Garnero and Helmberger*, 1998). They showed that high δA_{SKKS} values can be explained by a source-side ultra-low-velocity-zone at the base of the mantle with a thickness of 20 km, and a shear velocity reduction reduction of 30%. Here we investigate whether δA_{SKKS} may be affected by large-scale lower mantle structure.

δT_{SKKS} appears to be affected by the LLSVP. The predominantly positive δT_{SKKS} values indicate that SKKS is delayed more than SKS. Given the slight difference in propagation angles of SKS and SKKS (Figure 3.1), SKKS propagates a longer path than SKS through the core of the LLSVP. A 3–4 s time difference between SKKS and SKS implies that the shear-velocity contrast across the southwestern margins of the LLSVP is about 2%.

3.3.3 S-SKS and S/SKS

We measure δT_{S} traveltimes and δA_{S} amplitudes (Figure 3.4(c) and (d)) in a different manner. At diffraction distances ($> 110°$ for our study region), S (denoted as

SH) on the transverse component broadens and S (denoted as SV) on the R component have complex and variable waveshapes. This complicates time and amplitude measurements by waveform correlation. Therefore, we measure δT_S using SH and SKS onsets and δA_S from SV and SKS peak amplitudes (see also *Ritsema et al.* (1997)). Corrections for upper mantle anisotropy have been made using the SKS splitting tables of *Schutt and Humphreys* (2001). δT_S and δA_S have been measured beginning at 82° and 90°, respectively. We obtained 1174 measurements of δT_S and 823 measurements of δA_S. The large number of measurements at the shortest distances originate from the numerous seismic stations in California.

Both δT_S and δA_S increase with increasing epicentral distance. δA_S increases from 0 at 85° to ∼1.5 at a distance 120°. The increase of δA_S indicates that SV retains a relatively high amplitude. *Ritsema et al.* (1997) explained this observation with the presence of a negative velocity gradient in the lowermost mantle which retards the onset of S diffraction and the attendant amplitude reduction.

The positive values of δT_S at 85° indicate that SH is delayed more than SKS by the LLSVP, akin to δT_{SKKS}. The continuous increase of δT_S to ∼10 s at 110° suggests that the lowermost few hundred kilometers of the LLSVP extends northeastward. The northestern edge is marked by the S wave turning point at 110° because δT_S does not increase for distances larger than 110°.

3.4 Modeling

To understand the trends in traveltimes and amplitudes we analyze a selection of published 1D and 3D models that have been derived from waveform modeling and tomographic inversion. The models are constrained primarily by North American waveform recordings of Fiji-Tonga earthquakes and thus sample the same mantle cross-section as shown in Figure 3.2 and Figure 3.1(a). The 1D models are depicted in Figure 3.1(b).

3.4.1 1D models

Shear velocity profile M1 (*Ritsema et al.*, 1997) was derived from a similar, but smaller, collection of δT_S and δA_S measurements. M1 is identical to PREM to a depth of 2000 km. Below this depth, M1 is comprised of two linear segments. The shear velocity decreases linearly to a value 0.5% smaller than the PREM value at 2700 km depth. Below 2700 km depth, the shear velocity decreases to a value that is 3% lower than the PREM value at the core-mantle boundary.

Model KG10 (*Kawai and Geller*, 2010) is based on waveform inversion of S and ScS waveforms at relatively long (8–200 s) periods. The shear velocity is identical to PREM to a depth of 2500 km. Below 2500 km depth, the shear-velocity profile has multiple segments with alternating negative and positive gradients. The shear velocity decreases from 7.08 km/s (the PREM value) at about 2471 km depth to 6.99 km/s at about 2547 km depth. Between 2547 km and 2819 km, the velocity increases from 6.99 km/s to 7.24 km/s. In the lowermost 70 km of the mantle, the shear velocity decreases to 7.2 km/s at the CMB, a value that is 3.6% lower than the PREM value.

Profile L2 is from *Lay et al.* (2006), who analyzed the shear velocity beneath the central Pacific region from stacks of ScS precursors. L2 is the second of these three velocity profiles for a 240-km ($\sim 4^\circ$) wide sampling region of the lowermost mantle. The shear-velocity structure of L2 is similar to M1 but include several discontinuous shear velocity jumps (0.6% at 2655 km depth) and drops (0.5% at 2520 km, 0.6% at 2800 km, and 1.1% at 2860 km depth).

The authors interpret the differences between the profiles of sampling regions with positive and negative discontinuites in each bin (reflectors U and L) with double crossings of the Pv-pPv phase boundary. The seismic models provides three samples of upper and lower intersections with the phase boundary in a laterally varying thermal regime. So the laterally vanishing lens of pPv material within and near the margin

of a chemically distinct pile is consistent with the seismic reflectivity observation.

3.4.2 3D models

We analyze a cross-section (referred to as T) through S40RTS (*Ritsema et al.*, 2010) and several systematic modification of this tomographic model. The cross-section T is shown in Figure 3.1(a). Its midpoint is at 40°N and 110°W and the great-circle arc crosses the meridian at this midpoint at an angle (i.e. azimuth) of 60° clockwise from North.

Modifications to T are summarized in Table 3.2 and shown in Figure 3.5. In models T_{H1} and T_{H2} the shear-velocity anomalies are set to be zero within the source side (from 0 to 90°) and receiver side (from 90° to 180°) of the cross-section, respectively. T_{H1} and T_{H2} enable us to determine the influence of the LLSVP and the shear-velocity structure beneath the northeast Pacific and North America on the traveltime and amplitude anomalies.

Cross-sections T_{D1} and T_{D2} are based on S40RTS inversions with different applied damping factors. These model let us determine whether the amplitude and traveltimes depend on the strength of shear velocity anomalies in tomographic inversions. T_{D1} is damped less and T_{D2} is damped more than T. Therefore, the shear-velocity variations are smallest (-4.14 to 3.82% in D") in T_{D1} and highest (-8.59 to 8.09% in D") in T_{D2}. In addition, shear velocity variations are smoothest in T_{D1}. However, T_{D1}, T_{D2}, and T yield comparable fit within error to the same tomographic data sets. See *Ritsema et al.* (2007b) for additional discussion.

Our data are associated with source-receiver paths for a range of azimuths and central Pacific mid-points. In addition, model prediction of traveltimes and amplitudes are based on axi-symmetric velocity structures. To examine the variabilty of the amplitude and traveltimes due to the 3D nature of shear-velocity variations in the lower mantle, we compute waveforms for slightly different cross-section through

S40RTS. Models T_{A1} and T_{A2} are cross-sections drawn with more northerly azimuths of, respectively, 40° and 50°.

3.4.3 PSVaxi and SHaxi synthetics

The advent of relatively cheap computer clusters has spurred the development of techniques that are capable of solving the seismic wave equation for complex 2D and 3D structures on the global scale. For example, the 2D hybrid approach of computing synthetic seismograms (e.g., *He and Wen*, 2009), the 2D Cartesian pseudo-spectral approach (*Rondenay et al.*, 2010), and the Spectral-Element Method (SEM) approach (*To et al.*, 2005; *Ni et al.*, 2005) have been used to investigate LLSVP geometry.

Here we use the SHaxi method (*Jahnke et al.*, 2008) and its P-SV companion PSVaxi to compute the full seismic wave field of P-SV and SH motions with the correct 3D geometric spreading. In SHaxi and PSVaxi the computation is performed on a 2D grid in the plane of the great-circle arc. The 2D grid of heterogeneity is expanded to a 3D spherical geometry by rotating the grid around the radial axis passing through the seismic source.

This technique is, from a computational point of view, significantly cheaper than a full 3D approach such as the SEM (e.g., *Komatitsch and Tromp*, 2002b). The computation of synthetic seismograms at frequencies relevant to body-wave frequencies (< 0.1 Hz) can be computed rapidly on modest computing resources. PSVaxi and SHaxi has been used in studies of the D" discontinuity (e.g., *Thorne et al.*, 2007), global seismic scattering (*Jahnke et al.*, 2008), crustal structure (*Yang et al.*, 2007), and ULVZ structure modeling (*Zhang et al.*, 2009).

3.5 Results

3.5.1 1D models

Figure 3.6 shows the fit to δT_S and δA_S by M1, KG10, and L2. As demonstrated previously by *Ritsema et al.* (1997) the negative shear-velocity gradient in the lowermost 200 km of the mantle (in M1) explains the increase of δT_S and δA_S with increasing distance. The high SV amplitudes are the result of the retarded onset of wave diffraction. In PREM, S waves begin to diffract at a distance of 100° (for a 500-km deep earthquake). Diffraction begins at an epicentral distance larger 110° for model M1. The onset of diffraction at a relatively large distance is also evident from the relatively 'sharp' SH waveforms seen at distances larger than 110° (*Ritsema et al.*, 1997) (see also Figure 3.3). The increase of δT_S with distance is due to result of relatively slow S wave propagation through D".

M1 underestimates δT_S between 85° and 105°. This indicates that S is influenced by a low shear-velocity zone above the turning depth of S waves at 85° (i.e., 2500 km). This is well above M1's low-velocity layer in the lowermost (2700–2891 km) mantle.

Model L2 also predicts the increase of δT_S and δA_S with distance since it includes a low-velocity zone in the lowermost mantle with an overall vertical structure akin to M1. The negative shear-velocity gradient in L2 is weaker than in M1. Hence, the increase in δT_S and δA_S at distances larger than 100° is underestimated by L2. Since the low velocity layers in L2 are, like M1, confined to depths larger than 2700 km, L2 also fails to explain the positive δT_S values for the shortest distances. The discontinuous jumps in L2 do not affect the traveltimes and amplitudes.

Model KG10 does not predict the increase with distance of either δT_S and δA_S. Although shear velocities in KG10 are lower than in L2 and M1 model KG10 misses a negative gradient in the lowermost mantle that is necessary to retard the onset of S wave diffraction and hence to boost S amplitudes. The drop in δA_S between 100°

and 110° is related to the strong positive shear-velocity gradient between 2600 km and 2800 km depth in KG10. This is clearly a model prediction that is inconsistent with the observations. However, in contrast to M1 and L2, model KG10 explains the positive δT_S values for the shortest distances since KG10 incorporates a strong shear velocity reductions near the S wave turning point between 85–100°. This observation points to the presence of shear-velocity reductions well above D".

3.5.2 3D models

3.5.2.1 The effects of the LLSVP

Figure 3.7a–d compares the observed amplitude and traveltime anomalies to the predictions for models T, T_{H1} and T_{H2}. The predicted values for δA_{SKKS} are indistinguishable among the models, which demonstrate that large-scale variations of shear velocity in the mantle have little effect on SKKS and SKS amplitudes. The prediction of both T and T_{H1} match the observations which indicates that the traveltime delays are mostly due to the LLSVP in the southwest Pacific. The LLSVP in T (and T_{H1}) produces postive values of δT_S although the value of about 3 s near 85° is underestimated by S40RTS. δT_{SKKS} and δT_S are negative for T_{H2}. Thus, the predominantly high shear-velocity structures beneath the northeastern Pacific and North America reduce the difference traveltimes by up to 2 s.

Predicted values for δA_S for T_{H1} are up to 0.3 larger than for T_{H2} (Figure 3.7c). This indicates that the LLSVP enhances amplitudes of S diffracted waves by perturbing S wave paths through the lower mantle. Nevertheless, models T and T_{H1} underestimate δA_S. It is therefore clear that the LLSVP as imaged by S40RTS does not significantly distort S wave paths that would enhance amplitudes of diffracted waves.

3.5.2.2 The effects of damping

The effects of variable tomographic damping is illustrated in Figure 3.7e–h. The traveltime and amplitude anomalies are slightly larger for model T_{D1} with the weakest damping and thus largest shear-velocity anomalies. The traveltime anomaly δT_{SKKS} differs most among the models. For model T_{D1}, δT_{SKKS} is up to 3 s higher than for model T_{D2}. This demonstrates that the SKKS and SKS traveltime difference is influenced by the contrast in shear velocities at the southwestern margin of the Pacific LLSVP.

δT_S and δA_S are, respectively, 1–2 s and 0.2 smaller for T_{D2}. However the overall trends in the amplitude and traveltime predictions are similar. Therefore, an uncertainty in the strength of the shear-velocity anomalies in tomographic models does not significantly influence the interpretation of trends observed in our collection of difference traveltimes and amplitude ratios.

3.5.2.3 The effects of azimuth

Like the effect of tomographic damping, the predicted traveltime and amplitude anomalies change little if they are computed for cross-sections with slightly different azimuths (Figure 3.7i–l). The most significant effect is seen for δT_S. As shown in Figure 3.7, the shear-velocity reduction within the LLSVP is lowest in T_{A2}. Therefore, shear waves propagating through the LLSVP as imaged by T_{A2} are not as strongly delayed as for T_{A1} and T, and thus δT_S are up to 2 s smaller. Despite the different shape of the LLSVP in cross-section T_{A1}, the traveltimes and amplitude ratios are virtually identical for T_{A1} and T.

3.6 A hybrid model

The model comparisons from sections 4.1 and 4.2 demonstrate that both large-scale structure, as imaged tomographically, and the "fine-scale" layered structure, as imaged by waveform modeling, contribute to the traveltime and amplitude anomalies. Model S40RTS explains the non-zero SKKS-SKS difference traveltimes (δT_{SKKS}), and the positive S-SKS difference traveltimes (δT_{S}) at distances shorter than 100°. This demonstrates how the asymmetric southwesterly position of the LLSVP within cross-section T (Figure 3.1(a)) delay through-going S and SKS waves more than the more steeply propagating SKS waves. In fact, non-zero values of δT_{SKKS} cannot be explained by 1D models.

The relatively rapid rise of δT_{S} to 10 s at 120° and the large values of δA_{S} of up to 1.2 are explained well by the negative shear velocity gradient incorporated in model M1. Models L2, which includes shear velocity reduction with a weaker gradient than M1, underestimates δT_{S} and δA_{S}. Model KG10, which lacks a negative gradient, predicts near-constant values for δT_{S} and an insignificant δA_{S} amplitude ratio, contrary to observations. This indicates that a negative shear velocity gradient in the lowermost mantle is a required feature in seismic models of the Pacific lower mantle. Model KG10 explains values of δT_{S} of +3 s near 85°. This indicates a delay reduction of the shear velocity at the S wave turning depth of 2500 km. Rather than placing this shear-velocity anomaly at the S wave turning depth of 2500 km, we argue that the delay is due to S wave propagation along a $\sim$ 1000 km long path through the LLSVP.

In Figure 3.8, we propose a hybrid model ($\mathrm{T_{HYB}}$) for the Pacific lower mantle which incorporates the key attributes of the models. The overall Pacific lower mantle is described by S40RTS. Included in this image is (1) the M1 shear velocity profile for the lowermost 200 km of the mantle. The profile is confined to the northeastern edge of the LLSVP (40°–60°). (2) A ULVZ, as modeled by *Zhang et al.* (2009), is

embedded at the base of the LLSVP in the source side.

Given model non-uniqueness and the large scatter in our data, and the limited set of phases being used, we refrain from detailed manipulation of the model in order to optimize data fit. By adding the gradient at the lowermost 200km of the mantle, because of the approaching raypaths of SKKS and SKS, δT_{SKKS} and δA_{SKKS} showed barely differences with both amplitude and traveltimes (in Figure 3.7d), with again an average of 3–4 seconds on traveltime residuals. Both models appear to underestimate δT_{S} before 100° and overestimate the data by over 2–3 seconds after 110°. However, the fitting these two models provide looks better overall than the original T. Model $\mathrm{T_{HYB}}$ provides a good fit. It does not fit the increase of δT_{S} and δA_{S} beyond 110° because the M1 profile is cut off at the northeastern extent of the LLSVP.

As discussed by *Zhang et al.* (2009), δA_{SKKS} is affected by a thin ULVZ at the base of the mantle. None of the 1D or 3D considered sofar had an effect on δA_{SKKS}. To match δA_{SKKS}, we add a 20-km thick ULVZ layer with a shear-wave reduction of 30% compare to PREM model. Additionally, we sent a local negative gradent of -1.25% – -2.5% in the lowermost 200km of the mantle, with the extention from 40° to 60° in our T1 model. The reason to select this range is to largely keep the amplitude anomaly and avoid the delay it will cause the SKS waves at the same time, we name our new model T_sum.

3.7 Discussion

Compared to the scale of the structure travel times could solve, the amplitude of seismic waves is more sensitive to the rough, smaller-scale structure and boundaries, especially for those gradient changes, which is under the resolution of tomography. We investigate how the traveltimes and amplitudes are affected by the broad and smooth velocity structure or small and sharp boundary-like structure, and find out that the waveforms response differently to multiple scales and different types of structures,

with a combined complexity from both traveltimes and amplitudes. Tomography are damped models designed to explain global traveltimes. Amplitudes are not part of it. They depend on gradients. Tomography is smooth, no edges, no strong traveltime gradients (*Ritsema et al.*, 1998) or waveform anomalies (*Ni et al.*, 2003). 1D models apply to limited region but cannot represent velocity structure that is asymmetrically placed between the source and receiver.

For tomography models, the differences in Figure 3.7e–h and i–l in the curves reflects the uncertainty due to damping and azimuths. The damping has little effect on the amplitude and traveltime variations with distance. Compared to damping effects, 3D structure differences due to azimuths seems to provide large values to traveltime scatters while contribute almost nothing to amplitude variations. The prediction of models with different azimuths and damping show that 3D variations and damping comprise part of the observed scatters but not dominate for both traveltime and amplitudes. The smoothed-out tomography structure could explain a large portion of the positive values for δT_{S}.

Due to the tradeoff of the large-scale reduction in KG10 and the similar effect on δT_{S} with S40RTS, we confirm that it is likely that the LLSVP is actually reflected as the radial velocity reduction within the mid-mantle depth for 1D models. Instead of attribute the velocity reduction in KG10 to phase transitions in basalt from Mg-pv to Mg-ppv (*Tsuchiya and Tsuchiya*, 2006) as the authors stated, we would rather believe that it is caused by LLSVP, which is a representation of the reduction in a radial extent.

KG10 from *Kawai and Geller* (2010) has a large velocity reduction to more than 5% peaked at the depth of 2550km. It is designed to match ScS-S times and waveforms. It also matches S-SKS times at the same distances. The comparison of δT_{S} between KG10 model and S40RTS tomography models share a common feature of about 5 s time delay, which can be mainly attributed on S wave interacted with

the LLSVP structure. However, it is worthy noticing that KG10 and even the tomography models could not provide the data variations along distances in the data measurements of δT_S. Moreover, the amplitudes don't show agreeable value with the data measurements, indicating again that the 3D structure is not the main attribute to the anomaly in SV amplitudes. Instead, the low-velocity layer at the base of the mantle like M1 and L2 provide can give us a trend with increasing times and with enhanced SV amplitudes. This means a finer or sharper structure similar as M1 or L2 provide must be present to provide the variations along distances. This exercise leads to a model of the Pacific governed by S40RTS-like large-scale velocity structure and layering as seen in L2.

The gradient, both represented by L2 and M1, may exist as sharper discontinuities like L2 shows to correspond with the reflection phases result but has to be a even shaper reduction to be consistent with SV amplitudes. It is noticed that L2 model in *Lay et al.* (2006) is not a universal applied model within the whole Pacific region, but with a thinning-out ppv layer to the northeast direction. Synthetic tests with all 3 bins of the model series show a limited influence on our measurements. We here just consider L2 as a representation of all bins. For the first increasing and later decreasing velcities at the bottom 200 km of the mantle, the authors in both *Kawai and Geller* (2010) and *Lay et al.* (2006) have mentioned the effects from the double-crossing that possibly exist (*Hernlund et al.*, 2005).

Not much variation has been found with our 1D models in Figure 3.1(b) for SKKS/SKS pair traveltime and amplitude ratio measurement, neither for the tomography 3D structures in Figure 3.5. The amplitude ratio of SKKS and SKS, as is discussed in *Zhang et al.* (2009), is mainly affected by the existence of the fine-scale structures ULVZs. Waveforms and limited array analysis of SPdiffKS since *Garnero et al.* (1993) has been used to study ULVZs. This ULVZ structure is possibly located right at the southwest Pacific region where SKS/SKKS wave enter the core, which

skirts the LLSVP and more sensed by SKS instead of SKKS wave paths. The ULVZs are too fine to be imaged in tomography. Further complexity is indicated by short-period signal scattering (*Cormier*, 2000; *Hedlin and Shearer*, 2000). Scattering may be linked ULVZs although it must be emphasized that a significant portion of the lower mantle is as yet unexplored for potential scatterers.

Attenuation, on the other hand, is another possibility that can affect seismic amplitudes. Attenuation in the lower mantle, where our measurements of S and SKS wave paths separate the most, is comparatively hard to detect under current investigations. *Lawrence and Wysession* (2006) measured the t* difference between the seismic phases ScS and S, which has more sensitivity to the deeper part of mantle. Their results reflect a possibly high Q layer at approximately the bottom 1000 km of the mantle. Simple synthetic tests can show that a high Q at the bottom, will add an influence on the phase S more, and enhance it's amplitude, which could add a contribution to δA_{S}. The temperature and dynamics in the lowermost mantle which are related to attenuation, if known, could provide us with further constraints.

With the phases we use to achieve the 1D models, it is due to the ray path coverage that we attribute the anomaly to the lowermost 500 km but the anomaly above could still affect. Part of the LLSVP reflected in tomography images is reflected in 1D models, both of which can affect traveltime tremendously, but not the amplitudes. While the finer-scales layering of D" , which are basically under the resolution of tomography images, affect amplitudes the most. The high amplitude of δA_{S} and δT_{S} in longer distances indicate that the M1-like negative gradient structure may extend further northeast than the tomography model suggests. With our modeling, we clarify the picture of the lower mantle region with multi-scale structures and evaluate the sensitivity of the tomography models. Overall, tomography models do not work well to model the amplitude with its smooth structures.

In our study, we are not keen on the lateral extension of those sharp structures,

which will, for certain, affect the amplitude with its appearances and disappearance. Only within the modeling of T_{HYB} model, we add a local ULVZ and local M1-like structure to model its approximate lateral location at the same time, and the results generally fit. It further tells us the complexity of adding the lateral dimensional, with the possibility of complicated tradeoffs. Under the resolution of current tomography models, localized structures that could not be imaged could contribute most to the amplitudes in particular. For instance, the ULVZs as discussed by *Garnero and Jeanloz* (2000), could be tradeoff with CRZ (core rigid zone) and CMTZ (core-mantle transition zone). Additionally, ULVZ can also contribute to exaggerated Sdiff amplitude if placed in the far source side.

It is important for us to have a "integrated" view to look at the regional and global features, with the representation of the Pacific lower mantle structure reflected in both tomography and 1D models, and the resolution of finer-scale structures in 1D models instead of tomography images. Amplitude provide an independent angle for to evaluate the tomography images.

3.8 Conclusions

Shear-wave traveltimes and amplitudes recorded across regional networks of seismic stations are affected by both large-scale structure in the lower mantle and fine-scale layering in D". S-SKS and SKKS-SKS traveltime differences are larger than PREM predictions because of the relatively long propagation paths of S and SKKS through the large-low shear velocity province (LLSVP) in the lower mantle beneath the southwest Pacific. The relatively S/SKS and SKKS/SKS amplitudes are due to a near-receiver negative shear velocity gradient of $\sim$2% in the lowermost several hundred kilometers of the mantle and the near-source presence of a thin ($\sim$ 20 km) ultra-low velocity layer with 20–30% shear velocity reduction at the base of the mantle. While these seismic characteristics of the deep mantle have been resolved previously,

our study demonstrates that the modeling of basic attributes such as wave travel-times and amplitudes requires a multi-scale approach that considers but cannot be exclusively focused on large-scale or fine-scale structure. Large-scale structure may compromise the resolution of fine-scale models of the lowermost mantle, and a hybrid model is in need to develop a unified picture of the Pacific lower mantle.

Table 3.1: Fiji-Tonga earthquakes

Date	Lat (°S)	Lon (°E)	Depth (km)	M_W
1991/12/03	26.31	178.57	581.0	6.3
1992/07/11	22.28	-178.51	381.0	7.2
1993/04/24	17.73	179.81	600.0	6.2
1993/08/07	23.87	179.82	555.0	6.7
1994/03/09	17.77	-178.50	564.0	7.6
1994/10/27	25.79	179.35	549.0	6.6
1995/01/17	20.87	-179.23	637.0	6.3
1995/04/13	13.40	170.40	640.0	6.1
1996/08/05	20.69	-178.31	550.0	7.4
1996/10/19	20.41	-178.51	591.0	6.9
1997/05/25	32.12	179.79	333.0	7.1
1997/09/04	26.57	178.34	624.7	6.8
1998/01/27	22.41	179.04	610.1	6.4
1998/03/29	17.55	-179.09	537.2	7.1
1998/05/16	22.23	-179.52	586.1	6.8
1999/06/26	17.96	-178.19	590.4	6.0
2000/01/13	17.61	-178.74	535.0	6.2
2000/05/04	17.91	-178.52	515.8	6.4
2000/06/14	25.52	178.05	604.6	6.4
2000/08/15	31.51	179.73	357.7	6.6
2001/04/28	18.06	-176.94	351.8	6.8
2002/06/30	22.20	179.25	620.4	6.4
2002/08/19	21.70	-179.51	580.0	7.6
2003/01/04	20.57	-177.66	378.0	6.5
2007/10/05	25.19	179.46	509.4	6.5
2007/10/16	25.77	179.53	509.3	6.6
2008/01/15	21.98	-179.54	597.6	6.5
2008/04/18	17.34	-179.02	553.8	6.3
2008/07/03	23.37	-179.78	581.2	6.2
2008/07/19	17.34	-177.31	391.0	6.4
2009/02/18	27.42	-176.33	25.0	7.0

Table 3.2: Models

3D models	**Remarks**
T	S40RTS (see Figure 3.1(b))
T_{H1}	T but $\delta V_S = 0$ from 0° to 90°
T_{H2}	T but $\delta V_S = 0$ from 90° to 180°
T_{A1}	S40RTS with azimuth 40°
T_{A2}	S40RTS with azimuth 50°
T_{D1}	S40RTS inversion damped weakly
T_{D2}	S40RTS inversion damped strongly

1D Models	**Remarks**
M1	Ritsema et al. (1997)
L2	Lay et al. (2006)
KG10	Kawai and Geller (2010)

Hybrid Models	**Remarks**
T_{HYB}	T plus ULVZ plus M1 (from 40° to 60°)

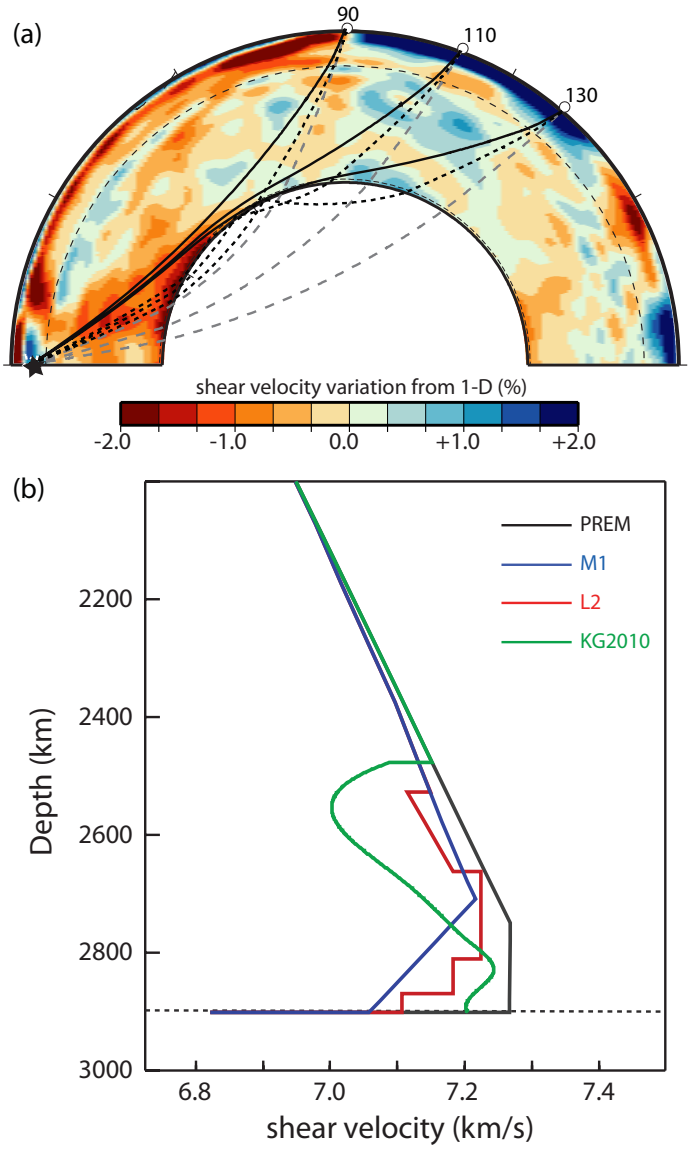

Figure 3.1: Cross-section of tomographic model S40RTS is plotted together with 1D shear profiles: (a) Shear velocity perturbation from PREM in a vertical cross-section (T) through the mantle according to model S40RTS (*Ritsema et al.*, 2010). The cross-section T includes the Fiji-Tonga source region (indicated by the star) and North America. The solid, dashed and dotted lines are S, SKS, and SKKS ray paths for epicentral distances of 90°, 110° and 130° calculated using the M1 (*Ritsema et al.*, 1997) velocity profile. (b) Shear-velocity profiles for (black) PREM (*Dziewonski and Anderson*, 1981), (blue) M1 (*Ritsema et al.*, 1997), (red) L2 (*Lay et al.*, 2006), and (green) KG10 (*Kawai and Geller*, 2010) for the Central Pacific.

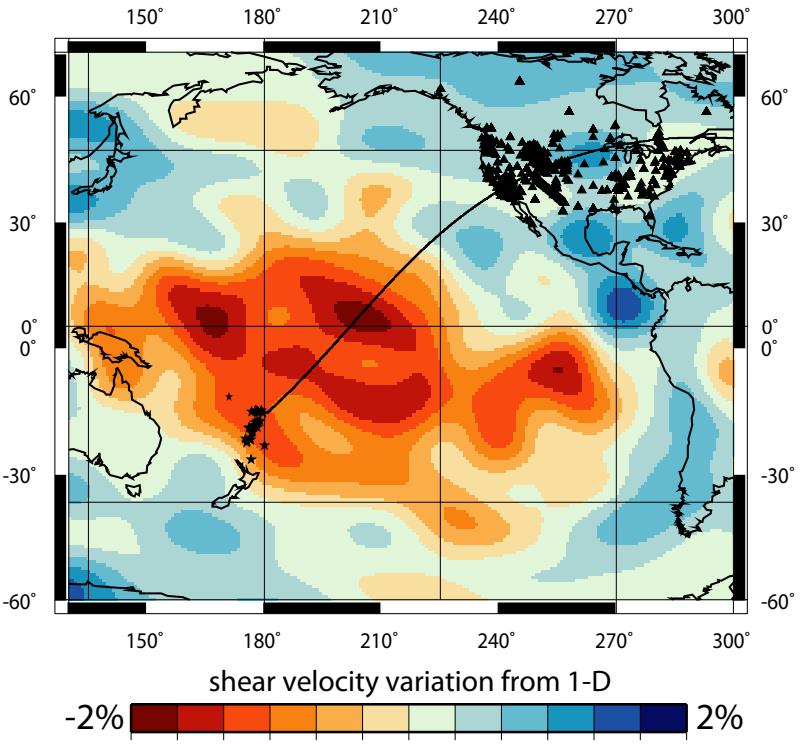

Figure 3.2: Map of event-receiver geometry are shown with the reflection points of SKS, SKKS and Sdiff along great circle raypaths. The events (star) and receivers (triangle) are from Fiji-Tonga region and North America region, separately.

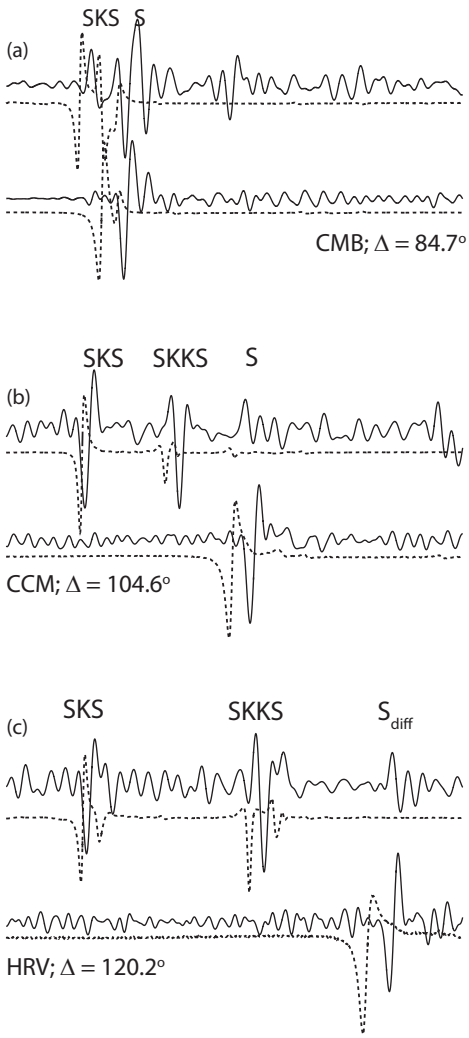

Figure 3.3: An example of (solid lines) recorded and (dashed lines) synthetic waveforms (velocity) of SKS, SKKS and S at stations (a) CMB, (b) CCM and (c) HRV for the October 16, 2007 ($H = 512$ km, $M_W = 6.6$) Fiji Islands earthquake. The radial components are plotted above the transverse component waveforms.

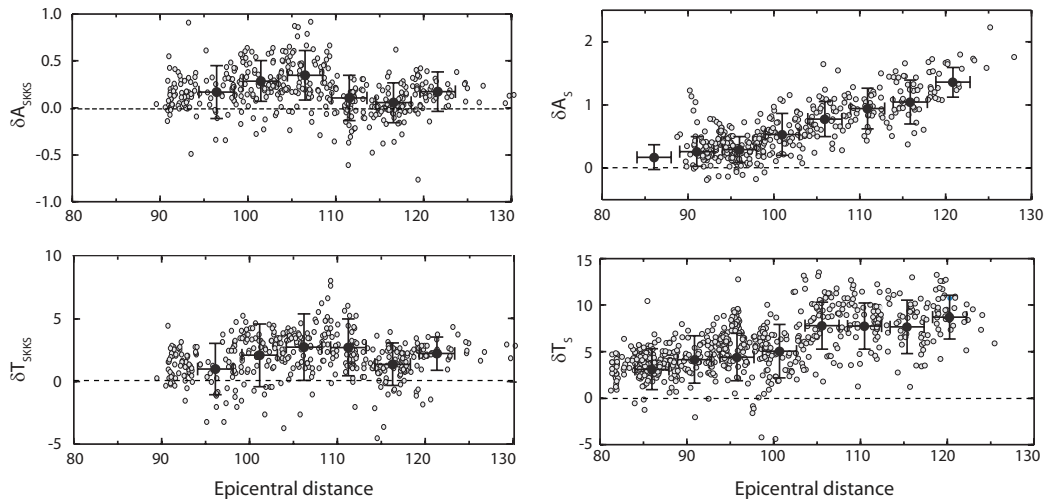

Figure 3.4: Measurements (grey circles) and average values (including 1σ uncertainties) of S/SKS and SKKS/SKS, determined in 5°-wide overlapping bins, of (a) δA_{SKKS}, (b) δA_{S}, (a) δA_{SKKS}, (b) δA_{S}, (c) δT_{SKKS}, and (d) δT_{S}.

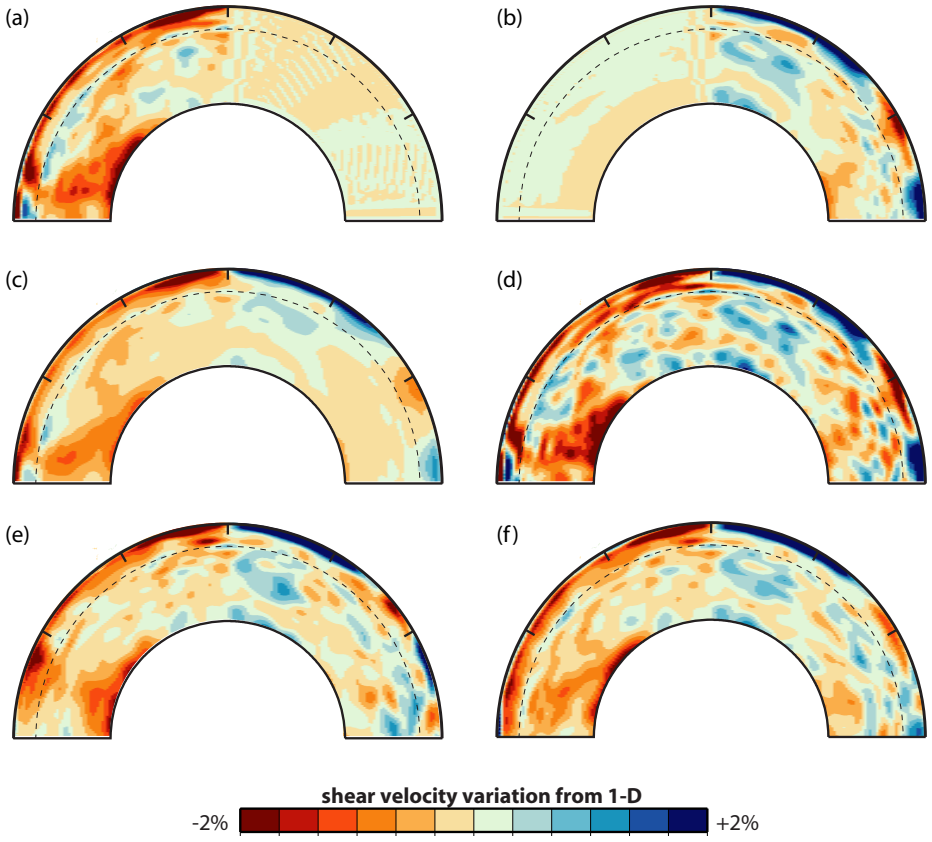

Figure 3.5: Cross-sections of 3D models: (a) T_{H1}, (b) T_{H2}, (c) T_{D1}, (d) T_{D2}, (e) T_{A1}, (f) T_{A2}. See also Table 3.2.

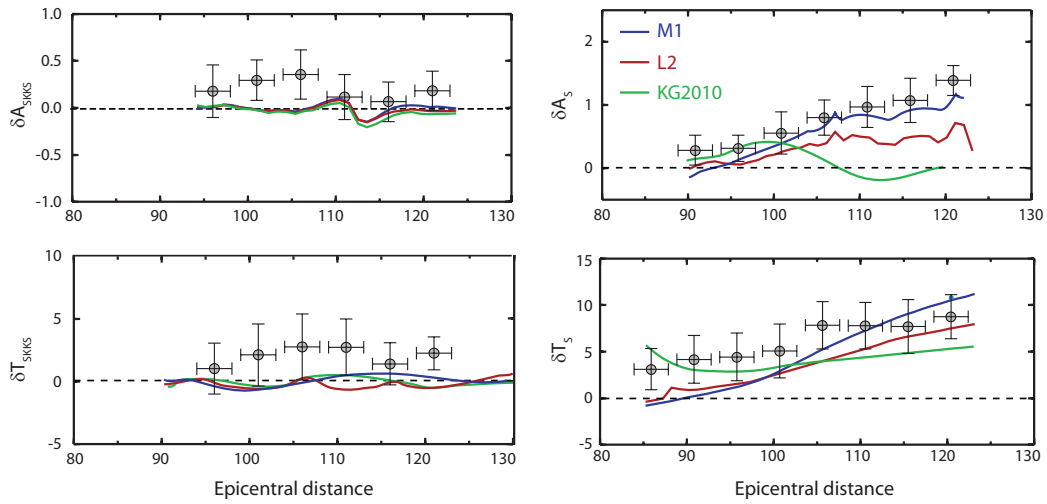

Figure 3.6: Model predictions using 1D model M1, L2, KG10 are shown with observed average values. Values of δA_{SKKS}, δA_{S}, δT_{SKKS}, and δT_{S} for 1D profiles M1 (*Ritsema et al.*, 1997), L2 (*Lay et al.*, 2006), KG10 (*Kawai and Geller*, 2010) are plotted.

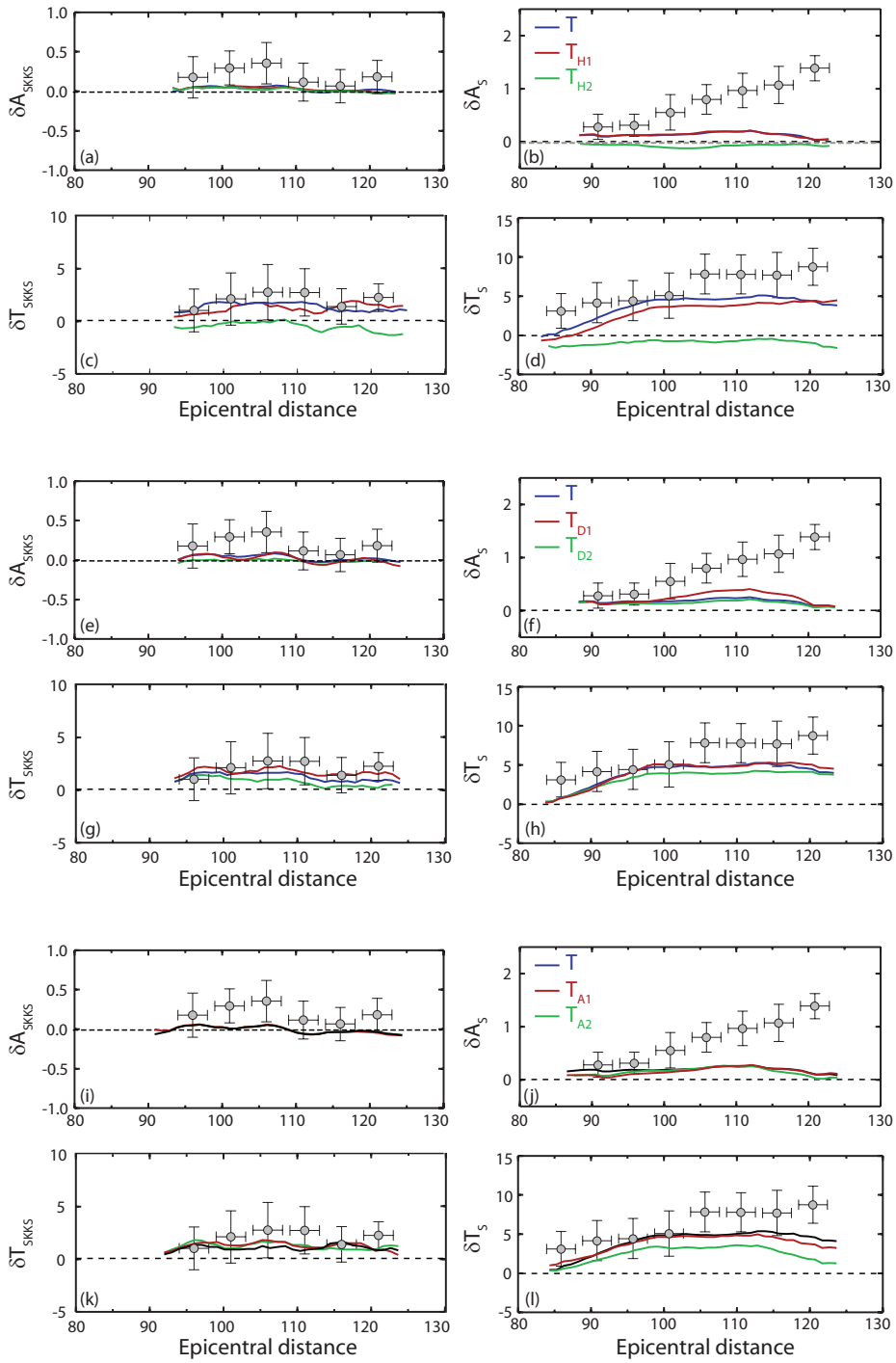

Figure 3.7: Model Predictions using multiple 3D models are shown. Measurements and model predictions of (a, e, i) δA_{SKKS}, (b, f, j) δA_{S}, (c, g, k) δT_{SKKS}, and (d, g, l) δT_{S}. Blue lines are the traveltime and amplitude predictions for T. The red lines are the prediction for $\mathrm{T_{H1}}$ (in a, b, c, d), $\mathrm{T_{D1}}$ (in e, f, g, h), and, $\mathrm{T_{A1}}$ (in i, j, k, l). The green lines are the prediction for $\mathrm{T_{H2}}$ (in a, b, c, d), $\mathrm{T_{D2}}$ (in e, f, g, h), and, $\mathrm{T_{A2}}$ (in i, j, k, l).

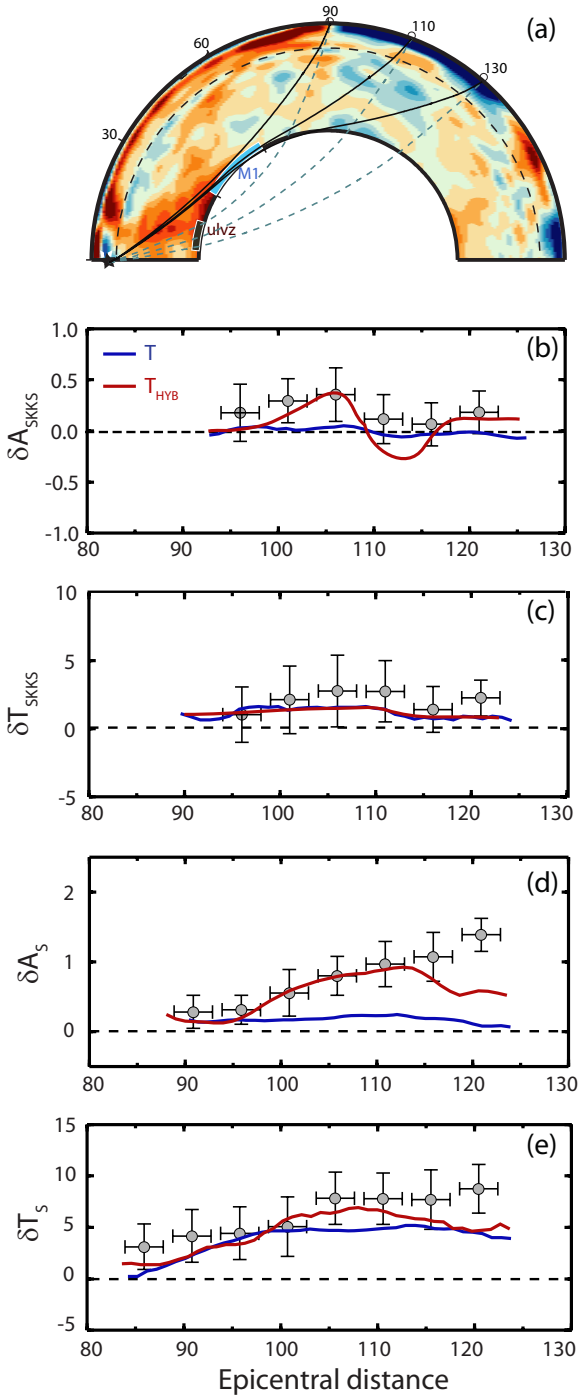

Figure 3.8: A hybrid model is put together to fit the observations. Measurements and model predictions of (a) δA_{SKKS}, (b) δA_{S}, (c) δT_{SKKS}, and (d) δT_{S}. The predictions are determined for cross-sections (blue) T, and (red) $\mathrm{T_{HYB}}$.

CHAPTER IV

An analysis of SS precursors using spectral-element method seismograms

4.1 Abstract

The traveltimes of underside shear-wave reflections (i.e., SS precursors) are widely used data for mapping the topography of phase transitions in the upper mantle. Here, we examine the accuracy of ray theory in estimating the contribution of shear-velocity heterogeneity in the mantle to SS-S400S, SS-S670S and S400S-S670S traveltimes. We analyze stacks of spectral-element method waveforms computed for 34 shallow earthquakes and 16,020 globally distributed virtual seismometers. The waveforms are computed for three versions of the S20RTS model in which the strength of the volumetric shear-velocity perturbations within the layered structure of the Preliminary Reference Earth Model (PREM) varies. We find that ray-theoretical corrections account for only 50% of the traveltime variation due to large-scale velocity heterogeneity. For current tomographic models, this translates into unpredictable long- and short-wavelength errors in maps of phase-transition depth variations of about 5 km, roughly 10% of published variations in phase transition depths. However, relative errors may be significantly larger if ray-theoretical traveltime corrections are based on (forthcoming) models of shear-velocity with much stronger heterogeneity at the

smallest scales.

4.2 Introduction

The stacking of SS precursors is a widely used seismological technique for the imaging of the transition zone (TZ) in the upper mantle. The seismic phase SS is an underside shear-wave reflection off Earth's surface halfway between an earthquake and seismic station (Figure 4.1). The SS signal on a transverse component seismogram has a relatively high amplitude over a broad teleseismic distance range (70–160°). SS can be analyzed for seismograms for a diverse set of earthquake-station pairs that render a global distribution of SS reflection points.

Underside reflections off the Moho (i.e., SmS) and off seismic discontinuities in the upper mantle (i.e., S400S and S670S) at 400 and 670 km depth — depths according to PREM (*Dziewonski and Anderson*, 1981) — are recorded up to four minutes before SS, hence the name 'precursors'. Although these internal reflections have small amplitudes, summation (i.e. stacking) of tens to hundreds of seismograms can bring precursory signal above noise level. The stacking of precursors is, in principle, straightforward because S670S and S400S have predictable slownesses (i.e. wave incidence angles) and they are not obscured by major high-amplitude phases.

SS precursor analysis yields excellent upper mantle constraints of both continental and oceanic regions. Since the global studies by *Shearer* (1991) and *Shearer and Masters* (1992), the analysis of SS precursors has progressed rapidly. A large number of studies have linked seismic reflections to the mineral structure of the upper mantle, the presence of melt, and discontinuity topography on a global and regional scale. For reviews, see *Shearer* (2000), *Helffrich* (2000), *Kind and Li* (2007), and *Deuss* (2009).

SS precursors are particularly useful for estimating the depths of the 400 and 670 boundaries and for estimating the role of the TZ in heat and mass transfer between the upper and lower mantle. The thermodynamic Clapeyron slopes of the 400 and

670 have opposite signs (e.g., *Katsura and Ito*, 1989; *Bina and Helffrich*, 1994; *Frost*, 2008). As a result, the 400 is expected to be shallower and the 670 is expected to be deeper in relatively cool transition zone regions (such as subduction zones). Vice versa, in relatively warm mantle regions, the 400 is deeper and the 670 is shallower than the global average values.

The traveltime differences between SS, S400S, and S670S are the key probes of phase transition depths and, indirectly, temperature variations within the transition zone. As discussed by *Deuss* (2009), the TZ is estimated to be, on average, 242±2 km thick, nearly 30 km thinner than in PREM. The 670 is deepest beneath subduction zones (e.g., *Flanagan and Shearer*, 1998; *Gu et al.*, 2003; *Houser et al.*, 2008; *Lawrence and Shearer*, 2008) and the 400 is deepest beneath the Pacific (e.g., *Deuss*, 2007; *Gu et al.*, 2009; *Houser and Williams*, 2010). The long-wavelength variation in transition zone thickness of about 50 km correlates with the velocity variations seen tomographically and reflect large-scale upper mantle dynamics. The anticorrelation between 400 and 670 topography may be expected if one considers variations of the geotherm across the entire upper mantle (e.g., *Ritsema et al.*, 2009b). In addition, phase transition topography may be complicated by the transformation of garnet (e.g., *Hirose*, 2002) or the effects of mechanical mixing (*Xu et al.*, 2008).

Another source of uncertainty arises from the contribution of shear-velocity heterogeneity in the crust and mantle on the traveltimes of SS and its precursors. Although numerous studies suggest that ray-theoretical traveltime calculations may be imprecise due to the long-wavelength nature and the broad sensitivity kernels of SS waves (*Chaljub and Tarantolla*, 1997; *Neele et al.*, 1997; *Neele and de Regt*, 1999; *Zhao and Chevrot*, 2003; *Dahlen*, 2005), traveltime contributions due to shear-velocity heterogeneity has so far been estimated by ray-tracing through tomographic velocity models. A notable exception is the the study of *Lawrence and Shearer* (2008) who analyze stacks of waveforms under the assumption that its sensitivity can be approximated

by a stack of sensitivity kernels.

Here, we examine the potential errors in depth estimates of the 400 and 670 as inferred from SS precursor analysis when ray-theory and long-wavelength tomographic models are used to estimate the contribution of shear-velocity heterogeneity to traveltimes. We complement theoretical work (e.g., *Zhao and Chevrot*, 2003; *Dahlen*, 2005) with a study of synthetic seismograms that mimics the analytical procedures commonly applied to data. We compute 3D waveforms spectral-element method (SEM) for three tomographic models and determine how inaccurate ray-theoretical corrections project as artifacts in traveltime maps of synthetic waveform stacks.

4.3 3D wave simulations and processing

We employ the SEM developed by *Komatitsch and Tromp* (2002a) to compute hour-long transverse-component waveforms. With computational resources available to us, we can compute teleseismic seismograms at frequencies shorter than about 60 mHz. This upper limit of the frequency band is sufficiently high to synthesize the relatively long-period waveforms of SS and its precursors. The waveforms are bandpass filtered using a cosine-square filter with cutoff frequencies of 4 mHz and 50 mHz and corner frequencies of 8 mHz and 40 mHz.

We compute waveforms for three 3D models, which we refer to as T1, T2, T3 (Figure 4.2). T1, T2 and T3 are models of shear-velocity perturbations in the mantle from the transversely isotropic PREM. They are derived from the same data and modeling approaches used to derive model S20RTS (*Ritsema et al.*, 2004) but the damping in the tomographic inversion has been adjusted (e.g., *Ritsema et al.*, 2007a). Model T2 is the same as S20RTS. Models T1 and T3 are more strongly and weakly damped models. Therefore, shear-velocity variations in T1 are smoother and weaker than in S20RTS and they are the strongest in model T3. Models T1 and T3 represent the variation in the strength of shear-velocity heterogeneity resolved by the most

recently derived global models. We do not modify the seismic structure of the crust nor do we modify the depths of the 400 and 670 velocity discontinuities. Thus, T1, T2, and T3 include only volumetric perturbations of shear velocity that are embedded in PREM's layered structure.

We simulate waveforms for 34 earthquakes at a uniform depth of 20 km and they are distributed over the globe (Figure 4.3). The earthquakes have the same (vertical dip-slip) mechanism as event 101607I (October, 16 2007 21:05:43) from the global CMT catalog to maximize the teleseismic SS radiation pattern. We compute transverse component seismograms at 16,020 virtual seismic stations on a global grid with $2^\circ \times 2^\circ$ spacing. This yields a fairly uniform distribution of SS reflection points and a density that exceeds 700 per $10^\circ \times 10^\circ$ across the globe.

4.3.1 Definitions of traveltime anomalies

Differences in traveltimes between SS (T_{SS}), S400S (T_{S400S}) and S670S (T_{S760S}) are defined as:

$$\Delta T_{400} = T_{SS} - T_{S400S}, \tag{4.1}$$

and

$$\Delta T_{670} = T_{SS} - T_{S670S}, \tag{4.2}$$

and the difference traveltime between S400S and S670S is defined as

$$\Delta T_{400-670} = T_{S400S} - T_{S670S}. \tag{4.3}$$

ΔT_{400} and ΔT_{670} are the two-way traveltimes of shear waves between the surface and the 400 and 670, respectively. $\Delta T_{400-670}$ is the two-way shear-wave traveltime through the TZ.

Anomalies of these traveltimes with respect to the PREM are defined as

$$\delta \mathrm{T}^{1\mathrm{D}} = \Delta \mathrm{T}^{\mathrm{SEM}} - \Delta \mathrm{T}^{\mathrm{PREM}}, \tag{4.4}$$

and with respect to models T1, T2 and T3 as

$$\delta \mathrm{T}^{3\mathrm{D}} = \Delta \mathrm{T}^{\mathrm{SEM}} - \Delta \mathrm{T}^{3\mathrm{D}}. \tag{4.5}$$

Here, ΔT applies to either $\Delta \mathrm{T}_{400}$, $\Delta \mathrm{T}_{670}$ or $\Delta \mathrm{T}_{400-670}$. $\Delta \mathrm{T}^{\mathrm{SEM}}$ is the traveltime difference measured in the SEM waveforms by waveform correlation. $\Delta \mathrm{T}^{\mathrm{PREM}}$ and $\Delta \mathrm{T}^{3\mathrm{D}}$ are the ray-theoretical traveltimes computed for PREM and for the 3D models (e.g., T1, T2, or T3). $\delta \mathrm{T}^{1\mathrm{D}}$ is expected to reflect the 3D velocity heterogeneity. $\delta \mathrm{T}^{3\mathrm{D}}$ is expected to be 0 if ray theory accurately describes long-period SS traveltimes. Thus, non-zero values of $\delta \mathrm{T}^{3\mathrm{D}}$ quantify the inaccuracy of ray-theoretical SS traveltime calculations.

Figure 4.4 compares T1, T2, and T3 seismograms for a window that includes the SS, S400S, and S670S signals based on an event beneath the North Pacific Ocean and a station beneath the western Indian Ocean at an epicentral distance of 124°. The surface reflection point of SS is at 10°N, 115°E in the South China Sea. Note that $\Delta T_{400-670}$, which can be approximated by the time between the S400S and S670S signal maxima, is several seconds shorter than the PREM and the S20RTS traveltime predictions (i.e., $\delta T^{1\mathrm{D}} <0$ and $\delta T^{3\mathrm{D}} < 0$), indicating that ray theory overestimates the shear-wave propagation time though the high-velocity TZ beneath the South China Sea. It is this signal that we map using the stacking of SEM waveforms.

4.3.2 Stacking and traveltime measurements

The amplitudes of S400S and S670S are only several percent of the SS amplitude due to the relatively low impedance contrast at the 400 and the 670. When analyzing

recorded waveforms, trace summation (i.e. 'stacking') is necessary to bring the S400S and S670S signals above noise level. We stack SEM waveforms following a stacking procedure that is commonly applied to data. In this procedure, we align the waveforms on the SS signal, define the arrival time of SS to be 0, multiply waveforms with a negative SS polarity by -1, and normalize the waveforms by dividing them by the peak SS amplitude.

The S400S and S670S waveforms are 120-s long segments centered on PREM-predicted arrival times of S400S and S670S, denoted as τ_{400} and τ_{670} and calculated using the method of *Crotwell et al.* (1999). The stack of the S400S (i.e., S^{400}) and S670S (i.e., S^{670}) signals involves a sum of N traces:

$$S^{400}(t) = \sum_{k=1}^{N} s_k(t - \tau_{400}^{(k)} - 60, t - \tau_{400}^{(k)} + 60), \tag{4.6}$$

and

$$S^{670}(t) = \sum_{k=1}^{N} s_k(t - \tau_{670}^{(k)} - 60, t - \tau_{670}^{(k)} + 60). \tag{4.7}$$

When determining stacks with respect to the ray-theoretical traveltimes of models T1, T2, and T3, τ_{400} and τ_{670} are computed by ray-tracing through the 3D models.

The stacks are determined for a selection of N seismograms with common SS reflection points in a circular cap with a midpoint x_0 and a radius of 10°. A selection of N waveforms have ray-theoretical SS surface reflections points that fall within a circle about a center x_0 and a radius of 10°. By determining stacks for x_0 that are uniformly spaced by 5° across the globe, we map the global variation of δT^{1D} and δT^{3D}. Each of the stacks includes at least $N = 700$ traces (Figure 4.3). The traveltimes with respect to PREM (δT^{1D}) and with respect to the 3D models (δT^{3D}) are estimated by cross-correlating the stacked SS, S400S, and S670S waveforms.

4.3.3 An analysis of PREM synthetics

To determine artifacts that arise due to the stacking procedure and incomplete data coverage, we first analyze stacks of PREM synthetics. The PREM waveforms have been determined using the transversely isotropic PREM model while the ray-theoretical traveltimes have been calculated for the "equivalent" isotropic PREM model as implemented in the TauP code by *Crotwell et al.* (1999). The slight difference in the implementation of the transverse isotropy structure between 80 and 220 km depths yields a constant traveltime difference of about -1.0 s for δT_{400}^{1D} and δT_{670}^{1D}. This signal has been subtracted from the maps by resetting the mean values of δT_{400}^{1D} and δT_{670}^{1D}.

Figure 4.5 shows maps of $\delta \mathrm{T}^{1D}$, plotted at the cap centers. The variation of δT_{400}^{1D} and δT_{670}^{1D} are less than 0.1 s and the variation in $T_{400-670}^{1D}$ is, at most, 0.2 s. The largest 'traveltime errors' correspond to measurements with relatively low cross-correlation coefficients (< 0.9) between the stacked SS, S410S, and S660S waveforms and inhomogeneous sampling of the SS slowness range. Nevertheless, the traveltime variation of 0.2 s in these PREM stacks is much smaller than the variation resolved in the stacks of SEM waveforms for T1, T2, and T3. Thus, the signal that we will discuss in the next section does not originate from the stacking method or the inhomogeneous data coverage.

4.4 Results

4.4.1 Maps of $\delta \mathrm{T}^{1D}$ and $\delta \mathrm{T}^{3D}$

Figure 4.6 shows maps of $\delta \mathrm{T}^{1D}$ determined from the stacks of the SEM synthetics for models T1, T2, and T3. As expected, the large-scale variation of δT^{1D} is similar to the variations of shear-velocity heterogeneity in T1, T2, and T3 (compare Figure 4.6 with Figure 4.2). Since velocity heterogeneity is largest in model T3,

the traveltimes variation is largest for T3. δT^{1D}_{400} and δT^{1D}_{670} are stronger and exhibit longer-wavelength variations than $\delta T^{1D}_{400-670}$ because shear-velocity heterogeneity in the uppermost mantle are relatively strong and broad.

δT^{1D}_{400} and δT^{1D}_{670} reflect the vertically integrated traveltime through the upper mantle. The traveltime variations is primarily determined by the strong shear-velocity heterogeneity in the uppermost mantle. Hence, the ridges and continents stand out as positive and negative traveltime delays, respectively. $\delta T^{1D}_{400-670}$ correlates with the shear-velocity structure in the TZ. It is negative beneath the western Pacific, South America, the central Atlantic and along the Atlantic coasts of Africa. In these regions, the shear velocity is relatively high in T1, T2, and T3.

The amplitude of $\delta \mathrm{T}^{3D}$ ranges from about 1.0 s (for T1) to 3.0 s (for T3) (Figure 4.7). This is significantly smaller than the variation of $\delta \mathrm{T}^{1D}$, which indicates that the ray-theoretical corrections remove a significant portion of the traveltime signal seen in $\delta \mathrm{T}^{1D}$. It appears that the long-wavelength variations (e.g., subducting zones and ocean-continent contrasts) are explained best by ray theory since a long-wavelength signal in $\delta \mathrm{T}^{3D}$ is not as dominant as in $\delta \mathrm{T}^{1D}$.

However, the non-zero values of $\delta \mathrm{T}^{3D}$ clearly demonstrate that the ray-theoretical SS traveltimes do not describe the traveltimes of SS and SS precursors exactly. In particular, the peak-to-peak variation in $\delta T^{3D}_{400-670}$ is only a factor of two smaller than the peak-to-peak variation in $\delta T^{1D}_{400-670}$. Moreover, they do not clearly correlate with the shear-velocity variations in model T1, T2 and T3 and, therefore, may be interpreted as small-scale thickness variations of the TZ.

4.4.2 Spectra of $\delta \mathrm{T}^{1D}$ and $\delta \mathrm{T}^{3D}$

To emphasize that the spatial variation of $\delta \mathrm{T}^{3D}$ comprises a short-wavelength signal in comparison to $\delta \mathrm{T}^{1D}$, we plot in Figure 4.8 the spectral amplitude of $\delta T^{1D}_{400-670}$ and $\delta T^{3D}_{400-670}$ as a function of spherical harmonic degree. These plots are determined

by expanding the maps of Figures 4.6 and 4.7 into spherical harmonics.

δT^{1D} has a 'red' spectrum that is characteristic for seismic tomography. The S660S-S410S traveltime variations, reflecting the shear velocity variations of the TZ, are the largest for the lowest spherical harmonic degrees. In contrast, the spectrum of δT^{3D} exhibits less variations as a function of spherical order.

From the spectra of cap-averaged traveltime maps it is impossible to determine at which spatial wavelengths the ray-theoretical corrections are incorrect. Nevertheless, Figure 4.8 indicates that the 3D corrected traveltime maps of Figure 4.7 includes signals at all spatial wavelengths. The difference in δT^{1D} and δT^{3D} diminishes for increasing spherical order. Beyond about degree 12, the variation of δT^{3D} is as strong as δT^{1D}.

4.5 Discussion and conclusions

In agreement with *Zhao and Chevrot* (2003), we find that ray-theoretical traveltime calculations through long-wavelength shear-velocity models are imprecise. For three versions of S20RTS in which the strength of shear-velocity heterogeneity varies, we find that ray-theoretical calculation of SS traveltimes can differ by several seconds from the traveltimes inferred from spectral-element method (SEM) seismograms (Figure 4.4).

Inaccurate ray-theoretical calculations of traveltimes influence the mapping of the traveltimes of SS precursors (i.e., S400S and S670S) and, hence, the estimates of lateral variations of phase-transition depths.

Our study complements the study from *Zhao and Chevrot* (2003) by calculating traveltime maps of SS-S400S, SS-S670S, and S400S-S670S using stacks of SEM seismograms in geographically distributed caps. Traveltimes are "corrected" for shear-velocity heterogeneity by ray-tracing through tomographic models. This analytical procedure is similar to the procedures commonly applied to waveform data (e.g.

Flanagan and Shearer, 1998; *Gu and Dziewonski*, 2002; *Houser et al.*, 2008). Figure 4.4 indicates that shear-velocity heterogeneity, as imaged tomographically, renders minor SS waveform perturbations at frequencies larger than 60 mHz. Therefore, SS and precursor traveltime differences can be determined accurately by cross-correlation analysis.

Since spectral-element method computations are time-consuming, we limit our analysis to three versions of shear velocity model S20RTS, which vary by the amount of damping applied in the tomographic inversion. The variable strength and dominant spatial scales of shear-velocity heterogeneity in these three models is similar to the variations within the most recently published tomographic models (e.g. *Ritsema et al.*, 2011).

As expected, traveltime anomalies with respect to PREM (Figure 4.6), correlate with the shear-velocity variations in the uppermost mantle (for δT_{400}^{1D} and δT_{670}^{1D}) and transition zone (for $\delta T_{400-670}^{1D}$). The non-zero traveltime variations of δT_{400}^{3D}, δT_{670}^{3D}, and $\delta T_{400-670}^{3D}$ demonstrates that ray-theoretical traveltime calculations of SS, S400S, and S670S are inaccurate.

The stacking of misaligned S400S and S670S waveforms due to the inaccurate traveltime corrections project as traveltime variations that are 20% (for δT_{400}^{3D} and δT_{670}^{3D}) and 50% (for $\delta T_{400-670}^{3D}$) of the uncorrected signal (i.e., $\delta \mathrm{T}^{1D}$). Moreover, maps of $\delta \mathrm{T}^{3D}$ contain both long-wavelength and short-wavelength structures (Figure 4.8). Thus, artifacts in the traveltime maps are not restricted to the short wavelength structure. Spatial variations in $\delta \mathrm{T}^{3D}$ do not clearly relate to the shear-velocity variations in the tomographic model on which they are based and may be misinterpreted as small-scale variations in phase transition depths.

In waveform data, the variation in $\delta T_{400-670}^{1D}$ is about ± 10 s (e.g., *Flanagan and Shearer*, 1998; *Gu and Dziewonski*, 2002). This is an order of magnitude larger than errors in the ray-theoretical corrections for S20RTS (and other tomographic models) of

the upper mantle. Thus, if S20RTS and other recently derived global shear-velocity models are adequate models of the shear-velocity structure in the upper mantle, inaccuracies in the ray-theoretical corrections do not severely influence the resolution of long-wavelength maps of phase transition depth. An error in $\delta T^{3D}_{400-670}$ of 1.0 sec (Figure 4.7) projects as an error in the thickness of the transition zone of about 2 km, which is an order of magnitude smaller than the transition zone thickness variations inferred from waveform data.

As shown in Figure 4.8, the variation in the corrected S400S-S670S traveltime map (i.e., $\delta T^{3D}_{400-670}$) is only smaller than the uncorrected map (i.e., $\delta T^{1D}_{400-670}$) at the longest wavelengths ($<$ spherical degree 8). Naturally, the use of smaller cap radii or, equivalently, stacking and spatial averaging over smaller regions yields maps of traveltime variations with higher-amplitude and more spatial detail. However, as Figure 4.9 shows, the errors due to inaccurate traveltime corrections are also amplified. To study small-scale regions of the mantle with SS precursors, such as hotspot (e.g. *Deuss*, 2007), it is necessary to calculate the contribution of the crust (e.g. *Ritsema et al.*, 2009a) and shear-velocity heterogeneity in the mantle (e.g., *Lawrence and Shearer*, 2008) on traveltimes with finite-frequency approaches.

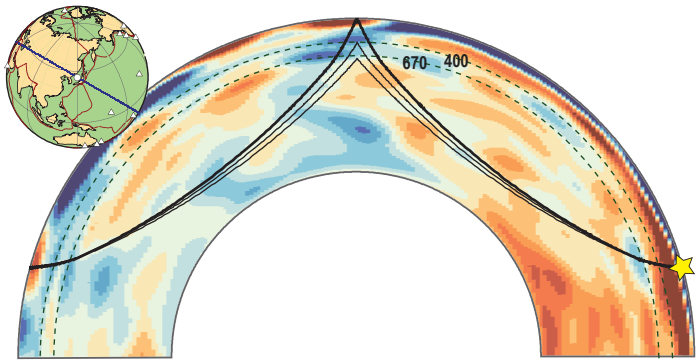

Figure 4.1: Cross-section of model T2 is shown. The background shows the shear-velocity perturbations (low-velocity and high-velocity anomalies in red and blue, respectively) from PREM in a mantle cross-section beneath the western Pacific and eastern Asia (see inserted map) according to model T2. The dashed lines are the 400 and 670 discontinuities.

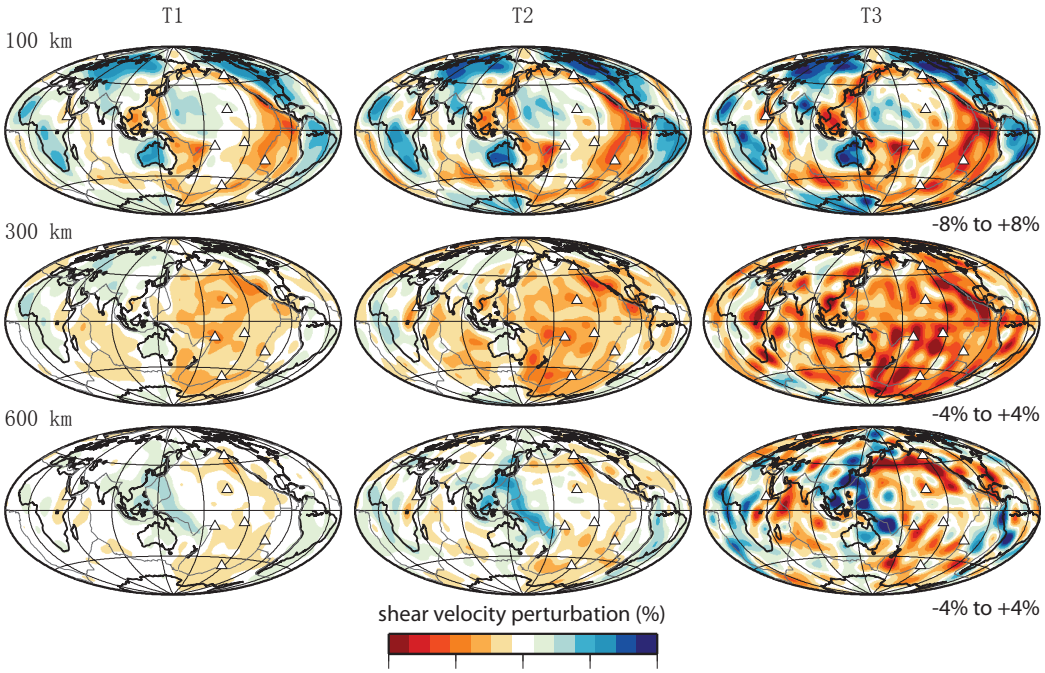

Figure 4.2: Shear-velocity perturbations (from PREM) are shown for S20RTS damped models: T1 (left), T2 (middle), T3 (right). Models are plotted at depths of (top) 100 km, (middle) 300 km, and (bottom) 600 km. Low and high shear-velocity regions are indicated with red and blue colors. The peak-to-peak variation is indicated below the maps. White triangles are hotspot from the catalog of (*Ritsema and Allen*, 2003).

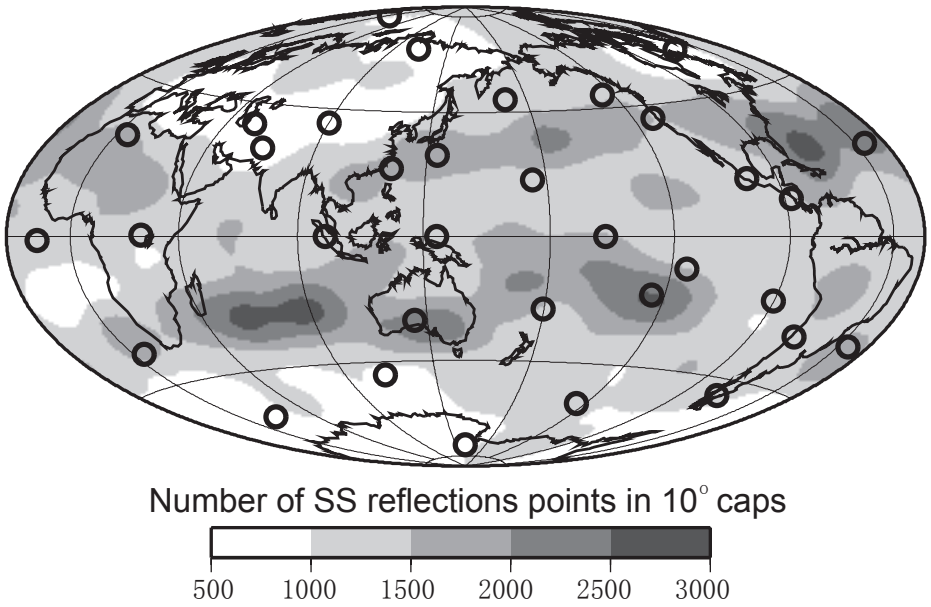

Figure 4.3: Global density of SS bounce points is mapped. Epicenters of 34 earthquakes (circles) superposed on the global density of the SS bounce points. Note that most regions include more than a 1000 geometric SS surface reflection points within caps with a radius of 10°.

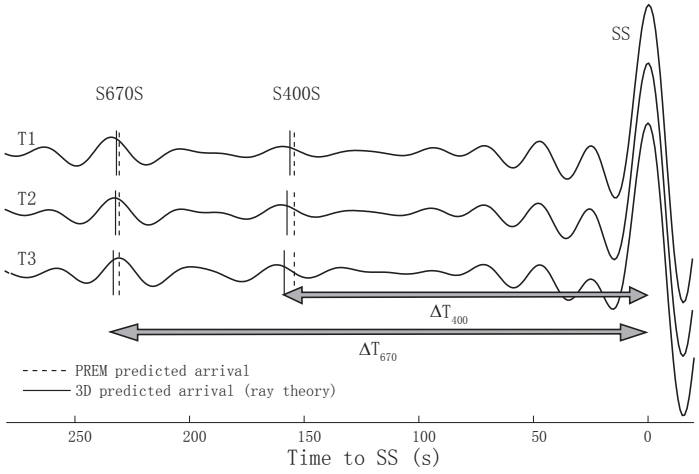

Figure 4.4: Example SEM waveforms of SS, S400S, and S670S are shown. Waveforms of SS, S400S, and S670S for models T1, T2, and T3, computed for an event beneath the North Pacific Ocean and a station in the western Indian Ocean at an epicentral distance of 124°. The waveforms are aligned on the peak amplitude of SS wave whose arrival time is defined to be 0. The SS surface reflection point is beneath the South China Sea (N10°, E115°). The S400S and S670S phases arrive about 160 s and 230 s before SS. Their PREM and 3D predicted arrival times are indicated with dotted and solid vertical lines, respectively.

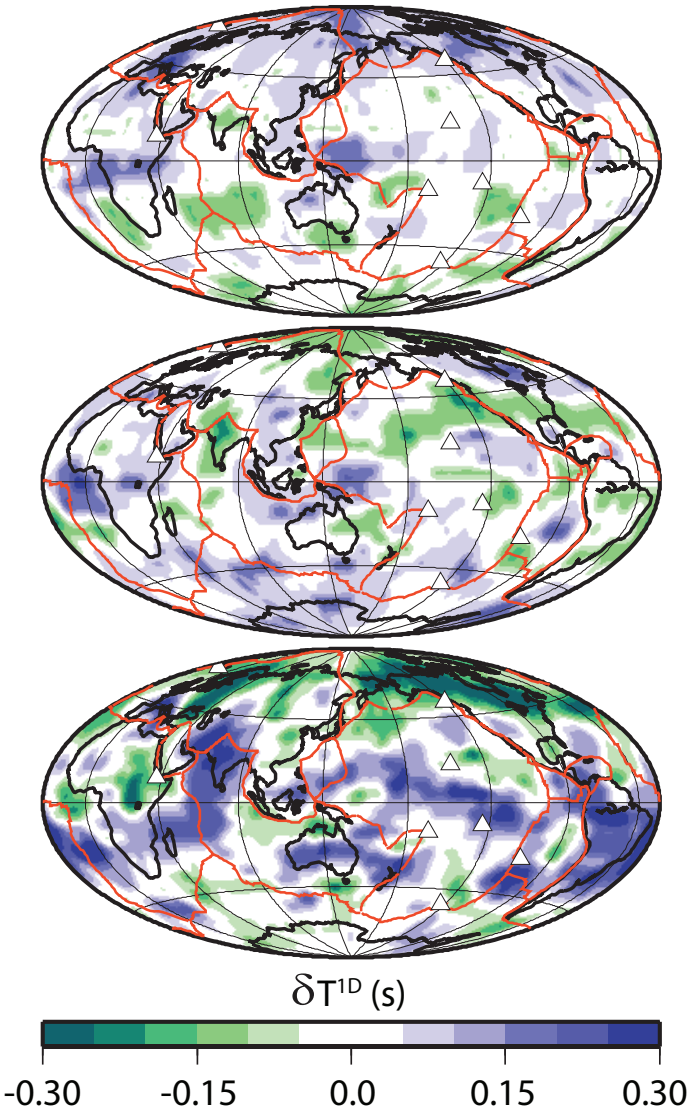

Figure 4.5: Measurement errors are plotted with estimated dT_1D. dT_1D estimated for PREM synthetics (predicted to be 0) for (from top to bottom) SS-S400S, SS-S670S, and S400S-S670S.

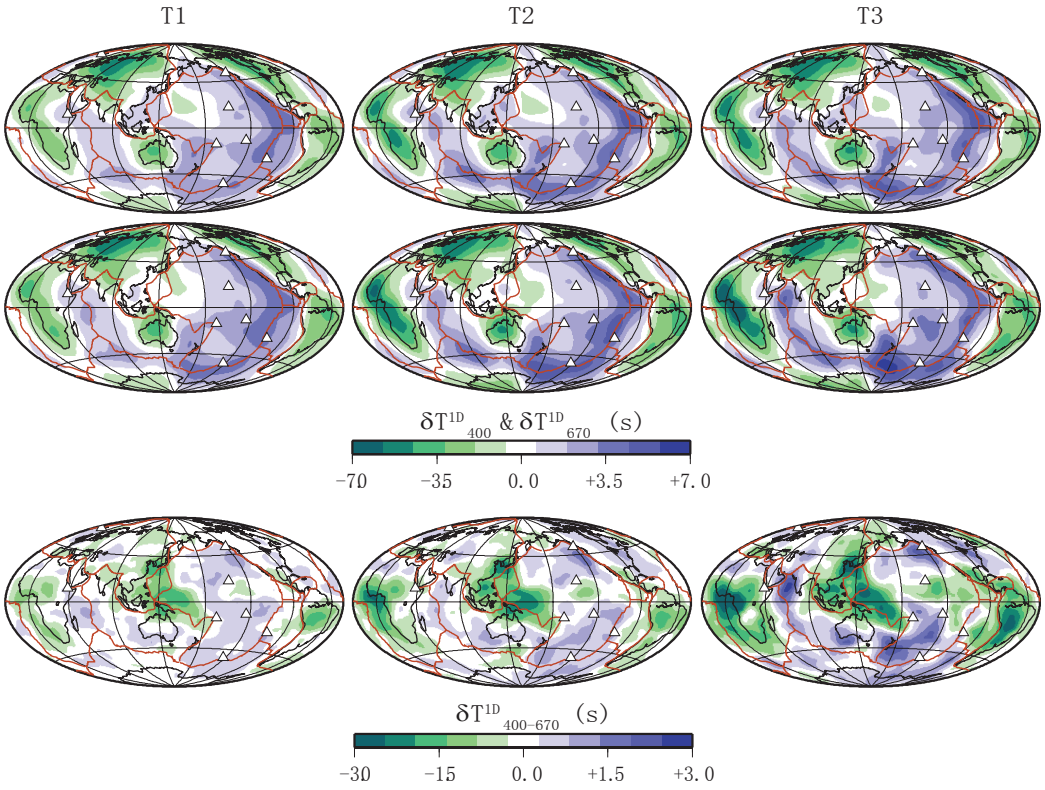

Figure 4.6: dT_1D are estimated for S20RTS damped models. Maps of δT^{1D} for the traveltimes of (from top to bottom) SS-S400S (δT^{1D}_{400}), SS-S670S (δT^{1D}_{670}), and S400S-S670S ($\delta T^{1D}_{400-670}$) for models (left) T1, (middle) T2, and (right) T3. The traveltime variations of δT^{1D}_{400} and δT^{1D}_{670} are two times larger than the variation in $\delta T^{1D}_{400-670}$.

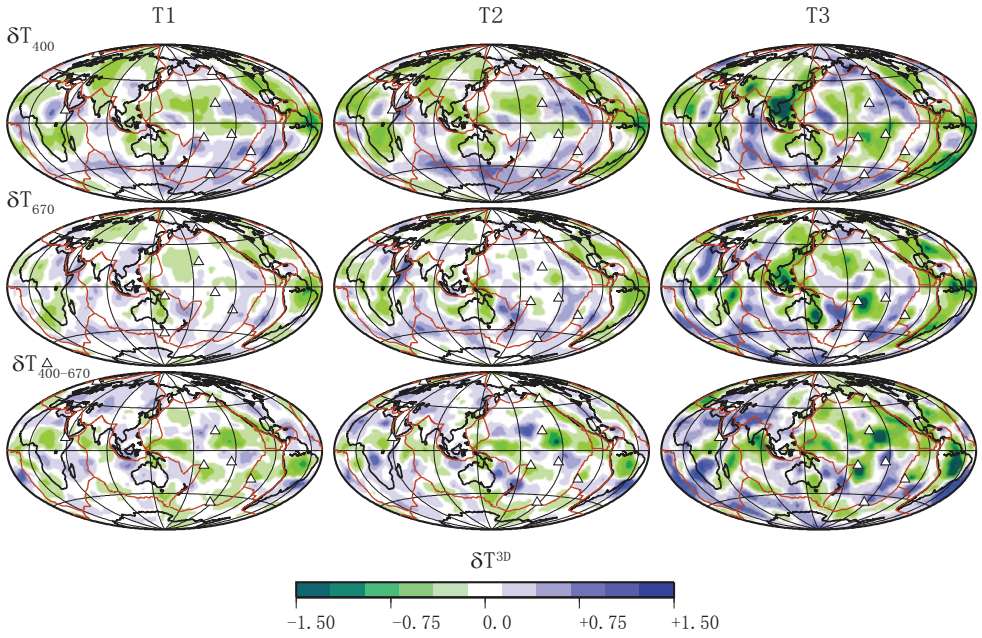

Figure 4.7: dT_3D are estimated for S20RTS damped models. Maps of δT^{3D} for the traveltimes of (from top to bottom) SS-S400S (δT^{3D}_{400}), SS-S670S (δT^{3D}_{670}), and S400S-S670S ($\delta T^{3D}_{400-670}$) for models (left) T1, (middle) T2, and (right) T3.

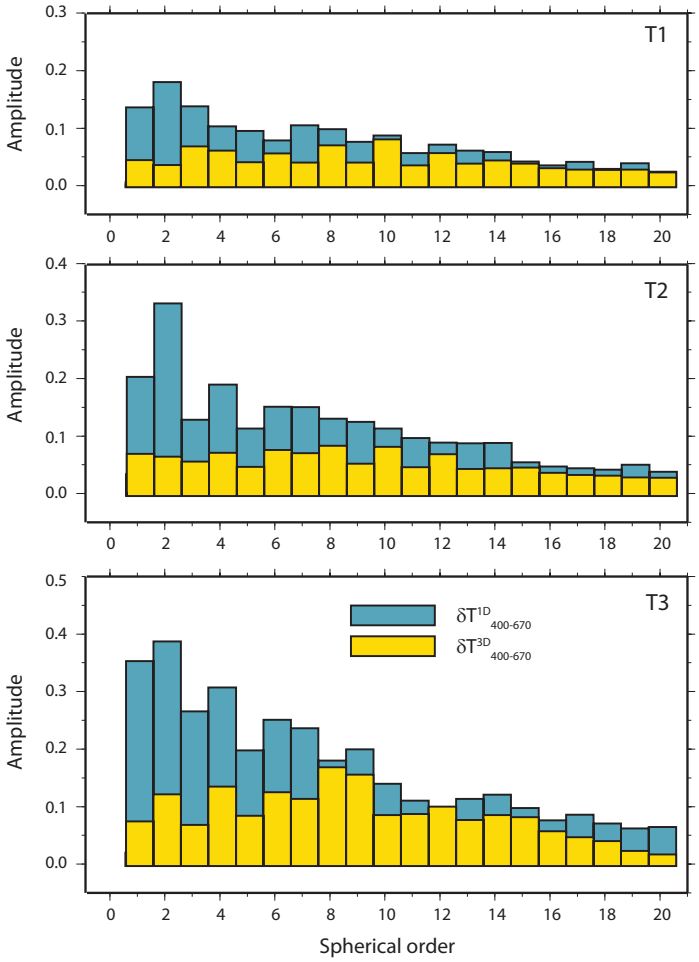

Figure 4.8: Normalized amplitude spectra is calculated of dT_1D and dT_3D. Normalized amplitude spectra as a function of spherical harmonic degree of (blue) $\delta T^{1D}_{400-670}$, and (yellow) $\delta T^{3D}_{400-670}$, for models (top) T1, (middle) T2, and (bottom) T3.

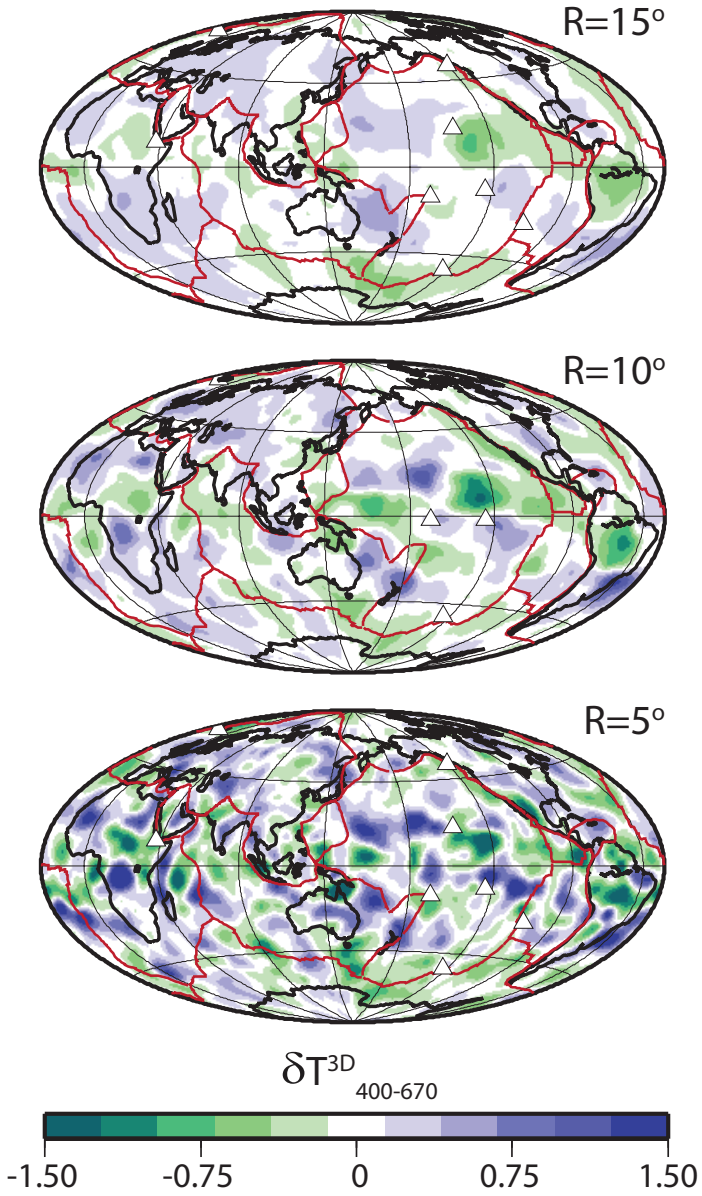

Figure 4.9: dT_3D are estimated for T2 with caps. Maps of $\delta T^{3D}_{400-670}$ for model T2 determined by stacking waveforms within caps with radii of (top) 15°, (middle) 10°, and (bottom) 5°.

CHAPTER V

Modeling spatial distribution of SS/S amplitude ratios

5.1 Abstract

We examine the epicentral distance and spatial variation of a new global data set of 12,000 long-period (>16 s) SS/S amplitude ratios within the epicentral distance range 40–170^o, and model these with 3-D spectral-element method (SEM) simulations. The large-scale pattern of SS/S depends significantly on seismic velocity variations in the deep mantle. SEM predictions of SS/S amplitude variations for global-scale tomographic models of shear velocity show a geographical correlation with tomographic images in the deep mantle. However, they do not correlate well geographically with the observed SS/S, which indicate larger variations when S (or SS) propagates along the margins of the large-scale velocity anomalies. Thus the simulations demonstrate that focusing has a large imprint on body wave amplitude ratios, and that the tomographic models cannot reproduce the observed spatial patterns, especially near margins of two LLSVPs.

5.2 Introduction

The amplitude is a basic attribute of a seismic wave, yet amplitude variations are more complex than traveltime anomalies. Amplitudes depend on near source and receiver complexity and wave excitation by earthquakes. More importantly in the context of this thesis, they depend on heterogeneous elastic structure which causes wave focusing (*Woodhouse and Wong*, 1986; *Wang and Dahlen*, 1995) and on Earth's anelastic structure (e.g., *Dalton and Ekström*, 2006). Although anelastic structure of the mantle has been estimated from surface wave (e.g., *Romanowicz*, 1995; *Selby and Woodhouse*, 2000; *Dalton and Ekström*, 2006; *Dalton et al.*, 2008) and body wave (e.g., *Bhattacharyya et al.*, 1996; *Reid et al.*, 2001; *Warren and Shearer*, 2002) amplitudes, wave focusing may overwhelm the anelastic effects. It is therefore be challenging to separate elastic and anelastic contributions.

Body-wave traveltime differences such as SS-S (e.g., *Woodward and Masters*, 1991) and S-SKS (e.g., *Kuo et al.*, 2000) are extremely useful to constrain seismic velocity variations in the mantle. Here we focus on body-wave amplitude ratios of SS and S waves. *Ritsema et al.* (2002) demonstrated that coherent patterns of the SS/S amplitude ratio can be determined from high-quality long-period waveform data. We expand on this study with a new collection of SS/S amplitudes and a new set of simulations to determine whether it can be explained by reasonable models of seismic velocity and attenuation. Our aim is to investigate whether the wave amplitude may be a useful complementary data type in tomography. Ultimately, body-wave amplitudes and full waveforms may prove useful in tomographic inversions.

5.3 Measurements

5.3.1 Data

The amplitudes of S and SS amplitudes can be measured over a broad teleseismic distance range (40–160^o) even if S diffracts. They provide good lateral, vertical sampling of the mantle. Our new global data set includes more than 12,000 SS/S amplitude ratio measurements. The SS/S amplitude ratios is not severely influenced by errors in uncertain earthquake source parameters (e.g., epicenter, mechanism, and seismic moment) and heterogeneous structure near the source and receiver.

The S and SS phases have different paths in the mantle, and turn at different depths. SS is an underside reflection off Earth's surface halfway between an earthquake and seismic station, as shown in Figure 5.1. At a distance of 60^o, SS turns just below the transition zone. SS turns at about 2700 km depth at 140^o. The turning depth of S wave is $\sim$1200 km at 60^o and S begins to diffract along the core-mantle boundary at distances larger 100^o. S and SS have high amplitudes and are well-isolated phases and can thus be easily measured using seismograms for a diverse set earthquake-station pairs that render a global distribution of SS reflection points. The ray paths of P and PP are propagating along similar paths with S and SS, respectively, except with steeper taking-off angles.

Using broadband waveform data collected from the global IRIS and GEOSCOPE networks, permanent regional networks (e.g. CNSN, USNSN, GRSN), and PASSCAL deployments (1980–2005), we measure SS/S and PP/P amplitude ratios with respect to the Preliminary Reference Earth Model (PREM) (*Dziewonski and Anderson*, 1981). We make these measurements by cross-correlating low-pass filtered (T $>$ 16 s) observed and synthetic waveforms following *Ritsema and van Heijst* (2002). The synthetics are computed by normal-mode summation using the PREM's velocity and Q structures and Harvard CMT source parameters.

To visualize the global pattern of SS/S amplitude ratios, we plot values of the SS/S amplitude ratios at the SS reflection points (Figure 5.2). Since measurement scatter is large, smoothing is applied by cap averaging to bring out the coherent large scale variation. Here, the average value of SS/S is determined for all measurements with SS reflection points in the same circular cap with a radius of 5 or 10^o (e.g. *Flanagan and Shearer*, 1998). Most SS reflection are points located in the central Pacific and Eurasia because most seismic stations are located in Europe and North America. The Indian Ocean, the Atlantic Ocean, North America, Australia, and Europe are also well sampled. SS bounce point density is low in South America and Africa, because most of sources and stations are located in the northern hemisphere.

5.3.2 Measurement criteria

The waveshape of a long-period (T>16 s) body wave is not severely complicated by the earthquake rupture process, complex crustal reverberations and microseismic noise. It is therefore possible to measure body-wave traveltime and amplitudes to process a large volume of data automatically, without bias, and with the same accuracy. We apply several quality-control criteria to identify unreliable measurements following *Ritsema and van Heijst* (2002). Seismograms with high noise levels before the first-arrival and high-amplitude coda are discarded. Phases that arrive within 40 s are excluded for measurements. Two quantities, F_1 and F_2, defines the similarity between recorded ($d(t)$) and synthetic ($s(t)$) waveforms. They are the least-squares misfit between recorded and synthetic waveforms within a a 40-s long cross-correlation window w centered about the predicted arrival time:

$$F_1 = \frac{\int_w [d(t) - s(\tau_m - t)]^2 dt}{\int_w d(t)^2 dt}. \tag{5.1}$$

Here, τ_m is the time-shift of the synthetic (i.e. the traveltime delay) at which the cross-correlation function has a maximum. The second quantity is defined as:

$$F_2 = \frac{min(A_1, A_2))}{max(A_1, A_2))}. \tag{5.2}$$

where A_1 and A_2 are amplitude factors that minimize, respectively, using

$$\int_w [d(t) - A_1 s(\tau_m - t)]^2 dt \tag{5.3}$$

and

$$\int_w [A_2^{-1} d(t) - s(\tau_m - t)]^2 dt. \tag{5.4}$$

A_1 and A_2 are amplitudes anomalies of the seismic phases within window w. Similar values of A_1 and A_2 (and hence F_2=1) indicate identical wave shapes, while dissimilar wave shapes between $s(\tau_m - t)$ and $d(t)$ lead to A_1 and A_2 differences and a value of F_2. We require that F_1 and F_2 are larger than 0.7 Figure 5.3 shows an example of our criteria to accept or reject S and SS measurements. Measurements of traveltime and amplitude are acceptable if there is a good match between the observed and synthetic waveforms match well in the entire cross-correlation window. Different processing parameters (e.g., different minimum values of 0.6, 0.8, 0.9 assigned to F_1 and F_2) are used to analyze the reliability of the measurements. We find only minimal differences in our set of measurements as long as F_1 and F_2 are larger than 0.7.

We have measured a total of about 220,000 P-wave traveltimes and 167,000 S-wave traveltimes for about 4,000 earthquakes (1980–2005) listed in the Harvard-CMT catalog with a body-wave magnitude larger than 5.9.

After selecting high-quality seismograms for single phases, we identify seismograms on which we can measure the amplitudes of P and PP (i.e.,A_1^P, A_2^P, A_1^{PP}, A_2^{PP}) on vertical component recordings and S and SS (i.e., A_1^S, A_2^S, A_1^{SS}, A_2^{SS}) on

transverse component recordings. We define

$$A_1^{SS/S} = \frac{min(A_1^{SS}, A_2^{SS})}{max(A_1^S, A_2^S)} \tag{5.5}$$

and

$$A_2^{SS/S} = \frac{max(A_1^{SS}, A_2^{SS})}{min(A_1^S, A_2^S)} \tag{5.6}$$

as minimum and maximum estimates of the SS/S amplitude ratio, respectively. The best estimate of SS/S and its uncertainty are calculated by

$$SS/S = \frac{A_1^{SS/S} + A_2^{SS/S}}{2} \pm \frac{A_1^{SS/S} - A_2^{SS/S}}{2}. \tag{5.7}$$

The threshold for accepting the measurements of SS/S is

$$\frac{\left|A_1^{SS/S} + A_2^{SS/S}\right|}{A_1^{SS/S} - A_2^{SS/S}} < 0.1. \tag{5.8}$$

We define the amplitude variations of SS/S amplitude ratios by

$$\delta A_{SS/S} = \log_{10}(\frac{A_1^{SS/S} + A_2^{SS/S}}{2}), \tag{5.9}$$

and PP/P by

$$\delta A_{PP/P} = \log_{10}(\frac{A_1^{PP/P} + A_2^{PP/P}}{2}). \tag{5.10}$$

Values of δA equals to 0 imply that the measurements are identical to PREM-predicted values.

This corresponds to data with a least-squares waveform fit between $d(t)$ and $s(\tau_m - t)$, after the time shift τ_m has been applied, of at least 80% and values of F_1 and F_2 are higher than 0.7. The signal-to-noise ratios are larger than 1.7, minimal traveltime uncertainties are smaller than 10 s, and amplitude anomalies are smaller than 3.0.

Our data set includes 12,000 SS/S measurements at epicentral distances larger than 45^o. The same measurements procedure and selection criteria are applied to vertical component waveform data to obtain 13,700 PP/P amplitude ratio measurements.

5.3.3 SS/S and PP/P amplitudes distance profiles

Figure 5.4(a)(b) shows PP/P and SS/S as a function of epicentral distance. Average values of SS/S and PP/P amplitude ratios are determined for 5^o wide bins. The scatter of both SS/S and PP/P is large: PP/P varies between 0.4 and 2.5, and SS/S varies between 0.2 and 6.3. However, the amplitude ratios have a clear trend with distance, especially for SS/S. SS/S increases between 50^o and 60^o, remains higher than 1 until 110^o, and decreases sharply at larger distances. In comparison, PP/P amplitude ratios slightly decreases between 40^o–160^o.

The distance dependence of SS/S amplitude ratios might indicate the existence of some 1D structure. It decreasing at $\Delta > 110^o$ that persists in different subsets of measurements. Anomalous velocity gradients in D" may be responsible for the decrease in SS/S at $\Delta > 110^o$, Since for these distances S propagates as a diffracted wave along the core-mantle boundary (Figure 5.1). Anomalous vertical velocity gradients in D" may affect S amplitudes (e.g., *Thorne and Garnero*, 2004). For example, *Ritsema et al.* (1997) demonstrate that the strong negative gradient in D" beneath the Pacific region amplifies the amplitude of S. Thus, the observed decrease of the SS/S amplitude ratio may be related to an increase in the S amplitude due to anomalous gradients at the core-mantle boundary.

However, Figure 5.7 demonstrates that the SS/S reduction at $\Delta > 110^o$ is a global characteristic seen for S paths that propagate through regions with both relatively high and low shear velocities. Over 80% of the S paths are from four earthquake source regions: the Fiji region (FJ), the South America subduction region (SA), the Japan subduction region (JP), and the Indonesia region (IN). SS/S measurements

from these regions show similar trends. The Fiji region, associated with seismograms in Europe, yield D" sampling below Eurasia. *Gaherty and Lay* (1992) have previously resolved a high shear velocity gradient at the base of the mantle in this region. The Indonesia events are primarily recorded at North American stations with S paths sampling D" beneath the northern circum-Pacific region. This is also region where shear velocities are relatively high (e.g., *Ritsema et al.*, 1997). All four subsets have negative amplitude variations for $\Delta > 130^o$ even though S samples primarily high velocity D" regions, which are expected to reduce S amplitudes. Therefore, we believe that our data are not biased by preferential sampling of D" with negative velocity gradients. We suspect that attenuation in the mantle is the cause of this trend. For now, we focus on the variability of SS/S and PP/P and analyze these data after the epicentral distance trend has been removed.

5.3.4 SS/S and PP/P amplitudes global variations

To visualize the spatial distribution of SS/S and PP/P amplitude ratios, we plot their values at the bounce point of the reflected waves (SS and PP). Figure 5.5 shows the PP/P and SS/S amplitude ratios before and after the distance trend has been removed. If the trend is taken out, the SS/S variation is slightly reduced. PP/P amplitude variations with or without the distance corrections are similar, since PP/P do not vary strongly with epicentral distance.

The global variation of PP/P clearly exhibits a oceanic/continental distribution. The largest values correspond to continental PP reflection points, and the smallest PP/P have PP reflection points in the oceans. This observation was also made by *Ritsema et al.* (2002) who suggested that the variable crustal thickness at the PP/P reflection points is responsible for a variable PP reflection coefficient.

In contrast, the SS/S amplitude ratios do not clearly correlate with surface geology. This suggest that SS/S is not predominantly affected by seismic structure in the

uppermost mantle and crust. SS/S has minima in the central and southern Pacific, along the Atlantic ridge, and northwestern Europe. and maxima beneath northern Africa, northern North America and central South America. However, a clear oceanic-continental correlation in SS/S is missing. This suggest that seismic structure in the entire mantle affects SS/S. There is a weak degree-2 signal in SS/S, with negative amplitude values beneath the Pacific and Africa region, suggesting that LLSVPs in the deep mantle structure influence the SS/S amplitude ratios.

To further explore the influence of the upper mantle (<1000 km), mid mantle (>1000 km), and lower mantle (>2000 km) we divide the data sets into three groups. Figure 5.6 shows (1) SS/S for epicentral distances smaller than 90^o, (2) larger than 90^o, and (3) larger than 110^o. If $\Delta < 90^o$, S turns within a wide depths within the lower mantle but SS turns shallower than 1000 km. If $\Delta > 90^o$, S propagate near the base of the mantle. If $\Delta > 110^o$, S has diffracted over one thousand of kilometers along the core-mantle boundary. Because SS/S for group (1) sample the entire mantle column, its spatial pattern is values of data collected in the model with distances ¡90^o are averaged over a wide depth ranges, the spatial patterns is complex. SS/S of groups (2) and (3) include S wave data with D" sampling. They exhibit large-scale patterns of negative $\delta A_{SS/S}$ values (see Equation 5.9) beneath the Pacific, Africa and the Atlantic, and they are strongest for group (3). This suggest that the LLSVPs of the lowermost mantle affect SS/S which will be discussed later.

Because of the dominate influence by the crust, it is hard to quantify the mantle affects for PP/P. We focus only on SS/S from hereon.

5.4 Tomographic Model Predictions

In order to investigate whether the amplitude ratios are predicted by shear velocity variation as imaged in tomographic models, we simulate SS/S amplitude ratios by applying Equation 5.7 to synthetic transverse component seismograms. These syn-

thetics are computed using the Spectral-Element Method (SEM) (*Komatitsch and Tromp*, 2002c,d) for crustal model CRUST2.0 (*Bassin et al.*, 2000), model ETOPO5 of ocean bathymetry and topography (NOAA,1988), and 3-D models of S and P wave velocity heterogeneity in the mantle. We focus on a variety of tomographic models (S20RTS (*Ritsema et al.*, 1999), S40RTS (*Ritsema et al.*, 2010) and S362ani (*Kustowski et al.*, 2008)) which represent isotropic (S20RTS and S40RTS) and anisotropic (S362ani) shear velocity perturbations from transverse isotropic PREM (*Dziewonski and Anderson*, 1981). The waveforms are computed for periods longer than 20 s similar to the frequencies used to process the data.

Since the SEM simulations are time consuming, we limit ourselves to calculating 400,000 synthetic seismograms for 34 worldwide earthquakes with synthetic seismic station distributions of $2^o \times 2^o$ cell globally. The distribution of SS reflection points (Figure 5.8) have dense global coverage. Regions such as central Eurasia and North America have the densest coverage. The large number of synthetic seismograms ensuring that the gross statistic of data coverage is reproduced.

The calculated global variations of SS/S amplitude ratios for models S20RTS, S40RTS and S362ani are shown in Figure 5.9. The gross patterns and amplitudes of SS/S predicted by model S20RTS and S40RTS are very similar, and SS/S computed for model S362ani is only slightly different, especially beneath the Pacific. SS/S is mostly positive in southern Asia and North America, and negative in the Pacific, Africa and along the Southeast Indian Ridge. Although one can identify a few similarities, a clear correlation between the theoretical and observed SS/S values and the predicted values for the tomographic models is missing.

However, a degree-2 pattern is present in the simulations of SS for larger distances. In Figure 5.10, we analyze the simulated SS/S for model S20RTS in the same manner as Figure 5.6: SS is plotted for distances (1) $< 90^o$ (2) $> 90^o$ (3) $< 110^o$ and smoothed using cap averaging. As in the data we observe negative values for SS/S for SS/S in

the Pacific and Africa, that is strongest for group (3). In detail the pattern of SS/S resembles the shape of the LLSVP at the core-mantle boundary. The simulations for distances smaller than 90^o (i.e., group (1)), on the other hand, indicate an influences of shallow structure with strong negative anomalies south of Australia, the Afar region and Europe, and positive values within the Pacific west of the East Pacific Rise.

The match between the observed and simulated SS/S amplitude ratios is not perfect. For the largest distance the influence of the LLSVP is clear. However, the observed SS/S amplitudes are lowest near the edges of the LLSVPs, which suggest that the lateral gradients affect SS/S amplitudes. For instance, SS/S in the Fiji region has show a strong negative value of amplitude measurements, which might indicate the sharp southwestern margin of the Pacific LLSVP. The central "hole" in the middle of Pacific LLSVP may indicate that shear velocity gradients are smooth within these anomalies.

5.5 Discussion

SS/S amplitude variations point to the significant effects of velocity gradients in the mantle on wave propagation. The SEM-predicted SS/S amplitude ratio underestimates the actual elastic focusing effects, because seismic amplitudes are determined by gradients and second derivatives of the velocity model, which are reduced by damping in the tomographic inversion.

Using the spectral-element method (SEM) seismograms we demonstrate that seismic wave focusing imparts long-period body-wave amplitude variations. This is consistent with previous inferences (e.g., *Ritsema et al.*, 2002; *Tibuleac et al.*, 2003). The simulated SS/S amplitude ratios imitate the tomographic predictions in the deep mantle. However, the low correlation between the observed and computed amplitude ratios indicates that long wavelength shear velocity structure in the mantle does not fully explain the observed amplitude anomalies and that wave attenuation may also

play a role.

The varies versions of tomographic models shows that the strength of the shear velocity anomalies do not play a major role in the observed mismatches. The comparisons between S20RTS (and S40RTS) and S362ani confirms that the expected variation of SS/S is the same for a variety of 3-D models. Our findings suggest that the current tomographic images lack sufficiently strong structure (especially sharp velocity gradients) because of regularization and only including traveltimes.

5.6 Conclusion

New global measurements of SS/S amplitude ratios with wide distance ranges (40–160^o) are made. Negative values of SS/S at the largest distances are not differentiated regionally and are most due to attenuation in the mantle.

After the epicentral distance trend has been removed, we quantify whether various 3-D mantle can explain the SS/S variations. We have used three tomographic models with different parameterizations. While spatial variations from simulation for each of the 3-D models are similar, none of them explain the observed lateral variations well. A degree-2 pattern is present in the 3-D simulations of amplitude variations, which resembles the LLSVPs at the CMB. In contrast, the observed amplitude exhibit extreme values at the edges of the large-scale anomalies, determined possibly by sharp lateral velocity gradients. We therefore conclude tomographic models poorly map sharp lateral gradients that cause strong focusing of seismic waves.

To summarize, SS/S amplitude ratios are valuable for refining shear-velocity models of the mantle by containing additional information of velocity gradients. Structures caused by sharp velocity changes must be refined to constrain the effects of focusing and defocusing in the (deep) mantle using body-wave amplitudes.

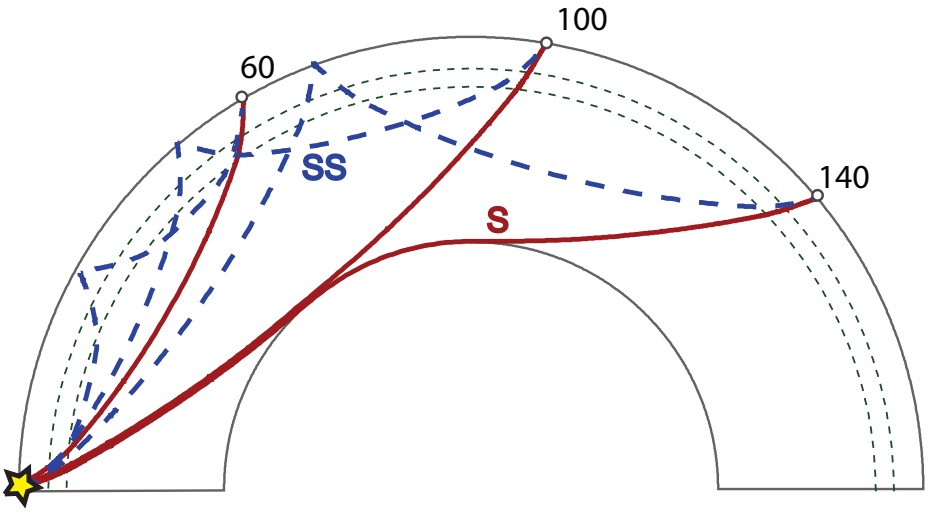

Figure 5.1: Raypaths of S (solid) and SS (dash) waves are shown for an epicentral distance of 60^o, 100^o, 140^o. It indicates the turning depths information of both SS and S waves.

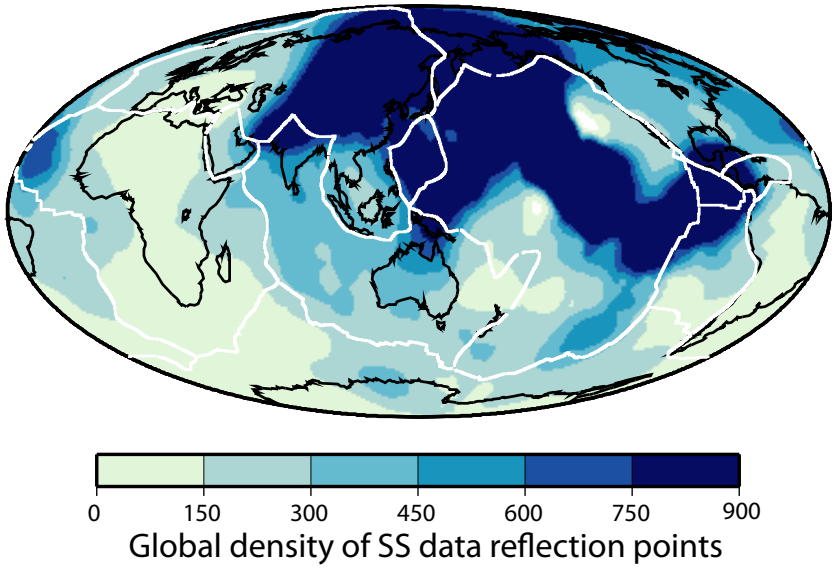

Figure 5.2: The global density of the SS bounce points is plotted in a map view. Note the uneven geometric distribution of SS surface reflection points plotted with radius 5^o caps. The darker the shading, the higher the density of bounce points.

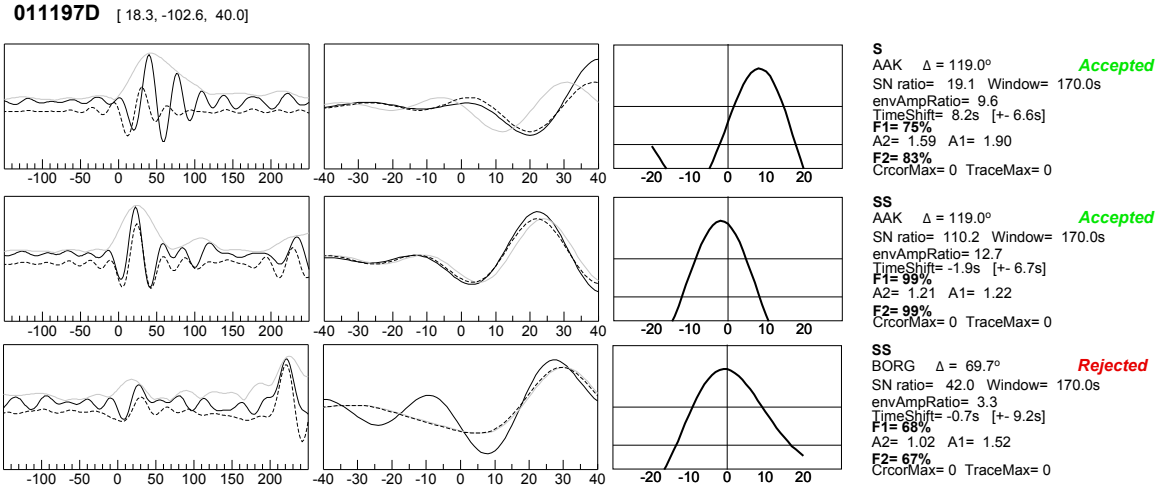

Figure 5.3: Examples of S, SS waves measurements for event 011197D recorded at global stations AAK and BORG. The left panel compares seismograms (dark line) and PREM synthetics (grey line) about the predicted PP-wave arrival for a 400 s long window, while the middle panel shows the PREM fit as well as the best-fitting synthetic (dashed line) after a time shift has been applied. The right column shows the cross-correlation function. The variables provided on the right are the criteria used to consider whether a measurement is reliable or not. The S and SS waves for are regarded as acceptable because F_1 and F_2 are higher than 0.7, the S and SS wave is simple and well above noise level, and the cross-correlation function does not have a secondary maximum. The SS measurement on BORG is rejected because both F_1 and F_2 are lower than 0.7 due to the waveform mismatch at the onset of SS.

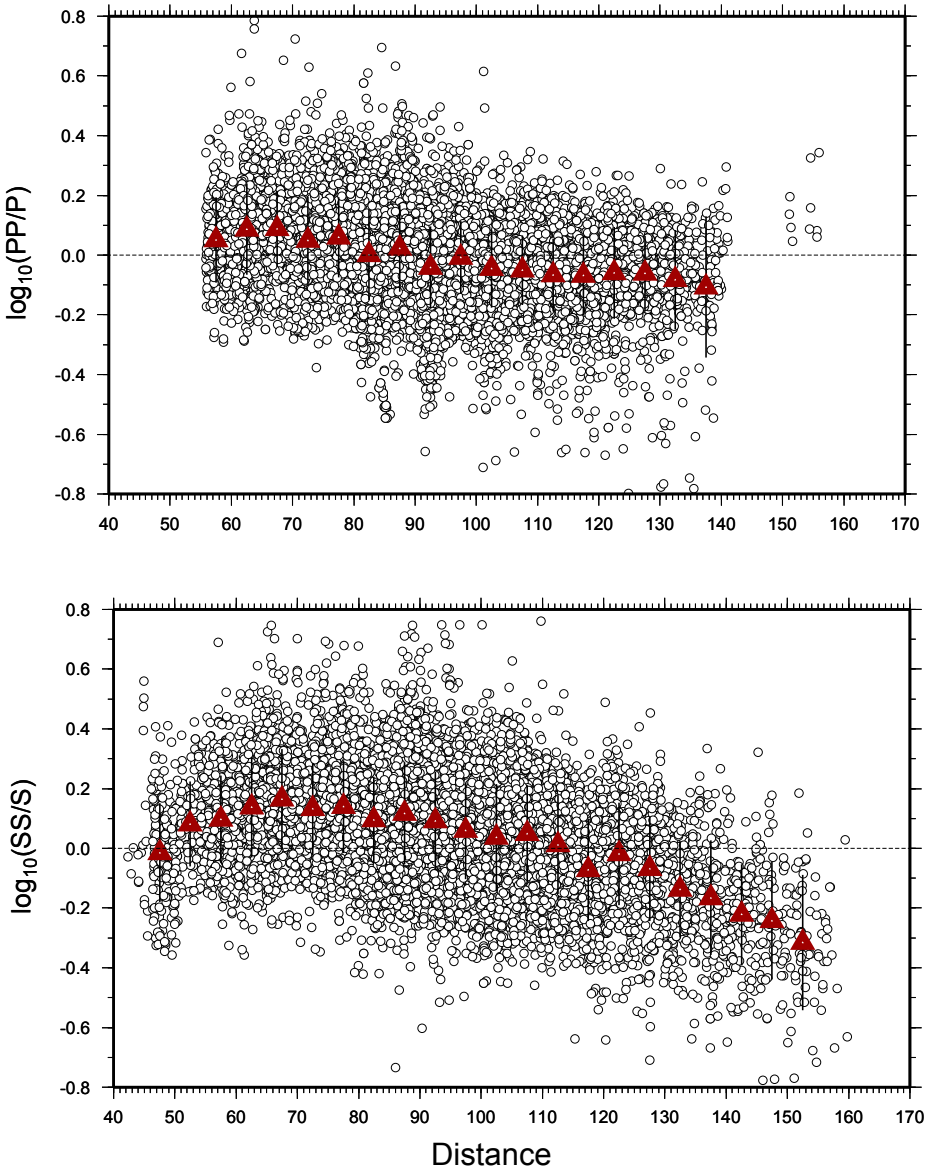

Figure 5.4: The global measurements (black dots) are plotted along epicentral distances (40^o – 170^o) of (a) PP/P amplitude ratios and (b) SS/S amplitude ratios. The averaged values (red triangles) are plotted within bins of 5^o each and one standard deviation.

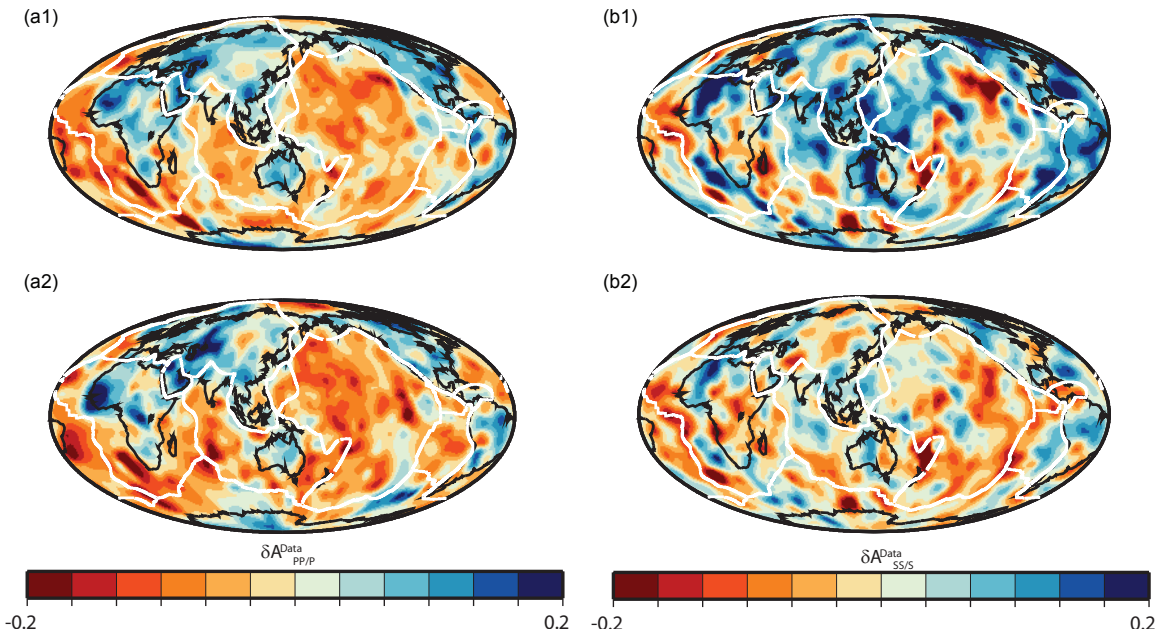

Figure 5.5: Global variation of PP/P (a1) and SS/S (b1) measurements are plotted and the same data after they have been corrected for the epicentral distance variation (a2, b2) smoothed out with cap size of 5^o.

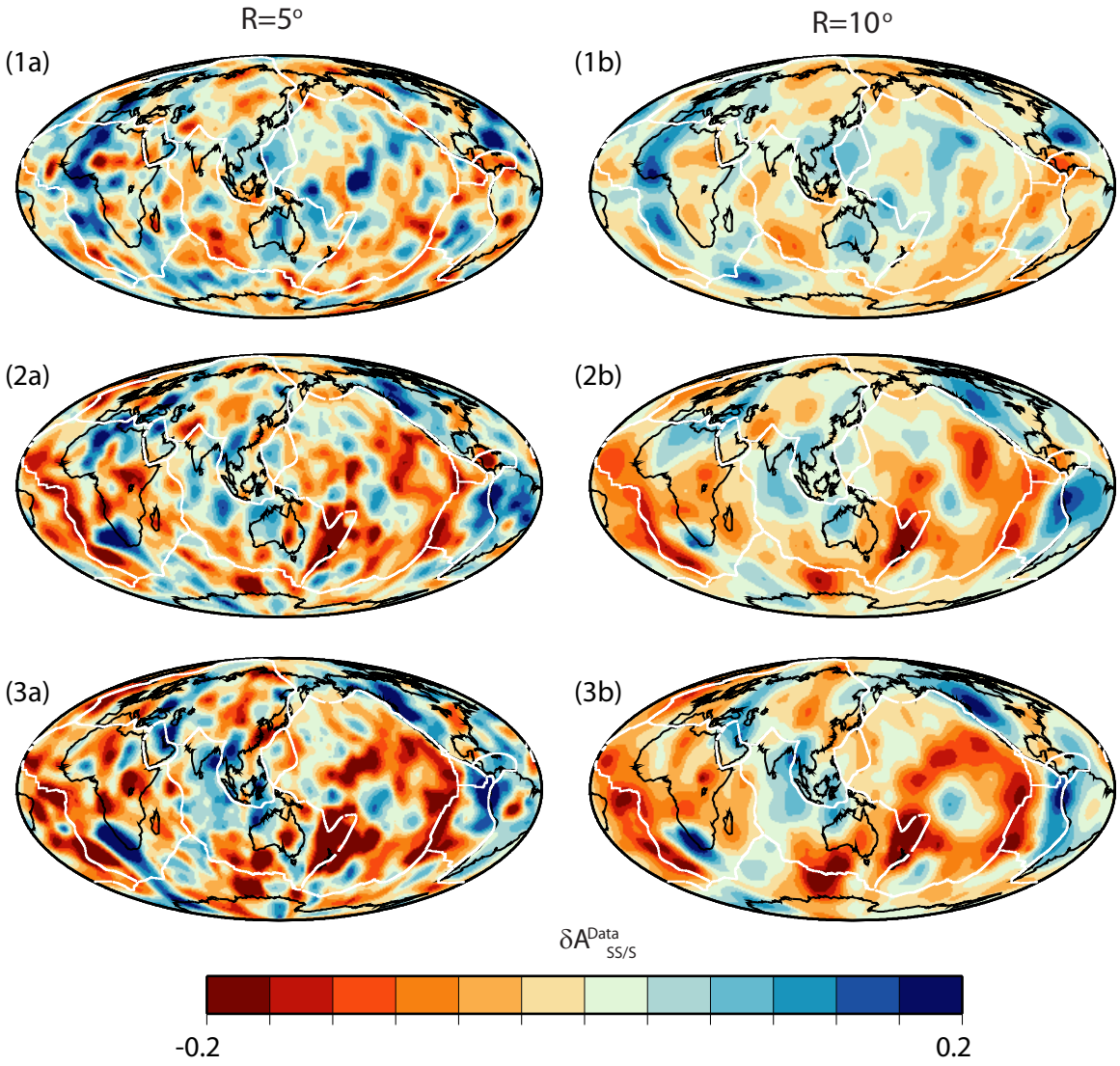

Figure 5.6: Distance dependence of SS/S amplitudes global variations are shown with epicentral distances (1)<90^o, (2)>90^o and (3)>110^o smoothed out with cap sizes 5^o(1st column) and 10^o(2nd column).

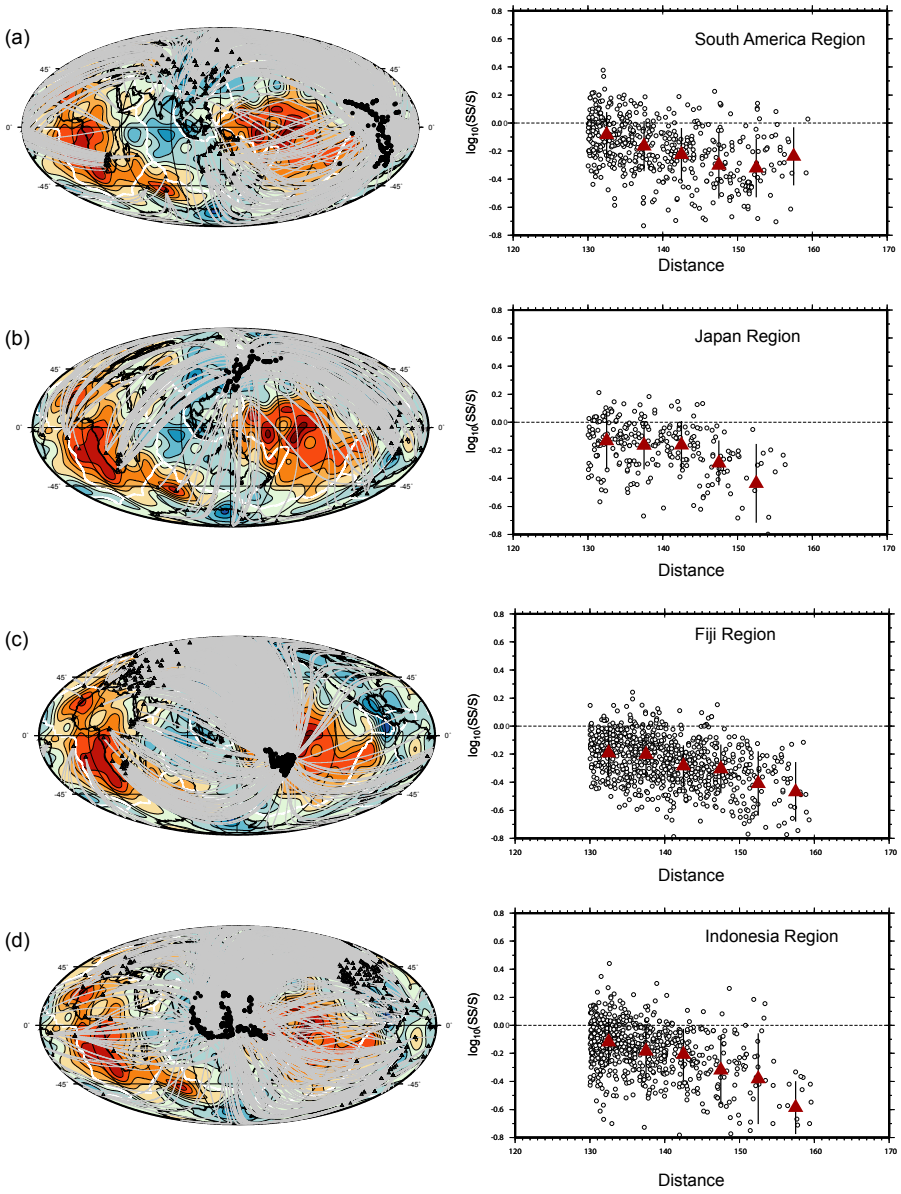

Figure 5.7: Regional variations of SS/S amplitude ratios with epicentral distance > 130^o are plotted with sources divided into (a)South America Region (b) Japan Region (c) Fiji Region (d) Indonesia Region. The averaged values (red triangles) are plotted within bins of 5^o each and one standard deviation.

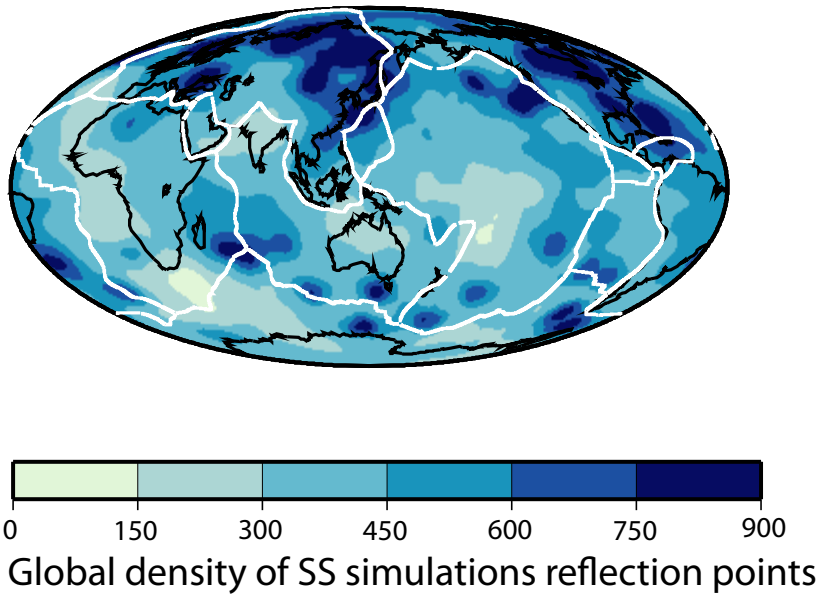

Figure 5.8: The global density of the SS bounce points from 3D synthetics are plotted in a map view. Note the uneven geometric distribution of SS surface reflection points plotted with radius 5^o caps.

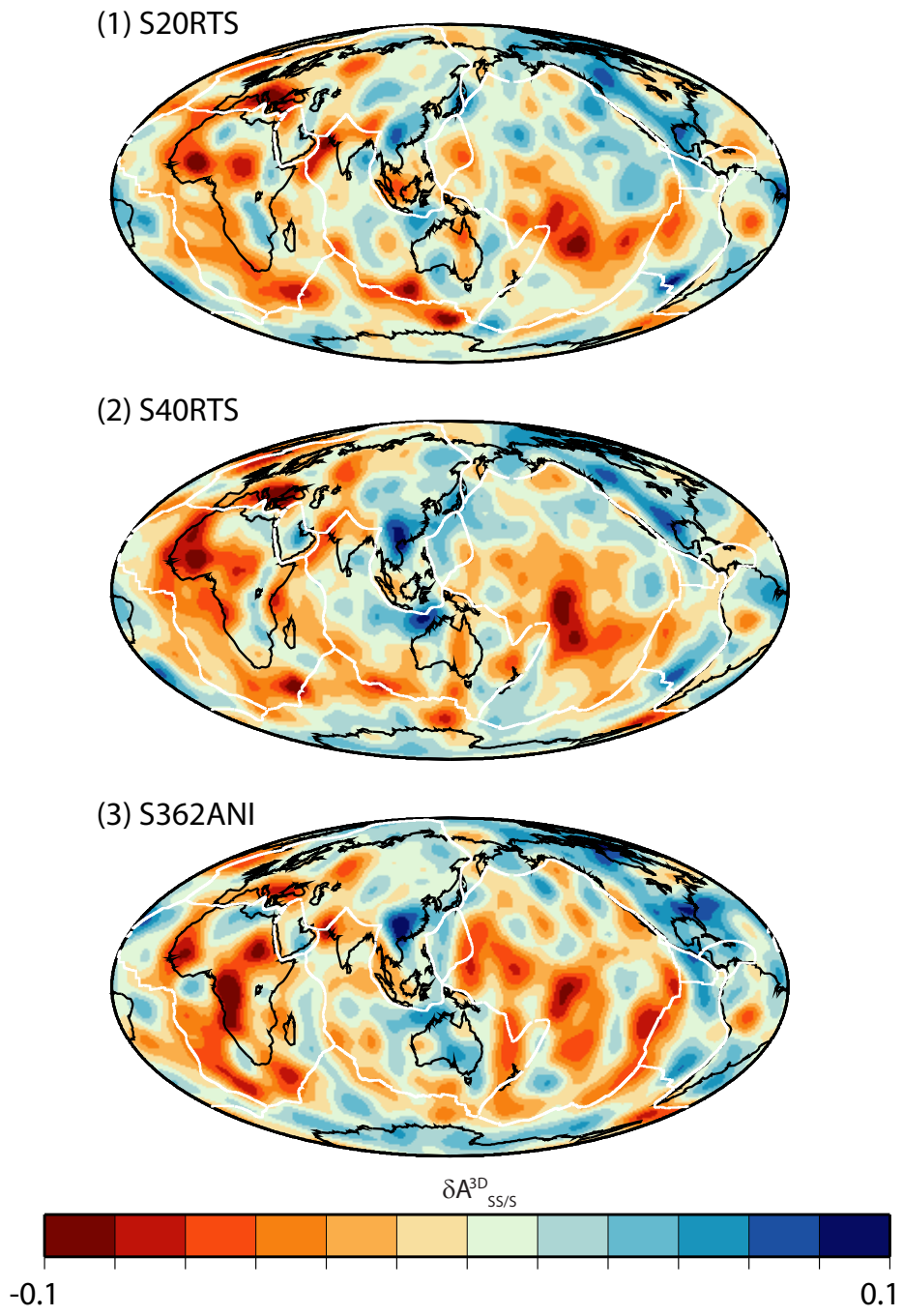

Figure 5.9: Calculated values of SS/S amplitude ratios are plotted for models S20RTS (*Ritsema et al.*, 1999), S40RTS (*Ritsema et al.*, 2010), and S362ani (*Kustowski et al.*, 2008) averaged by cap size 5^o.

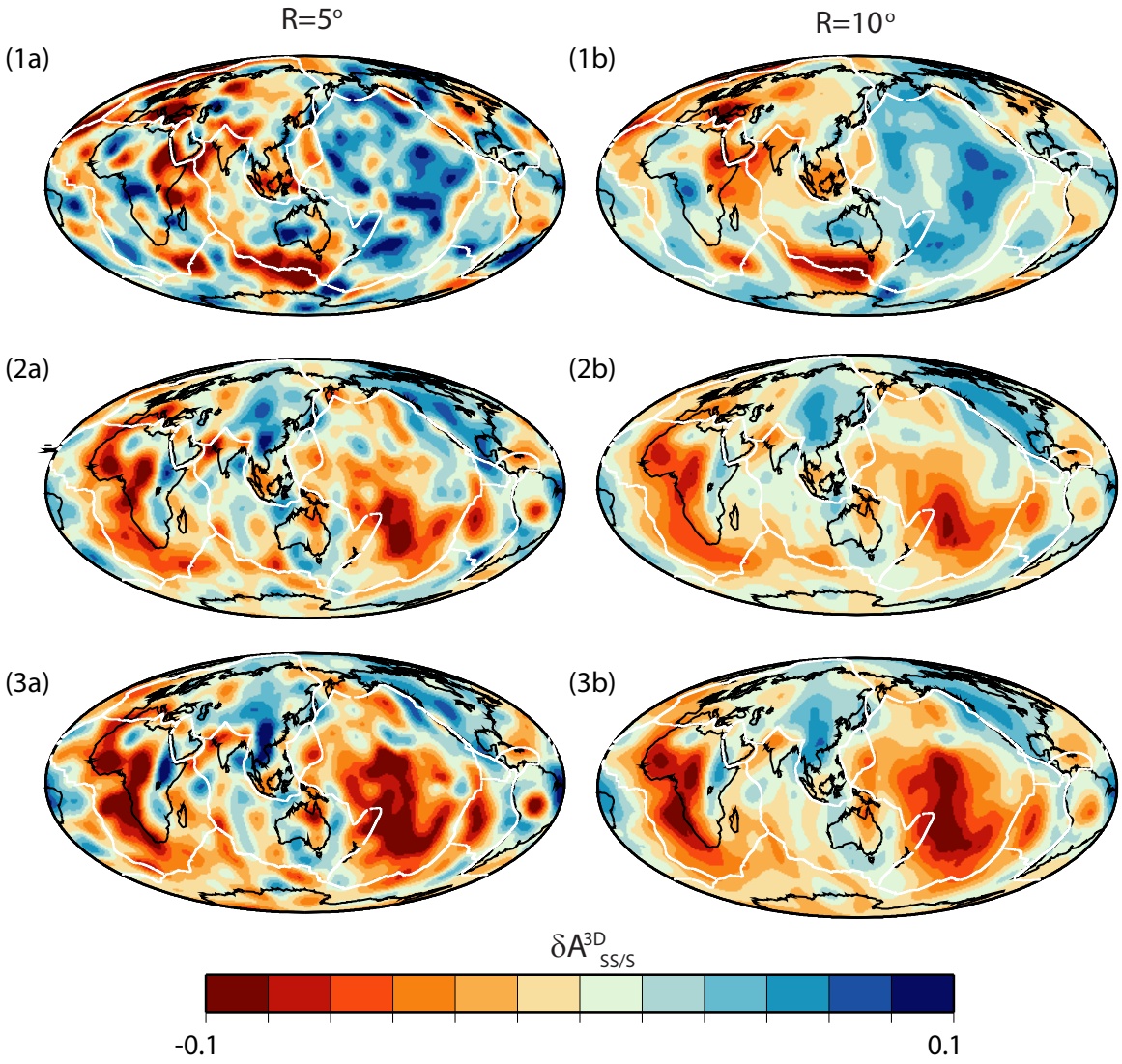

Figure 5.10: Distance dependence of SS/S amplitudes global simulations from S20RTS (*Ritsema et al.*, 1999) models, plotted with epicentral distances (1)<90^o, (2)>90^o and (3)>110^o using cap sizes of 5 and 10^o.

CHAPTER VI

Conclusions

Over the past decades, seismologists have made significant progress in the modeling of the Earth's structure in multiple scales. This dissertation focuses on refining models of the elastic and anelastic structure of the Earth using seismic traveltimes and amplitudes. The complexity of models for the deep mantle is steadily increasing, with both the radial and lateral scale lengths revealed by seismic waveform amplitudes and travel times. Features mainly detected and discussed in this thesis include a seismic velocity gradient in D" about 200–300 km above the CMB, a thin ultralow velocity layer in the deepest 5–50 km of the mantle at the source side, and the presence of the Pacific anomaly at the base of the mantle. The seismic characteristics of these features are summarized in the Table 6.1. It takes advanced numerical methods to address the complexities in the heterogeneous mantle locally and globally. Below I first discuss the advantages of the methods I take and then summarize how my findings impact our understanding the thermal, chemical and compositional state of the Earth mantle. Finally I illustrate the possible new research directions in the future.

Table 6.1: Seismically observed lower mantle features

Feature	**Thickness**	**Vs(%)**	**Vp(%)**	**Lateral extent***
LLSVP	500–1500	-3 to -12	-1 to -3	widely spread
D" discontinuity	200–300	-1 to -2	$\sim<1$	40–60^o
ULVZ	5–30	-10 to -30	-5 to -10	5–15^o

*: the epicentral distances from the earthquake from Fiji-Tonga region

6.1 Body wave studies combined with 3-D advanced numerical modeling

Although 1D modeling procedures are effective and easy to apply, 2D and 3D waveform simulations are increasingly applied to imaging the deep mantle. The presence of strong heterogeneity with geometries requires advanced numerical methods for calculating synthetics for realistic structures. With the gradual emergence of 3D numerical modeling capabilities, it should become possible to more thoroughly explore these effects and to process higher-frequency 3D wavefield simulations to better evaluate the models of the fine-scale structures.

However, before fully applying the 3-D simulations, we begin by evaluating how tomographic models explain waveforms and whether modeling simplification affect the quality of seismic models. Ray theory is widely applied to approximate propagating seismic waves. However, in Chapter 4 of the thesis, it is demonstrated that the ray-theoretical traveltime calculations through long-wavelength shear-velocity models are imprecise. Differences of several seconds confirm the noticeable possible error generated from ray-theoretical approximation. On the other hand, because the data sources for the tomographic inversion are mostly from phase traveltime and surface waves, the ability of the current tomographic models to reflect other wave features (e.g., wave amplitudes) are questionable. Our examination in Chapter 5 further prove the inconsistency between the 3-D simulated SS/S amplitude ratios and the observations. Overall, we illustrate that with the rapid increasing 3D numerical modeling capabilities, the inability of the current seismic tomography techniques should be

further noticed and improved.

On the other hand, tomographic images still provide a important reference to finer-scale body wave studies. For example, the modeling of the Earth's lower mantle through the use of seismic wave-travel time tomography show some consistency (e.g. *Ritsema and van Heijst*, 2000; *Gu et al.*, 2001; *Grand*, 2002; *Antolik et al.*, 2003; *Zhao*, 2004; *Panning and Romanowicz*, 2006; *Takeuchi*, 2007; *Kustowski et al.*, 2008; *Li et al.*, 2008), especially for the two LLSVPs. Using body wave phases, especially near the core-mantle boundary (CMB) where various reflections, refractions, and diffractions of seismic energy occur, we can reveal a greater level of detail in seismic imaging in addition to tomography. Recent body wave analyses have complemented the earlier findings from tomographic inversions of global travel time data sets, adding detail to some of the long wavelength features observed in tomographic models (see recent discussion by *Lay et al.* (2004); *Lay and Garnero* (2004); *Garnero* (2004). In Chapter 2 and Chapter 3, our detailed analysis of the Pacific lower mantle provide constraints on shear-velocity for both the radial and lateral lengths derived from simulations of a hybrid of tomography and fine structured revealed by body wave studies.

However, a main restriction in high-resolution body wave studies is the geographic coverage limitations imposed by earthquake-to-seismic recording network configurations. There still are some intrinsic ambiguities on the extend and sharpness of the LLSVPs. The widely use of seismic amplitudes and waveforms, as well as seismic reflections, could manifest the rough, fine-scale structures. On the other hand, refining global tomography further can be essential for improving the resolution of the smooth large-scale structures too. A unified picture which involve both broad and subtle features of the deep mantle is need to be detected and quantified.

6.2 Incorporation with other geophysical disciplines

The rigorous environments of the bottom of the lower mantle suggesting an interaction between the shallowest and deepest mantle. A principle challenge to constrain the origin of these features, as well as their possible connection to the evolution and dynamic behavior of the lower mantle. In this regard, incorporating information from other geophysical disciplines will be crucial.

The D" and CMB region have undoubtedly played a significant role in both the core and mantle dynamic systems throughout the 4.50-Gyr evolution of the Earth (*Lay et al.*, 1998). The regions are thought to be the graveyard of subducted slabs and the birth place of mantle plumes. The "superplumes" beneath the central Pacific and Africa are proposed to be generated by thermal boundary layer instabilities at the CMB (*Stacey and Loper*, 1983; *Sleep*, 1990; *Thompson and Tackley*, 1998). The LLSVP density is important with respect to whether these are large, buoyant , thermal "superplumes" or hot, dense piles of distinct material swept into their present configuration by surrounding downwellings and upwellings (*Tan et al.*, 2002; *McNamara and Zhong*, 2004, 2005). A strong correlation between the present-day configuration of LLSVPs and reconstructed emplacement locations for large igneous provinces dating back several hundred million years implies long-term stability of LLSVPs (*Burke and Torsvik*, 2004; *Torsvik et al.*, 2006, 2010; *Wen*, 2006; *Burke et al.*, 2008), with ongoing internal deformation (*McNamara et al.*, 2003; *Tan and Gurnis*, 2005; *Sun et al.*, 2007). The longevity of large-scale structures of the deep mantle is highly relevant to history of the geodynamo (*Glatzmaier et al.*, 1999).

The formation of the D" discontinuity is revealed by the discovery of a phase change of perovskite (*Murakami et al.*, 2004), which can provide a plausible explanation for both P- and S-waves. The temperature and compositional dependency of this phase change and the predicted elasticity and transport purparties of the high-pressure polymorph, known as postperovskite, provide the first predictive context for

evaluating the seismological images (*Lay et al.*, 2005; *Wookey et al.*, 2005; *Lay and Garnero*, 2007). Previous studies show variations in depth of an abrupt shear velocity discontinuity can be related to relative temperature fluctuations (*Helmberger et al.*, 2005; *Sun and Helmberger*, 2008). Double discontinuities with opposite sign can be related to multiple intersections of the local geotherm with the phase boundary and with temperature gradients and heat flow (*Hernlund et al.*, 2005; *Lay et al.*, 2006; *van der Hilst et al.*, 2007; *Lay et al.*, 2008). Further, anisotropic properties can be predicted and compared with observations (e.g. *Wookey et al.*, 2005; *Kawai and Tsuchiyac*, 2009).

The exhibited ULVZs under south-central Pacific and Africa are interpreted as partial melts (*Williams and Garnero*, 1996). In addition, the possible role of partial melting in the deep mantle has many present-day thermal and dynamical implication (e.g. *Lay et al.*, 2004) as well as possible implications for dense melt segregation in a deep mantle magma ocean over all of Earth history (*Labrosse et al.*, 2007). Some chemical heterogeneity, possibly involving core material (iron), may be present as well (*Knittle and Jeanloz*, 1991). It is dynamically possible for the heavier iron to be pulled upward by strong enough thermal buoyant forces, as shown in numerical simulation (*Hansen and D.Yuen*, 1988; *Yuen et al.*, 1993; *Cadek et al.*, 1994). ULVZs may be a manifestation of very high iron content in a thin layer of subsolidus postperovskite (*Mao et al.*, 2006), although it appears more likely that iron preferentially partitions into ferropericlase in the deep mantle. Others (e.g. *Hirose and Lay*, 2008) have argued that iron should partition out of the lower mantle into the outer core, leading to Fe-depletion in parts of D".

Attenuation is sensitive to temperature variations. Many important geophysical processes (mantle convection, plate tectonics, magmatism, etc.) involve lateral variations in temperature. The low attenuation in the asthenosphere provide evidence for the possibly existence of partial melting (*Karato and Jung*, 1998). More infor-

mation on lateral variations of attenuation can be gained by tomographic method (*Romanowicz*, 1995). The significant attenuation variations can be explained by regions where temperature vary over short distances, such as mid-ocean ridge, or the back-arc spreading center above the Tonga subduction (*Roth et al.*, 1999). The combining velocity and attenuation studies can provide valuable information.

6.3 Future work

Though models for the deep mantle are steadily becoming more complex, the studies on the large-scale patterns of lower-mantle heterogeneity are not yet reliably resolved. Moreover, possibly the parameterizations of the current tomographic models and our ignorance of detailed near-source and near-receiver complexities are still blemishing our understanding of deep mantle structure.

Despite that, the discovered shear velocity and attenuation features in the upper and lower mantle strongly suggest a dynamic convective system. If the velocity heterogeneity is caused by temperature, fluctuations of several hundred degrees would occur in the deep mantle. This is sufficient to induce density heterogeneity that will in turn drive solid-state convection. The convective flow could be continuously revealed by the seismic images, and lead to resolution of the whole mantle dynamic configuration. The combined structures and boundary layers at the base of the mantle could attribute to the distribution of chemical heterogeneities, flow structures, and zones of partial melting. Clearly, high-resolution studies are needed to resolve this issue.

The investigation using waveform amplitudes and traveltimes on the velocity and attenuation structures of the deep mantle in this thesis appear to be effective. The seismologically imaged features in the deep mantle provide first-order information regarding structures and processes. But we still need the joint interpretation with mineral physics and geodynamics information is required to evaluate the thermochemical significant of the structures (e.g. *Forte and Mitrovica*, 2001; *Deschamps and*

Trampert, 2003; *Resovsky et al.*, 2005; *Trampert et al.*, 2004). A new paradigm of the deep mantle evolution is gradually putted together (*Garnero et al.*, 2007; *Garnero and McNamara*, 2008; *Tronnes*, 2009).

APPENDICES

APPENDIX A

2.5-D and 3D methods: SHaxi/PSVaxi and SEM

A.1 SHaxi/PSVaxi

SHaxi (and its P-SV version PSVaxi), is a method to calculate high-frequency global SH (and P, SV) seismograms with axisymmetric geometries (*Jahnke et al.*, 2008). For teleseismic distances, a substantial part of the seismic energy travels within the great circle plan and can be approximated under the assumption that invariance are in the out of plan direction. In the method, we only compute the wavefield with the ignorance of the out of plane direction and the focuses on the two reminding dimensions, and the corresponding physical 3-D model is achieved by a virtually rotation of the 2-D domain around a symmetry axis. The method limited the consuming computing efforts by the restriction of axisymmetry, as well as preserving the correct geometrical spreading that can formerly only be achieved by 3-D methods. Such a scheme is as a mixture of strengths of 2-D and 3-D methods and refer it as 2.5-D methods. The applied ring-source to produce synthetics is equivalent to a vertical strike-slip source, which is arbitrary. But in the case of our thesis (Chapter 2,3), the method is very useful and suited for investigating relative

amplitude and/or traveltimes. Moreover, the reduction of the computational effort has permitted the production of the waveforms at higher frequencies (e.g. up to 1Hz dominant frequencies) that are not currently feasible with 3-D methods.

In Chapter 2 and 3, our usage of synthetic seismograms are around the period of 10 seconds. In addition, Chapter 2 examine the frequency effect of the SKKS/SKS amplitude ratio. In those cases, SHaxi/PSVaxi provide a better alternative to fully 3-D techniques such as SEM. The 3-D structures of ULVZs, LLSVP and complex structure of D" are incorporated into SHaxi/PSVaxi to achieve the correct fully 3-D synthetic seismograms at a much lower computational cost. The list of models produced by SHaxi/PSVaxi in Chapter 2 and 3 are listed separately in Table A.1 and Table A.2. The scattering of the mantle structures, the length scales and spatial location of those small-scale seismic heterogeneity are modeled and explained. Example of computed synthetics is shown in Figure A.2, which indicate the included small-scale velocity structure can broad the pulse width and delay their peak arrivals. A general record section of both data and synthetics produced from multiple methods are also showing in Figure A.1, which in addition shows the frequency information. The changes on the waveforms are discussed and explained accordingly in former chapters. Overall, the method of SHaxi/PSVaxi can provide important intuition into the wavefield for higher dimensional geometries, and is of great meaning to our modeling procedure.

A.2 SEM

In the thesis, 1-D synthetics are produced using two methods. Normal-mode summation is used (Chapter 5) to produce SS/S amplitude ratios with changing Q profiles, in which one sums spherical eigenfunctions. The reflectivity method is used when producing the synthetics for 1-D shear velocity models underneath Pacific (Chapter 2,3) (example synthetics shown in Figure A.1), in which we sum the reflections from a layered model in the frequency-wavenumber domain. However, to explore the lateral

variation of the Earth structure, we need to find a method to compute seismograms in three-dimensional (3D) Earth, such as shear-velocity model S20RTS.

SEM combined the strengths of both current finite-difference and pseudospectral techniques with a better griding of the globe. In a SEM, the wave field is expressed in terms of high-degree Lagrange polynomials on Gauss-Lobatto-Legendre interpolation points. The mesh of the SEM method is based on the so-called "quasi-uniform gnomonic projection". The mesh honors the first- and second-order discontinuities and 1-D model and accommodated other factors such as crust, surface topography, ellipticity, attenuation. Processors are taking separate slices of the constituting blocks and calculate the propagating waves. The communication to neighboring slices are done by using the Message-Passing Interface (MPI). The SEM include the physical dispersions of surface waves and diffracted body waves, which is particular important for the study of velocity model building, earthquake rupture, and the core-mantle boundary region. On the other hand, the SEM tried to accurately incorporate efforts of velocity and density heterogeneity, anisotropy, anelasticity, sharp velocity and density contrasts, crustal thickness variations, topography, ellipticity, rotation, self-gravitation. With including/excluding the above factors, and with the implementation of multiple versions of tomography models (as in Chapter 4,5), we are able to evaluate the quality of the robustness of the current tomographic models, and compare the ray-theory prediction with the prediction measured directly from 3-D synthetic waveforms. Example records from model T1, T2, T3 (different damping) are shown in Figure A.3 with a Fiji region earthquake and the seismic station located in Ann Arbor, MI.

We have implement the SEM for global wave propagation on a cluster of personal computers (PCs), the "flux" cluster* with 150 processors. The parallel computing allow the frequency range up to about 50 mHz, ant take about 12 hours to compute seismograms with a duration of 60 min for a single earthquake location. However,

theoretically, there is no upper limit to the seismic frequency content that can be reached by the SEM. With stronger computational power, the SEM will provide 3-D synthetics with higher frequency, which could benefit the detailed forward modeling studies and the development of global tomography.

[1]http://cac.engin.umich.edu/resources/systems/flux/index.html

Table A.1: Synthetic ULVZ models by PSVaxi

Model nums	Thickness (km)	Vs (%)	Vp (%)	Density (%)	Type(Dis/Grad)
Model1	5	30	10	10	Dis
Model2	10	30	10	10	Dis
Model3	15	30	10	10	Dis
Model4	20	30	10	10	Dis
Model5	5	30	10	10	Grad
Model6	10	30	10	10	Grad
Model7	15	30	10	10	Grad
Model8	20	30	10	10	Grad
Model9	10	18	6	10	Dis
Model10	10	18	12	10	Dis
Model11	10	18	18	10	Dis
Model12	10	6	2	10	Dis
Model13	10	18	6	10	Dis
Model14	10	30	10	10	Dis
Model15	10	30	10	50	Dis

[1]The compressional velocity, shear velocity and density reductions are all compared to PREM values. The last column specify if the reduction is a discontinuity or a gradient added. Synthetics of PSV components are produced with epicentral distances 90–140^o.

Table A.2: Synthetic tomographic models by SHaxi/PSVaxi

Model nums	Damping	Azimuth (°)	Degree (°)	M1 (°)	ULVZ (°)
Model1	2000	60	0–180	-	-
Model2	200	60	0–180	-	-
Model3	20000	60	0–180	-	-
Model4	2000	40	0–180	-	-
Model5	2000	45	0–180	-	-
Model6	2000	50	0–180	-	-
Model7	2000	55	0–180	-	-
Model8	2000	60	0–90	-	-
Model9	20000	60	0–90	-	-
Model10	2000	60	90–180	-	-
Model11	20000	60	90–180	0–180	-
Model12	2000	60	0–180	0–180*	-
Model13	2000	60	0–180	40–60	-
Model14	2000	60	0–180	40–70	-
Model15	2000	60	0–180	40–80	-
Model16	2000	60	0–180	40–60	5–15

*: M1-type negative gradient with shear velocity reduction 1.5 – 1.875%

[1]The velocity structure of S20RTS with the source from latitude 40^o, longitude -110^o, are used to produce 3 components with epicentral distances 80–140^o.

Table A.3: Earthquakes for SEM simulations

Event name	Region	Date	Depth (km)	M_W
011197D	MICHOACAN, MEXICO	1997/01/11	33.0	7.1
020497C	IRAN-USSR BORDER REGION	1997/02/04	10.0	6.5
020594B	UGANDA	1994/02/05	10.0	6.2
021294B	SOUTH PACIFIC OCEAN	1994/02/12	10.0	6.6
021696A	NORTH OF ASCENSION ISLA	1996/02/16	10.0	6.5
021995C	OFF COAST OF NORTHERN CA	1995/02/19	10.0	6.6
022797E	PAKISTAN	1997/02/27	33.0	7.1
030396B	NEAR COAST OF NICARAGUA	1996/03/03	33.0	6.6
030596B	TAIWAN REGION	1996/03/05	30.0	6.3
031696C	BONIN ISLANDS REGION	1996/03/16	477.0	6.6
032896C	ARABIAN SEA	1996/03/28	10.0	6.1
033195B	SEA OF JAPAN	1995/03/31	365.0	6.1
041795B	NORTH ATLANTIC RIDGE	1995/04/17	10.0	6.1
042397G	MARIANA ISLANDS	1997/04/23	101.0	6.5
042897C	PRINCE EDWARD ISLANDS REGION	1997/04/28	10.0	6.7
051094C	SANTIAGO DEL ESTERO PRO	1994/05/10	605.0	6.9
051197F	WEST CHILE RISE	1997/05/11	10.0	6.5
060296D	NORTH ATLANTIC RIDGE	1996/06/02	10.0	6.9
060696B	MID-INDIAN RISE	1996/06/06	20.0	6.2
061096A	VANUATU ISLANDS	1996/06/10	200.0	6.7
061196J	SAMAR, PHILIPPINE ISLANDS	1996/06/11	33.0	7.1
061797F	ANDREANOF ISLANDS, ALEUT	1997/06/17	33.0	6.4
062195A	BALLENY ISLANDS REGION	1995/06/21	10.0	6.7
062296A	BOUVET ISLAND REGION	1996/06/22	10.0	6.4
062797A	AZORES ISLANDS	1997/06/27	10.0	5.8
070997C	NEAR COAST OF VENEZUELA	1997/07/09	19.9	6.9
071696C	MINAHASSA PENINSULA	1996/07/16	33.0	6.5
080596E	OFF COAST OF ECUADOR	1996/08/05	33.0	6.3
080897C	FIJI ISLANDS REGION	1997/08/08	10.0	6.6
081097A	WESTERN AUSTRALIA	1997/08/10	10.0	6.2
081307E	SOUTHERN MID-ATLANTIC RIDGE	2007/08/13	10.0	5.5
081495A	NEW BRITAIN REGION	1995/08/14	126.0	6.7
081895B	SOUTH SANDWICH ISLANDS	1995/08/18	36.0	6.2
082506B	SICHUAN, CHINA	2006/08/25	21.8	5.0
090297B	COLOMBIA	1997/09/02	198.7	6.7
090596B	EASTER ISLAND REGION	1996/09/05	10.0	6.8
090895B	EASTER ISLAND CORDILLER	1995/09/08	10.0	6.3
091594E	SOUTHWESTERN ATLANTIC OCEAN	1994/09/15	10.0	6.0
092793C	SOUTH OF FIJI ISLANDS	1993/09/27	33.0	6.6
101498A	WESTERN GREENLAND	1998/10/14	10.0	5.0
101706D	CENTRAL ALASKA	2006/10/17	115.8	5.3
102794C	SOUTH OF FIJI ISLANDS	1994/10/27	549.0	6.6
110195A	NEAR COAST OF CENTRAL CH	1995/11/01	20.0	6.6
110594A	MACQUARIE ISLANDS REGION	1994/11/05	10.0	6.3
110595E	SOUTHERN SUMATERA	1995/11/05	58.0	6.3
111897B	IONIAN SEA	1997/11/18	33.0	6.6
112295A	ARAB REPUBLIC OF EGYPT	1995/11/22	10.0	7.2
112495A	SOUTH ISLAND, NEW ZEALA	1995/11/24	10.0	6.1
112897C	PERU-BOLIVIA BORDER REGION	1997/11/28	586.0	6.6
123199D	POLAND	1999/12/31	5.0	5.4

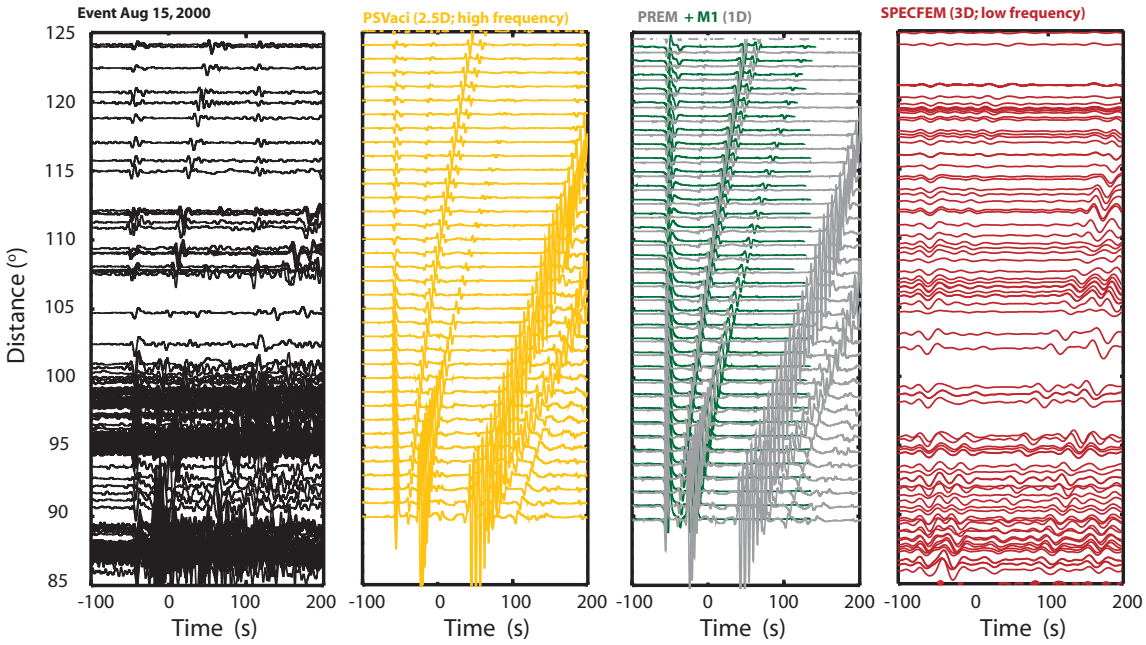

Figure A.1: Record sections for 1D/2.5D/3D methods are shown. Comparisons are made using the reflectivity (*Fuchs and Muller*, 1971), SEM (*Komatitsch et al.*, 2002) and PSVaxi (*Jahnke et al.*, 2008) methods. Seismograms are aligned by the synthetic arrival of SKS phase.

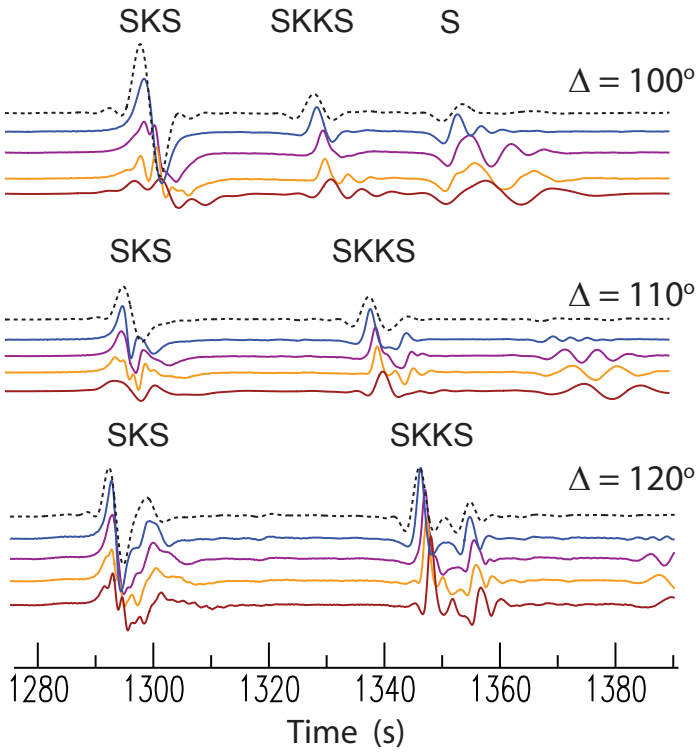

Figure A.2: Example synthetics of ULVZ models from PSVaxi (*Jahnke et al.*, 2008) are plotted with thickness 5 (blue), 10 (purple), 15 (yellow), 20 (red) km. Synthetics produced with PREM (*Dziewonski and Anderson*, 1981) (black dash) is also plotted for comparison. All seismograms are aligned by SKS. Phases SKS and SKKS (and S) are shown with the epicentral distances 100, 110, 120^o.

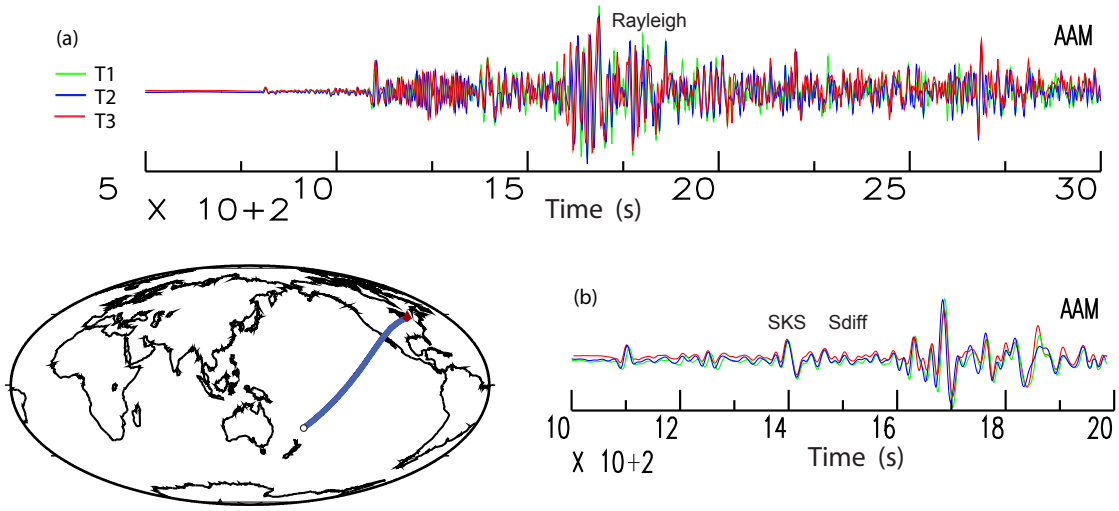

Figure A.3: Example synthetics from SEM runs with damping model T1, T2, T3. Fiji region earthquake (102794C) is recorded at the station AAM (δ=112^o). Waveforms are shown in two time windows with certain body waves and Rayleigh waves noted with the effect of damping more clearly displayed.

BIBLIOGRAPHY

BIBLIOGRAPHY

Adams, R. D. (1968), Early reflections of P'P' as an indication of upper mantle structure, *Bull. Seismol. Soc. Amer.*, *58*(6), 1933–1947.

Aki, K., and P. G. Richards (1980), Quantitative Seismology, W. H. Freeman and Co., San Francisco, California.

Antolik, M., Y. Gu, and G. Ekström (2003), J362D28: a new joint model of compresssional and shear velocity in the Earth's mantle, *Geophys. J. Int.*, *153*, 443–66.

Avants, M., T. Lay, S. Russell, and E. Garnero (2006), Shear velocity variation within the D" region beneath the central Pacific, *J. Geophys. Res.*, *111*(B5).

Bassin, C., G. Laske, and G. Masters (2000), The current limits of resolution for surface wave tomography in north america, *Eos Trans. AGU*, *81*, F897.

Bhattacharyya, J., G. Masters, and P. Shearer (1996), Global lateral variations of shear wave attenuation in the upper mantle, *J. Geophys. Res.*, *101*(B10), PP. 22,273–22,289, doi:199610.1029/96JB01782.

Bina, C. R., and G. Helffrich (1994), Phase transition Clapeyron slopes and transition zone seismic discontinuity topography, *J. Geophys. Res.*, *99*, 15,853–15,860.

Buffett, B. A., E. J. Garnero, and R. Jeanloz (2000), Sediments at the top of earth's core, *Science*, *290*(5495), 1338 –1342, doi:10.1126/science.290.5495.1338.

Bull, A. L., A. K. McNamara, and J. Ritsema (2009), Synthetic tomography of plume clusters and thermochemical piles, *Earth Planet. Sci. Lett.*, *278*, 152–162.

Bullen, K. (1949), An earth model based on a compressibility-pressure hypothesis, *Geophys. J. Roy. Astr. Soc.*, *109*(6), 720.

Burke, K., and T. Torsvik (2004), Derivation of large igneous provinces of the past 200 million years from long-term heterogeneities in the deep mantle, *Earth Planet. Sci. Lett.*, *227*, 531–38.

Burke, K., B. Steinberger, T. Torsvik, and M. Smethurst (2008), Plume generation zones at the margins of large low shear velocity provinces on the core-mantle boundary, *Earth Planet. Sci. Lett.*, *265*, 49–60.

Cadek, O., D. Yuen, V. Steinbach, A. Chopelas, and C. Matyska (1994), Lower mantle thermal structure deduced from seismic tomography, mineral physics and numerical modeling, *Earth Planet. Sci. Lett.*, *121*, 385–402.

Castle, J., and R. van der Hilst (2000), The core-mantle boundary under the Gulf of Alaska: no ULVZ for shear waves, *Earth Planet. Sci. Lett.*, *176*, 311C321.

Castle, J. C., and R. ver der Hilst (2003), Using ScP precursors to search for mantle structures beneath 1800 km depth massachusetts institute of technology, cambridge, massachusetts, USA, *Geophys. Res. Lett.*, *30*(8), doi:10.1029/2002GL016,023.

Chaljub, E., and A. Tarantolla (1997), Sensitivity of *SS* precursors to topography on the upper-mantle 660-km discontinuity, *Geophys. Res. Lett.*, *24*, 2613–2616.

Choy, G. (1977), Theoretical seismograms of core phase calculated by frequency-dependent full-wave theory, and their interpretation, *Geophys. J. Roy. Astr. Soc.*, *51*(2), 275–311.

Cormier, V. (2000), D" as a transition in the heterogeneity spectrum of the lowermost mantle, *J. Geophys. Res.*, *105*, 16,193–16,205.

Crotwell, H. P., T. J. Owens, and J. Ritsema (1999), The Taup Toolkit: Flexible seismic travel-time and ray-path utilities, *Seism. Res. Lett.*, *70*, 154–160.

Dahlen, F. A. (2005), Finite-frequency sensitivity kernels for boundary topography perturbations, *Geophys. J. Int.*, *162*, 525–540.

Dahlen, F. A., S. Hung, and G. Nolet (2000), Frechet kernels for finite-frequency traveltimes-I. theory, *Geophys. J. Int.*, *141*(1), 157–174, doi:10.1046/j.1365-246X.2000.00070.x.

Dalton, C. A., and G. Ekström (2006), Global models of surface wave attenuation, *J. Geophys. Res.*, *111*, 19 PP., doi:200610.1029/2005JB003997.

Dalton, C. A., G. Ekström, and A. M. Dziewonski (2008), The global attenuation structure of the upper mantle, *J. Geophys. Res.*, *113*, 24 PP., doi: 200810.1029/2007JB005429.

Deschamps, F., and J. Trampert (2003), Mantle tomography and its relation to temperature and composition, *Phys. Earth Planet. Inter.*, *140*, 272–91.

Deuss, A. (2007), Seismic observations of transition zone discontinuities beneath hotspot locations, in *Plates, Plumes, and Planetary Processes*, vol. 430, edited by G. Foulger and J. Jurdy, pp. 121–136, GSA, Boulder, CO.

Deuss, A. (2009), Global observations of mantle discontinuities using SS and PP precursors, *Surv. Geophys.*, *30(4-5)*, 301–326.

Dueker, K. G., and A. F. Sheehan (1998), Mantle discontinuity structure beneath the colorado rocky mountains and high plains, *J. Geophys. Res*, *103*(B4), PAGES 7153–7169.

Dziewonski, A. M., and D. L. Anderson (1981), Preliminary reference Earth model, *Phys. Earth Planet. Int.*, *25*, 297–356.

Dziewonski, A. M., B. H. Hager, and R. J. O'Connell (1977), Large scale heterogeneity in the lower mantle, *J. Geophys. Res.*, *82*, 239–255.

Dziewonski, A. M., V. Lekic, and B. A. Romanowicz (2010), Mantle Anchor Structure: An argument for bottom up tectonics, *Earth Planet. Sci. Lett.*, *299*(1–2), 69–79.

Flanagan, M. P., and P. M. Shearer (1998), Global mapping of topography on transition zone velocity discontinuities by stacking *SS* precursors, *J. Geophys. Res.*, *103*, 2673–2692.

Ford, S., E. Garnero, and A. McNamara (2006), A strong lateral shear velocity gradient and anisotropy heterogeneity in the lowermost mantle beneath the southern Pacific, *J. Geophys. Res.*, *111*(B3), doi:10.1029/2004JB003574.

Forte, A. M., and J. X. Mitrovica (2001), Deep-mantle high-viscosity flow and thermochemical structure inferred from seismic and geodynamic data, *Nature*, *410*(6832), 1049–1056, doi:10.1038/35074000.

Fouch, M., K. Fischer, and M. Wysession (2001), Lowermost mantle anisotropy beneath the Pacific: Imaging the source of the Hawaiian plume, *Earth Planet. Sci. Lett*, *190*(3-4), 167–180.

Frost, D. J. (2008), The upper mantle and transition zone, *Elements*, *4(3)*, 171–176, doi:10.2113/GSELEMENTS.4.3.171.

Fuchs, K., and G. Muller (1971), Computation of synthetic seismograms with reflectivity method and comparison with observations, *Geophys. J. Roy. Astr. Soc.*, *23*(4), 417–433.

Gaherty, J. B., and T. Lay (1992), Investigation of laterally heterogeneous shear velocity structure in d" beneath eurasia, *J. Geophys. Res.*, *97*, 417–435.

Garnero, E. (2004), A new paradigm for Earth's core-mantle boundary, *Science*, *304*(5672), 834–836.

Garnero, E., and D. Helmberger (1996), Seismic detection of a thin laterally varying boundary layer at the base of the mantle beneath the central-Pacific, *Geophys. Res. Lett.*, *23*(9), 977–980.

Garnero, E., and D. Helmberger (1998), Further structural constraints and uncertainties of a thin laterally varying ultralow-velocity layer at the base of the mantle, *J. Geophys. Res*, *103*(B6), 12,495–12,509.

Garnero, E., and R. Jeanloz (2000), Fuzzy patches on the Earth's core-mantle boundary?, *Geophys. Res. Lett.*, *27*(17), 2777–2780.

Garnero, E., T. Lay, and A. McNamara (2007), Implications of lower-mantle structural heterogeneity for existence and nature of whole-mantle plumes, *Geol. Soc. Am. Spec. Pap.*, *430*, 79–91.

Garnero, E., D. Helmberger, and S. Grand (1993), Constraining outermost core velocity with SmKS waves, *Geophys. Res. Lett.*, *20*(22), 2463–2466.

Garnero, E., J. Revenaugh, Q. Williams, T. Lay, and L. Kellogg (1998), Ultralow velocity zone at the core-mantle boundary, in *Core-mantle Boundary Region*, *Geodynamics Series*, vol. 28, pp. 319–334, AGU.

Garnero, E. J., and A. K. McNamara (2008), Structure and dynamics of Earth's lower mantle, *Science*, *320*, 626–628.

Garnero, E. J., and J. E. Vidale (1999), ScP; a probe of ultralow velocity zones at the base of the mantle, *Geophys. Res. Lett*, *26*(3), 377–380.

Glatzmaier, G., R. Coe, L. Hongre, and P. Roberts (1999), The role of the Earth's mantle in controlling the frequency of geomagnetic reversals, *Nature*, *401*, 885–90.

Grand, S. (2002), Mantle shear-wave tomography and the fate of subducted slabs, *Philo. Trans. Roy. Soc. Lond. Series A, Math. Phys. Sci.*, *360*(1800), 2475–2491.

Gu, Y. J., and A. M. Dziewonski (2002), Global variability of transition zone thickness, *J. Geophys. Res.*, *107(B7)*, 2135, doi:10.1029/2001JB000489.

Gu, Y. J., A. M. Dziewonski, and G. Ekström (2001), Preferential detection of the Lehmann discontinuity beneath continents, *Geophys. Res. Lett.*, *28*, 4655–4658.

Gu, Y. J., A. M. Dziewonski, and G. Ekström (2003), Simultaneous inversion for mantle shear velocity and topography of transition zone discontinuities, *Geophys. J. Int.*, *154*, 559–583.

Gu, Y. J., Y. An, M. Sacchi, R. Schultz, and J. Ritsema (2009), Mantle reflectivity structure beneath oceanic hotspots, *Geophys. J. Int.*, *178*, 1456–1472.

Gurnis, M., J. X. Mitrovica, J. Ritsema, and H. J. V. Heijst (2000), Constraining mantle density structure using geological evidence of surface uplift rates: The case of the African Superplume, *Geochem. Geophys. Geosyst.*, *1*(7), 1020.

Hager, B., R. Clayton, M. Richards, R. Comer, and A. Dziewonski (1985), Lower mantle heterogeneity dynamic topography and the geoid, *Nature*, *313(6003)*, 541–546.

Hansen, U., and D.Yuen (1988), Numerical simulation of thermal chemical instabilities at the core-mantle boundary, *Nature*, *334*, 237–240.

He, Y., and L. Wen (2009), Structural features and shear-velocity structure of the "Pacific Anomaly", *J. Geophys. Res.*, *114*, doi:10.1029/2008JB005814.

He, Y., L. Wen, and T. Zheng (2006), Geographic boundary and shear wave velocity structure of the "Pacific anomaly" near the core-mantle boundary beneath western Pacific, *Earth Planet. Sci. Lett.*, *244*(1-2), 302–314, doi:10.1016/j.epsl.2006.02.007.

Hedlin, M., and P. Shearer (2000), An analysis of large-scale variations in small-scale mantle heterogeneity using Global Seismographic Network recordings of precursors to PKP, *J. Geohys. Res.*, *105*, 13,655–13,673.

Helffrich, G. (2000), Topography of the trasition zone seismic discontinuities, *Rev. Geophys.*, *63*, 141–158.

Helmberger, D., T. Lay, S. Ni, and M. Gurnis (2005), Deep mantle structure and the postperovskite phase transition, *PROCEEDINGS OF THE NATIONAL ACADEMY OF ScienceS OF THE UNITED STATES OF AMERICA*, *102*(48), 17,257–17,263.

Hernlund, J. W., and P. J. Tackley (2007), Some dynamical consequences of partial melting in Earth's deep mantle, *Phys. Earth Planet. Inter.*, *162*(1-2), 149–163.

Hernlund, J. W., C. Thomas, and P. J. Tackley (2005), A doubling of the post-perovskite phase boundary and structure of the Earth's lowermost mantle, *Nature*, *434*, 882–886, doi:10.1038/nature03472.

Hirose, K. (2002), Phase transitions in pyrolitic mantle around 670-km depth: Implications for upwelling of plumes from the lower mantle, *J. Geophys. Res.*, *107(B4)*, 2078, doi:10.1029/2001JB000597.

Hirose, K., and T. Lay (2008), Discovery of Post-Perovskite and New Views on the Core-Mantle Boundary Region, *Elements*, *4*(3), 183–189.

Houser, C., and Q. Williams (2010), Reconciling pacific 410 and 660 km discontinuity topography, transition zone shear velocity patterns, and mantle phase transitions, *Earth Planet. Sci. Lett.*, *296*, 255–266.

Houser, C., G. Masters, M. Flanagan, and P. M. Shearer (2008), Determination and analysis of long-wavelength transition zone structure using *SS* precursors, *Geophys. J. Int.*, *174*, 178–194.

Hutko, A. R., T. Lay, and J. Revenaugh (2009), Localized double-array stacking analysis of PcP: D" and ULVZ structure beneath the Cocos plate, Mexico, central Pacific, and north Pacific, *Phys. Earth Planet. Inter.*, *173*(1-2), 60–74.

Idehara, K., A. Yamada, and D. Zhao (2007), Seismological constraints on the ultralow velocity zones in the lowermost mantle from core-reflected waves, *Phys. Earth Planet. Inter.*, *165*(1-2), 25–46.

Igel, H., and M. Weber (1996), P-SV wave propagation in the Earth's mantle using finite differences: Application to heterogeneous lowermost mantle structure, *Geophys. Res. Lett.*, *23*(5), 415–418.

Iitaka, T., K. Hirose, K. Kawamura, and M. Murakami (2004), The elasticity of the MgSiO3 post-perovskite phase in the Earth's lowermost mantle, *Nature*, *430*(6998), 442–445, doi:10.1038/nature02702.

Ishii, M., and J. Tromp (2001), Even-degree lateral variations in earth mantle constrained by free oscillations and the free-air gravity anomaly, *Geophys. J. Int.*, *145*, 77–96.

Jahnke, G., M. S. Thorne, A. Cochard, and H. Igel (2008), Global SH-wave propagation using a parallel axisymmetric spherical finite-difference scheme: application to whole mantle scattering, *Geophys. J. Int.*, *173*(3), 815–826.

Karato, S., and H. Jung (1998), Water, partial melting and the origin of the seismic low velocity and high attenuation zone in the upper mantle, *Earth Planet. Sci. Lett.*, *157*, 193–207.

Katsura, T., and E. Ito (1989), The system Mg_2SiO_4-Fe_2SiO_4 at high pressures and temperatures: Precise determination of stabilities of olivine, modified spinel, and spinel, *J. Geophys. Res.*, *94*, 15,663–15,670.

Kawai, K., and R. J. Geller (2010), Waveform inversion for localized seismic structure and an application to D" structure beneath the Pacific, *J. Geophys. Res.*, *115*, doi: 10.1029/2009JB006503.

Kawai, K., and T. Tsuchiyac (2009), Temperature profile in the lowermost mantle from seismological and mineral physics joint modeling, *PNAS*, *106*(52), 22,119–22,123, doi:10.1073/pnas.0905920106.

Kind, R., and X. Li (2007), Deep earth structure – transition zone and mantle discontinuities, in *Treatise on Geophysics*, vol. 1, edited by G. Schubert, pp. 591–618, Elsevier B.V., Amsterdam, The Netherlands.

Knittle, E., and R. Jeanloz (1991), Earth's core-mantle boundary: Results of experiments at high pressure and temperature, *Science*, *251*, 1438–1443.

Komatitsch, D., and J. Tromp (2002a), Spectral-element simulations of global seismic wave propagation–I. validation, *Geophys. J. Int.*, *149*, 390–412.

Komatitsch, D., and J. Tromp (2002b), Spectral-element simulations of global seismic wave propagation-I. Validation, *Geophys. J. Int.*, *149*(2), 390–412, doi: 10.1046/j.1365-246X.2002.01653.x.

Komatitsch, D., and J. Tromp (2002c), Spectral-Element simulations of global seismic wave Propagation-I. validation, *Geophys. J. Int.*, *149*(2), 390–412, doi: 10.1046/j.1365-246X.2002.01653.x.

Komatitsch, D., and J. Tromp (2002d), Spectral-element simulations of global seismic wave propagation-II. three-dimensional models, oceans, rotation and self-gravitation, *Geophys. J. Int.*, *150*(1), 303–318, doi:10.1046/j.1365-246X.2002.01716.x.

Komatitsch, D., J. Ritsema, and J. Tromp (2002), The Spectral-Element method, beowulf computing, and global seismology, *Science*, *298*(5599), 1737 –1742, doi: 10.1126/science.1076024.

Kuo, B.-Y., E. J. Garnero, and T. Lay (2000), Tomographic inversion of S-SKS times for shear velocity heterogeneity in D": Degree 12 and hybrid models, *J. Geophys. Res.*, *105(B12)*, 28,139C28,157.

Kustowski, B., G. Ekström, and A. M. Dziewonski (2008), The anisotropic shear-wave velocity structure of the Earth's mantle: A global model, *J. Geophys. Res.*, *113*, B06,306, doi:10.1029/2007JB005169.

Labrosse, S., J. Hernlund, and J. Coltice (2007), A crystalizing dense magma ocean at the base of the Earth's mantle, *Nature*, *450*, 866–69.

Lawrence, J. F., and P. M. Shearer (2006a), A global study of transition zone: thickness using receiver functions, *J. Geophys. Res.*, *111*, B06,307, doi: 10.1029/2005JB003973.

Lawrence, J. F., and P. M. Shearer (2008), Imaging mantle transition zone thickness with *SdS-SS* finite-frequency sensitivity kernels, *Geophys. J. Int.*, *174*, 143–158, doi:10,1111/j.1365-246X.2007.03673.x.

Lawrence, J. F., and M. E. Wysession (2006), QLM9: a new radial quality factor (Q[μ]) model for the lower mantle, *Earth Planet. Sci. Lett.*, *241*(3-4), 962–971, doi:16/j.epsl.2005.10.030.

Lay, T., and E. J. Garnero (2004), Core-mantle boundary structures and processes, in *The State of the Planet: Frontiers and Challenges in Geophysics*, edited by R. Sparks and C. Hawkesworth, pp. 150:25–41, AGU, Washington, DC.

Lay, T., and E. J. Garnero (2007), Reconciling the postperovskite phase with seismological observations of lowermost mantle structure, in *Post-Perovskite: The Last Mantle Phase Transition*, edited by K. Hirose, J. Brodholt, T. Lay, and D. Yuen, pp. 174:129–53, AGU, Washington, DC.

Lay, T., and E. J. Garnero (2011), Deep mantle seismic modeling and imaging, *Annu. Rev. Earth Planet. Sci.*, *39*, 91–123, doi:10.1146/annurev-earth-040610-133354.

Lay, T., and D. V. Helmberger (1983), A lower mantle S-wave triplication and the shear velocity structure of D", *Geophys. J. Int.*, *75*(3), 799–837, doi:10.1111/j.1365-246X.1983.tb05010.x.

Lay, T., D. Heinz, M. Ishii, S. Shim, and T. Tsuchiya (2005), Multidisciplinary impact of the lower mantle perovskite phase transition, *Eos Trans. AGU*, *86(1)*, 1,5.

Lay, T., Q. Williams, and E. Garnero (1998), The core-mantle boundary layer and deep Earth dynamics, *Nature*, *392*(6675), 461–468.

Lay, T., E. Garnero, and Q. Williams (2004), Partial melting in a thermo-chemical boundary layer at the base of the mantle, *Phys. Earth Planet. Inter.*, *146*(3-4), 441–467.

Lay, T., J. Hernlund, E. J. Garnero, and M. S. Thorne (2006), A post-perovskite lens and D" heat flux beneath the central Pacific, *Science*, *314*(5803), 1272–1276.

Lay, T., J. Hernlund, and B. A. Buffett (2008), Core-mantle boundary heat flow, *Nature Geoscience*, *1*(1), 25–32.

Li, A., K. M. Fischer, M. E. Wysession, and T. J. Clarke (1998), Mantle discontinuities and temperature under the north american continental kernal, *Nature*, *395*(6698), 160–163, doi:10.1038/25972.

Li, C., R. van der Hilst, E. Engdah, and W. Burdic (2008), A new global model for P wave speed variations in Earth's mantle, *Geochem. Geophys. Geosyst.*, *9*, Q05,018.

Li, X., and B. Romanowicz (1995), Comparison of global waveform inversions with and without considering cross-branch modal coupling, *Geophys. J. Int.*, *121*(3), 695–709, doi:10.1111/j.1365-246X.1995.tb06432.x.

Long, M. (2009), Complex anisotropy in D" beneath the eastern Pacific from SKS-SKKS splitting discrepancies, *Earth Planet. Sci. Lett.*, *283*, 181–189.

Luo, S.-N., S. Ni, and D. V. Helmberger (2001), Evidence for a sharp lateral variation of velocity at the core-mantle boundary from multipathed PKPab, *Earth Planet. Sci. Lett.*, *189*(3-4), 155 – 164, doi:10.1016/S0012-821X(01)00364-8.

Mao, W., H. Mao, W. Sturhahn, J. ZHao, and V. Prakapenka (2006), Iron-rich post-perovskite and the origin of ultralow-velocity zones, *Science*, *312*, 564–65.

Marone, F., Y. Gung, and B. Romanowicz (2007), Three-dimensional radial anisotropic structure of the north american upper mantle from inversion of surface waveform data, *Geophys. J. Int.*, *171*(1), 206–222, doi:10.1111/j.1365-246X.2007.03465.x.

Masters, G., G. Laske, H. Bolton, and A. Dziewonski (2000), The relative behavior of shear velocity, bulk sound speed, and compressional velocity in the mantle: Implications for chemical and thermal structure, in *Earth's Deep Interior: Mineral Physics and Tomography from the Atomic to the Global Scale*, vol. 117, pp. 63–87, Geophys. Mono. AGU.

McNamara, A., and S. Zhong (2004), Thermochemical structures within a spherical mantle: superplumes or piles?, *J. Geophys. Res.*, *109*, B07,402.

McNamara, A., and S. Zhong (2005), Thermochemical structures beneath Africa and the Pacific Ocean, *Nature*, *437*, 1136–39.

McNamara, A. K., P. E. van Keken, and S. Karato (2003), Development of finite strain in the convecting lower mantle and its implications for seismic anisotropy, *J. Geophys. Res.*, *108*, 14 PP., doi:200310.1029/2002JB001970.

McNamara, A. K., E. J. Garnero, and S. Rost (2010), Tracking deep mantle reservoirs with ultra-low velocity zones, *Earth Planet. Sci. Lett.*, *299*(1-2), 1–9, doi: 10.1016/j.epsl.2010.07.042.

Murakami, M., K. Hirose, K. Kawamura, N. Sata, and Y. Ohishi (2004), Post-Perovskite Phase Transition in MgSiO3, *Science*, *304*(5672), 855–858, doi: 10.1126/science.1095932.

Neele, F., and H. de Regt (1999), Imaging upper-mantle discontinuity topography using underside-reflection data, *Geophys. J. Int.*, *137*, 91–106.

Neele, F., H. de Regt, and J. VanDecar (1997), Gross errors in upper-mantle discontinuity topography from underside reflection data, *Geophys. J. Int.*, *129*, 194–204.

Ni, S., and D. Helmberger (2003a), Seismological constraints on the South African superplume; could be the oldest distinct structure on Earth, *Earth Planet. Sci. Lett.*, *206*(1-2), 119–131.

Ni, S., and D. Helmberger (2003b), Ridge-like lower mantle structure beneath South Africa, *J. Geophys. Res.*, *108*(B2).

Ni, S., E. Tan, M. Gurnis, and D. V. Helmberger (2002), Sharp sides to the African superplume, *Science*, *296*, 1850–1852.

Ni, S., V. Cormier, and D. Helmberger (2003), A comparison of synthetic seismograms for 2D structures: Semianalytical versus numerical, *Bull. Seismol. Soc. Am.*, *93*(6), 2752–2757.

Ni, S., D. Helmberger, and J. Tromp (2005), Three-dimensional structure of the African superplume from waveform modelling, *Geophys. J. Int.*, *161*(2), 283–294.

Nolet, G., and F. A. Dahlen (2000), Wave front healing and the evolution of seismic delay times, *J. Geophys. Res.*, *105*(B8), 054.

Obayashi, M., and Y. Fukao (1997), P and PcP travel time tomography for the core-mantle boundary, *J. Geophys. Res.*, *102*(B8), 841.

Panning, M., and B. Romanowicz (2006), A three dimensional radially anisotropic model of shear velocity in the whole mantle, *Geophys. J. Int.*, *167*, 361–379, doi: 10.1111/j.1365-246X.2006.03100.x.

Persh, S. E., J. E. Vidale, and P. S. Earle (2001), Absence of short-period ULVZ precursors to PcP and ScP from two regions of the CMB, *Geophys. Res. Lett.*, *28*(2), 387–390.

Pulliam, J., and M. K. Sen (1998), Anisotropy in the core-mantle transition zone may indicate chemical heterogeneity, *Geophys. J. Int.*, *135*, 113–128.

Reasoner, C., and J. Revenaugh (2000), ScP constraints on ultralow-velocity zone density and gradient thickness beneath the pacific, *J. Geophys. Res.*, *105*(B12), 182.

Reid, F. J. L., J. H. Woodhouse, and H. J. V. Heijst (2001), Upper mantle attenuation and velocity structure from measurements of differential s phases, *Geophys. J. Int.*, *145*(3), 615–630, doi:10.1046/j.1365-246x.2001.01395.x.

Resovsky, J., J. Trampert, and R. V. der Hilst (2005), Error bars for the global seismic q profile, *Earth and Planetary Science Letters*, *230*, 413–423, doi: 16/j.epsl.2004.12.008.

Restivo, A., and G. Helffrich (2006), Core-mantle boundary structure investigated using SKS and SKKS polarization anomalies, *Geophys. J. Inter.*, *165*(1), 288–302.

Revenaugh, J., and R. Meyer (1997), Seismic evidence of partial melt within a possibly ubiquitous low-velocity layer at the base of the mantle, *Science*, *277*(5326), 670–673.

Ritsema, J., and R. M. Allen (2003), The elusive mantle plume, *Earth Planet. Sci. Lett.*, *207*, 1–12.

Ritsema, J., and H. van Heijst (2000), Seismic imaging of structural heterogeneity in Earth's mantle: evidence for large-scale mantle flow, *Sci. Prog.*, *83*, 243–59.

Ritsema, J., and H. J. van Heijst (2002), Constraints on the correlation of p- and s-wave velocity heterogeneity in the mantle from p, PP, PPP, and PKPab traveltimes, *Geophys. J. Int.*, *149*, 482–489.

Ritsema, J., M. Hagerty, and T. Lay (1995), Comparison of broad-band and short-period seismic wave-form stacks - implications for upper-mantle discontinuity structure, *Geophys. Res. Lett.*, *22*, 3151–3154.

Ritsema, J., E. Garnero, and T. Lay (1997), A strongly negative shear velocity gradient and lateral variability in the lowermost mantle beneath the Pacific, *J. Geophys. Res.*, *102*, 20,395–20,411.

Ritsema, J., S. Ni, D. V. Helmberger, and H. P. Crotwell (1998), Anomalous shear velocity reductions and gradients in the lower mantle beneath Africa, *Geophys. Res. Lett.*, *25*, 4245–4248.

Ritsema, J., H. J. van Heijst, and J. H. Woodhouse (1999), Complex shear velocity structure imaged beneath Africa and Iceland, *Science*, *286*, 1925–1928.

Ritsema, J., L. A. Rivera, D. Komatitsch, J. Tromp, and H.-J. van Heijst (2002), Effects of crust and mantle heterogeneity on PP/P and SS/S amplitude ratios, *Geophys. Res. Lett.*, *29*(10), doi:10.1029/2001GL013831.

Ritsema, J., H. J. Van Heijst, and J. H. Woodhouse (2004), Global transition zone tomography, *J. Geophys. Res.*, *109*, B02,302, doi:10.1029/2003JB002610.

Ritsema, J., A. K. McNamara, and A. Bull (2007a), Tomographic filtering of geodynamic models: Implications for model interpretation and large-scale mantle structure, *J. Geophys. Res.*, *112*, B01,303, doi:10.1029/2006JB004566.

Ritsema, J., A. K. McNamara, and A. L. Bull (2007b), Tomographic filtering of geodynamic models: Implications for model interpretation and large-scale mantle structure, *J. Geophys. Res.*, *112*(B01303), doi:10.1029/2006JB004566.

Ritsema, J., H. J. Van Heijst, J. H. Woodhouse, and A. Deuss (2009a), Long-period body wave traveltimes through the crust: implication for crustal corrections and seismic tomography, *Geophys. J. Int.*, *179*, 1255–1261.

Ritsema, J., W. Xu, L. Stixrude, and C. Lithgow-Bertelloni (2009b), Estimates of the transition zone temperature in a mechanically mixed upper mantle, *Earth Planet. Sci. Lett.*, *277*, 244–252.

Ritsema, J., A. Deuss, H. J. van Heijst, and J. H. Woodhouse (2010), S40RTS: a degree-40 shear-velocity model for the mantle from new Rayleigh wave dispersion, teleseismic traveltime and normal-mode splitting function measurements., *Geophys. J. Int.*, doi:10.1111/j.1365-246X.2010.04884.x.

Ritsema, J., A. Deuss, H. J. Van Heijst, and J. H. Woodhouse (2011), S40RTS: a degree-40 shear-velocity model for the mantle from new rayleigh wave dispersion, teleseismic traveltime and normal-mode splitting function measurements, *Geophys. J. Int*, *184*, 1223–1236, doi:10.1111/j.1365-246X.2010.04884.x.

Rokosky, J. M., T. Lay, and E. J. Garnero (2006), Small-scale lateral variations in azimuthally anisotropic D" structure beneath the Cocos Plate, *Earth Planet. Sci. Lett.*, *248*(1-2), 411–425, doi:16/j.epsl.2006.06.005.

Romanowicz, B. (1995), A global tomographic model of shear attenuation in the upper mantle, *J. Geophys. Res.*, *100*(B7), PP. 12,375–12,394, doi: 199510.1029/95JB00957.

Rondenay, S., and K. Fischer (2003), Constraints on localized core-mantle boundary structure from multichannel, broadband SKS coda analysis, *J. Geophys. Res*, *108*(B11).

Rondenay, S., V. Cormier, and E. V. Ark (2010), SKS and SPdKS sensitivity to two-dimensional ultra-low velocity zones, *J. Geophys. Res.*, *115*, B04,311.

Rost, S., and E. J. Garnero (2006), Detection of an ultralow velocity zone at the core-mantle boundary using diffracted PKKPab waves, *J. Geophys. Res*, *111*(B7).

Rost, S., and J. Revenaugh (2001), Seismic detection of rigid zones at the top of the core, *Science*, *294*(5548), 1911–1914.

Rost, S., and J. Revenaugh (2003), Small-scale ultralow-velocity zone structure imaged by ScP, *J. Geophys. Res.*, *108*(B1).

Rost, S., and C. Thomas (2009), Improving seismic resolution through seismic arrays, *Surv. Geophys.*, *30*(4–5), 271–299, doi:10.1007/s10712-009-9070-6.

Rost, S., E. J. Garnero, and W. Stefan (2010a), Thin and intermittent ultralow-velocity zones, *J. Geophys. Res.*, *115*(B6), doi:10.1029/2009JB006981.

Rost, S., E. J. Garnero, M. S. Thorne, and A. R. Hutko (2010b), On the absence of an ultralow-velocity zone in the North Pacific, *J. Geophys. Res.*, *115*(B4), doi: 10.1029/2009JB006420.

Rost, S., E. Garnero, Q. Williams, and M. Manga (2005), Seismological constraints on a possible plume root at the core-mantle boundary, *Nature*, *435*(7042), 666–669.

Rost, S., E. J. Garnero, and Q. Williams (2006), Fine-scale ultralow-velocity zone structure from high-frequency seismic array data, *J. Geophys. Res.*, *111*(B9).

Roth, E., D. Wiens, L. Dorman, J. Hildebrand, and S. C. Webb (1999), Seismic attenuation tomography of the Tonga-Fiji region using phase pair methods, *J. Geophys. Res.*, *194*, 4597–4809.

Russell, S., C. Reasoner, T. Lay, and J. Revenaugh (2001), Coexisting shear- and compressional-wave seismic velocity discontinuities beneath the central Pacific, *Geophys. Res. Lett.*, *28*(11), 2281–2284.

Schutt, D., and E. Humphreys (2001), Evidence for a deep asthenosphere beneath North America from western united states SKS splits, *Geology*, *29*(4), 291–294.

Selby, N. D., and J. H. Woodhouse (2000), Controls on rayleigh wave amplitudes: attenuation and focusing, *Geophys. J. Int.*, *142*(3), 933–940, doi:10.1046/j.1365-246x.2000.00209.x.

Shearer, P. M. (1991), Constraints on upper-mantle discontinuities from observations of long-period reflected and converted phases, *J. Geophys. Res.*, *96*, 18,147–18,182.

Shearer, P. M. (2000), Upper mantle seismic discontinuities, *Geophys. Mono.*, *117*, 115–131.

Shearer, P. M., and T. G. Masters (1992), Global mapping of topography on the 660-km discontinuity, *Nature*, *355*, 791–796.

Shearer, P. M., M. P. Flanagan, and M. A. H. Hedlin (1999), Experiments in migration processing of SS precursor data to image upper mantle discontinuity strucure, *J. Geophys. Res.*, *104*, 7229–7242.

Silver, P., and C. Bina (1993), An anomaly in the amplitude ratio of SKKS/SKS in the range 100-108-degrees from portable teleseismic data, *Geophys. Res. Lett.*, *20*(12), 1135–1138.

Simmons, N., and S. Grand (2002), Partial melting in the deepest mantle, *Geophys. Res. Lett.*, *29*(11), 1552.

Simmons, N. A., A. M. Forte, and S. P. Grand (2009), Joint seismic, geodynamic and mineral physical constraints on three-dimensional mantle heterogeneity: implications for the relative importance of thermal versus compositional heterogeneity, *Geophys. J. Int.*, *177*, 1284–1304.

Sleep, N. (1990), Hotspots and mantle plumes: Some phenomenology, *J. Geophys. Res*, *95*, 6715–6736.

Souriau, A., and G. Poupinet (1991), A study of the outermost liquid core using differential travel-times of the SKS-phase, SKKS-phase and S3KS-phase, *Phys. Earth Planet. Inter.*, *68*(1-2), 183–199.

Stacey, F., and D. Loper (1983), The therma boundary layer interpretation of D" and its role as a plume source, *Phys. Earth Panet. Inter.*, *33*, 45–50.

Stein, S., and M. Wysession (2003), Introduction to Seismology, Earthquakes, and Earth Structure, Blackwell Sci.

Stutzmann, E., L. Vinnik, A. Ferreira, and S. Singh (2000), Constraint on the S-wave velocity at the base of the mantle, *Geophys. Res. Lett.*, *27*(11), 1571–1574.

Sun, D., and D. Helmberger (2008), Lower mantle tomography and phase change mapping, *J. Geophys. Res.*, *113*(B10), doi:10.1029/2007JB005289.

Sun, D., E. Tan, D. Helmberger, and M. Gurnis (2007), Seismological support for the metastable superplume model, sharp features, and phase changes within the lower mantle, *PNAS*, *104*(22), 9151–9155, doi:10.1073/pnas.0608160104.

Sun, D., D. Helmberger, and M. Gurnis (2010), A narrow, mid-mantle plume below southern Africa, *Geophys. Res. Lett.*, *37*(L09302), 5 PP., doi: 10.1029/2009GL042339.

Sylvander, M., and A. Souriau (1996), Mapping S-velocity heterogeneities in the D" region, from SmKS differential travel times, *Phys. Earth Planet. Inter.*, *94*(1-2), 1–21.

Takeuchi, N. (2007), Whole mantle SH velocity model constrained by waveform inversion based on three-dimensional Born kernels, *Geophys. J. Int.*, *169*, 1153–63.

Takeuchi, N., Y. Morita, N. D. Xuyen, and N. Q. Zung (2008), Extent of the low-velocity region in the lowermost mantle beneath the western Pacific detected by the Vietnamese Broadband Seismograph Array, *Geophys. Res. Lett.*, *35*, doi:10.1029/2008GL033,197.

Tan, E., and M. Gurnis (2005), Metastable superplumes and mantle compressibility, *Geophys. Res. Lett.*, *32*, L20,307.

Tan, E., M. Gurnis, and L. Han (2002), Slabs in the lower mantle and their modulation of plume formation, *Geochem. Geophys. Geosyst.*, *3*, 11,067.

Tanaka, S. (2002), Very low shear wave velocitv at the base of the mantle under the South Pacific Superswell, *Earth Planet. Sci. Lett.*, *203*(3-4), 879–893.

Tanaka, S. (2007), Possibility of a low P-wave velocity layer in the outermost core from global SmKS waveforms, *Earth Planet. Sci. Lett.*, *259*(3-4), 486–499, doi: 10.1016/j.epsl.2007.05.007.

Thompson, P., and P. Tackley (1998), Generation of mega-plumes from the core-mantle boundary in a compressible mantle with temperature-dependent viscosity, *Geophys. Res. Lett.*, *25*, 1999–2002.

Thorne, M., and E. Garnero (2004), Inferences on ultralow-velocity zone structure from a global analysis of SPdKS waves, *J. Geophys. Res.*, *109*(B8).

Thorne, M., T. Lay, E. Garnero, G. Jahnke, and H. Igel (2007), Seismic imaging of the laterally varying D" region beneath the Cocos Plate, *Geophys. J. Int.*, *170*, 635–648, doi:10.1111/j.1365-246X.2006.03279.x.

Tibuleac, I. M., G. Nolet, M. Caryl, and I. Koulakov (2003), P wave amplitudes in a 3-D earth, *Geophys. J. Int.*, *155*(1), 1–10, doi:10.1046/j.1365-246X.2003.01969.x.

To, A., B. Romanowicz, Y. Capdeville, and N. Takeuchi (2005), 3D effects of sharp boundaries at the borders of the African and Pacific Superplumes: Observation and modeling, *Earth Planet. Sci. Lett.*, *233*(1-2), 137–153.

Torsvik, T., M. Smethurst, K. Burke, and B. Steinberger (2006), Large Igneous Provinces generated from the margins of the large low-velocity provinces in the deep mantle, *Geophys. J. Int.*, *167*, 1447–60.

Torsvik, T., K. Burke, B. Steinberger, S. Webb, and L. Ashwal (2010), Diamonds sampled by plumes from the core-mantle boundary, *Nature*, *466*, 352–55.

Trampert, J., F. Deschamps, J. Resovsky, and D. Yuen (2004), Probabilistic tomography maps chemical heterogeneities throughout the lower mantle, *Science*, *306*, 853–856.

Tronnes, R. (2009), Structure, mineralogy and dynamics of the lowermost mantle, *Mineral. Petrol.*, *99*, 243–61.

Tsuchiya, T., and J. Tsuchiya (2006), Effect of impurity on the elasticity of perovskite and postperovskite: Velocity contrast across the postperovskite transition in (Mg,Fe,Al)(Si,Al)O3, *Geophys. Res. Lett.*, *33*, doi:doi:10.1029/2006GL025706.

Tsuchiya, T., J. Tsuchiya, K. Umemoto, and R. M. Wentzcovitch (2004), Elasticity of post-perovskite MgSiO3, *Geophys. Res. Lett.*, *31*, doi:10.1029/2004GL020278.

van der Hilst, R., M. de Hoop, P. Wang, S. Shim, P. Ma, and L. Tenoria (2007), Seismostratigraphy and thermal structure of Earth's core-mantle boundary region, *Science*, *315*, 1813–17.

Vinnik, L. P., V. Farra, and B. Romanowicz (1989), Azimuthal anisotropy in the earth from observations of sks at geoscope and nars broadband stations, *Bull. Seismol. Soc. Am.*, *79*(5), 1542–1558.

Wang, Y., and L. Wen (2004), Mapping the geometry and geographic distribution of a very low velocity province at the base of the Earth's mantle, *J. Geophys. Res.*, *109*, B10,305.

Wang, Z., and F. A. Dahlen (1995), Validity of surface-wave ray theory on a laterally heterogeneous earth, *Geophys. J. Int.*, *123*(3), 757–773, doi:10.1111/j.1365-246X.1995.tb06888.x.

Warren, L. M., and P. M. Shearer (2002), Mapping lateral variations in upper mantle attenuation by stacking P and PP spectra, *J. Geophys. Res. (Solid Earth)*, *107*, 2342, doi:10.1029/2001JB001195.

Weber, M. (1993), P- and S-wave reflections from anomalies in the lowermost mantle, *Geophys. J. Int.*, *115*(1), 183–210, doi:10.1111/j.1365-246X.1993.tb05598.x.

Wen, L. (2001), Seismic evidence for a rapidly varying compositional anomaly at the base of the Earths mantle beneath the Indian Ocean, *Earth Planet. Sci. Lett.*, *194*, 83 – 95.

Wen, L. (2006), A compositional anomaly at the Earth's core-mantle boundary as an anchor to the relatively slowly moving surface hotspots and as source to the DUPAL anomaly, *Earth Planet. Sci. Lett.*, *246*, 138–48.

Williams, Q., and E. Garnero (1996), Seismic evidence for partial melt at the base of Earth's mantle, *Science*, *273*(5281), 1528–1530.

Woodhouse, J. H., and Y. K. Wong (1986), Amplitude, phase and path anomalies of mantle waves, *Geophys. J. Int.*, *87*(3), 753–773, doi:10.1111/j.1365-246X.1986.tb01970.x.

Woodward, R. L., and G. Masters (1991), Global Upper Mantle Structure From Long-Period Differential Travel Times, *J. Geophys. Res.*, *93(B4)*, 63516377.

Wookey, J., S. Stackhouse, J. Kendall, J. Brodholt, and G. Price (2005), Efficacy of the postperovskite phase as an explanation for lowermost-mantle seismic properities, *Nature*, *189*, 141–53.

Wysession, M. E., E. A. Okal, and C. R. Bina (1992), The structure of the core-mantle boundary from diffracted waves, *J. Geophys. Res.*, *97*, 8749–8764.

Wysession, M. E., K. M. Fischer, G. I. Al-eqabi, P. J. Shore, and I. Gurari (2001), Using MOMA Broadband Array ScS-Sdata to image smaller-scale structures at the base of the mantle, *Geophys. Res. Lett.*, *28*(5), PP. 867–870, doi: 200110.1029/2000GL008485.

Xu, F., J. E. Vidale, and P. S. Earle (2003), Survey of precursors to P'P': Fine structure of mantle discontinuities, *J. Geophys. Res*, *108*, 2024, doi: 10.1029/2001JB000817.

Xu, W., C. Lithgow-Bertelloni, L. Stixrude, and J. Ritsema (2008), The effects of bulk composition and temperature on mantle seismic structure, *Earth Planet. Sci. Lett.*, *230*, 97–112.

Xu, Y., and K. D. Koper (2009), Detection of a ULVZ at the base of the mantle beneath the northwest pacific, *Geophys. Res. Lett.*, *36*, 5 PP., doi: 200910.1029/2009GL039387.

Yang, X., T. Lay, X.-B. Xie, and M. S. Thorne (2007), Geometric Spreading of Pn and Sn in a Spherical Earth Model, *Bull. Seismol. Soc. Am.*, *97*(6), 2053–2065, doi:10.1785/0120070031.

Young, C. J., and T. Lay (1987), The core-mantle boundary, *Annu. Rev. Earth Planet. Sci.*, *15*, 25.

Yuen, D., O. Cadek, A. Chopelas, and C. Matyska (1993), Geophysical inferences of thermal-chemical structures in the lower mantle, *Geophys. Res. Lett.*, *20*, 899–902.

Zhang, Y., J. Ritsema, and M. Thorne (2009), Modeling the ratios of SKKS and SKS amplitudes with ultra-low velocity zones at the core-mantle boundary, *Geophys. Res. Lett.*, *36*, doi:10.1029/2009GL040030.

Zhao, D. (2004), Global tomographic images of mantle plumes and subducting slabs: insight into deep Earth dynamics, *Phys. Earth Planet. Inter.*, *146*, 3–34.

Zhao, L., and S. Chevrot (2003), *SS*-wave sensitivity to upper mantle structure: Implications for the mapping of transition zone discontinuity topographies, *Geophys. Res. Lett.*, *30(11)*, 1590, doi:10.1029/2003GL017223.